

Contents

1	Introduction	1
1.1	Project Outline	4
2	Theoretical Background	7
2.1	Plasmons	7
2.1.1	Electromagnetic Waves	8
2.1.2	Bulk Plasmons and the Optical Properties of Metals	10
2.1.3	Surface Plasmons	12
2.2	Plasmon Coupling	19
2.2.1	Classical Models of Plasmonic Coupling	21
2.2.2	The Dynamical Optical Response of Plasmonic Dimers: Transitioning from Capacitive to Conductive Plasmonic Coupling	24
2.3	Plasmons in Tips	34
2.3.1	The Electromagnetic Response of Tips	36
2.3.2	Challenges associated with Tip Plasmonics	40
2.3.3	Tip Modification, Nanostructuring and Optical Antenna Tips	42
2.4	Conclusions	44
3	Electrochemical Fabrication of Spherical AuNP-Tipped AFM Probes	47
3.1	Electrochemical Deposition	48
3.2	Initial Fabrication of Spherical AuNP-Tipped AFM Probes	49
3.2.1	Dependence of Tip Morphology on Voltage and Underlying Nucleation Mechanisms	52
3.2.2	Decontamination of Tip Surfaces and Post-Fabrication Processing	55
3.3	Conclusions	56
4	Microscope Design for Simultaneous Measurements on Plasmonic Tips	59
4.1	Mechanical Design	59
4.2	Optical Design	61
4.2.1	Confocal Localisation of Spectra	65
4.2.2	Characterisation of Microscope Performance	67
4.3	Electronics Design	72
4.4	AFM Design: Measurements of Force	75
4.4.1	Calibrating the AFM	77
4.5	Scanning Capacitive AFM Tip Alignment	78
4.5.1	Mechanism for Alignment of Two Opposing Tips	78
4.5.2	Numerical Solutions for Tip Alignment	80

4.5.3	Experimental Measurements using Scanning Capacitance Microscopy . . .	83
4.5.4	Experimental Alignment of Tips using Scanning Capacitance AFM . . .	86
4.6	Conclusions	88
5	Understanding and Applying Single Tip Plasmonics	91
5.1	Optical Characterisation of Nanostructures using Hyperspectral Imaging . . .	91
5.2	Understanding Plasmons in Spherical Nanoparticle Tips	94
5.2.1	Interpreting the Spectral Response of Metallic Tips	96
5.2.2	Implications of Spherical Metallic Tip Plasmonics	99
5.3	Improved Field Enhancement of Spherical Au Nanoparticle Tips	100
5.4	Conclusions	104
6	Plasmon Interactions in Tip Dimers	105
6.1	Non-Optical Experimental Measurements of Dynamic Tip Dimers	105
6.1.1	General Properties of a Nano-Tip Dimer Gap	107
6.2	Plasmonic Coupling Between Tips	111
6.2.1	Sharp Tip Dimer Interactions	111
6.2.2	Spherical Tip Dimer Interactions	113
6.3	Quantum Effects in Sub-nm Gaps between Spherical-Tipped AFM Probes . .	116
6.3.1	Observations of Quantum Charge Transport in Plasmonic Cavities . . .	119
6.4	Conclusions	124
7	Conclusions and Outlook	127
7.1	Outlook and Future Directions	129
	References	131
	List of Symbols	145
	Acronyms	149
	Appendices	151

Optics has always stood as one of the primary branches of applied science, used to probe and extract information from many physical systems. By studying the way light interacts with a material its properties can be discerned. This is the main principle behind optical microscopy. Conventional optics, solely based upon the use of light, **however**, is held back by a fundamental limitation. The finite momentum of the photon restricts the spatial confinement of light to its wavelength. Since the discovery of the diffraction limit in 1873, much work has been done trying to circumvent its imposed limitations and retrieve information from sub-wavelength dimensions. Whilst the diffraction limit is firmly fixed for freely propagating photons it can be broken at an interface, where waves can acquire evanescent character. Such surface waves can exist with wavelengths far below those of photons and aid in the extraction of optical information from nanoscale sources. By understanding the electromagnetic behaviour of waves on an interface, optics can be brought down to nanoscale dimensions.

Nanophotonics, or nanooptics, is the name given to the progression of optics into the sub-wavelength domain - the understanding and application of light beyond the diffraction limit. Electromagnetic fields surrounding an object on these sub-wavelength length scales are said to be in the *near-field* domain as opposed to the conventionally *far-field*. To achieve this level of localisation, nanophotonics exploits light-matter interactions. Matter polarised by an external electromagnetic field can generate its own fields with much smaller degrees of localisation. These fields are determined both by the incident field and by the physical characteristics of the matter. By this mechanism the optical properties of metals on the nanometre scale become particularly interesting through the excitation of plasmons.

Plasmons are the quanta of collective oscillations of optically-driven free electrons, the study of which is known as plasmonics. By transferring photonic energy into surface plasmons at the surface of a metal the limits of optical confinement can be overcome, allowing light to be strongly confined to sub-wavelength dimensions in the form of a surface charge density oscillation. For this reason plasmonics is sometimes known as “*metal optics*”. Surface plasmons maintain the same frequency as their photonic excitation, however their wavelength is far below

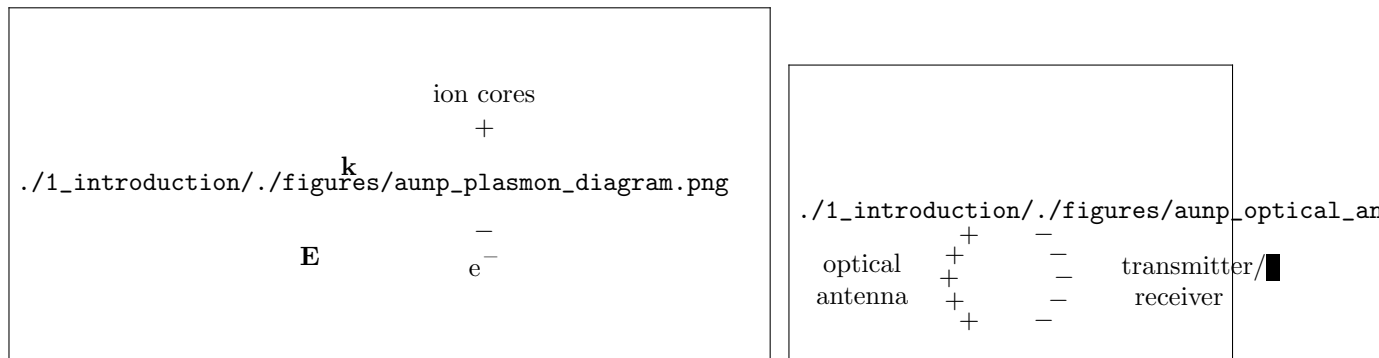


Figure 1.1: Diagram of a localised surface plasmon in a AuNP. Electrons move to screen the external field from the AuNP. The charge density at the electromagnetic poles of the surface greatly enhances the local field. AuNPs are therefore considered to be optical nano-antennae. The electric field from a near-field transmitter is coupled via an antenna into far-field radiation. By reciprocity, far-field radiation can be received in the near-field.

the diffraction limit. The result is a highly concentrated energy density at the poles of the charge oscillation on the metal surface. Charge accumulates at the surface, thus the electric field surrounding a strongly confined plasmon becomes significantly enhanced. This resonant near-field enhancement is one of the defining features of plasmons and forms the basis for nearly all applications of plasmonics to date.

The existence of plasmons has been known for over a century, however limited experimental access to metallic nanostructures restricted their study and application until technology advanced. The advent of modern microscope technology and nanostructure synthesis reignited the field and, over the course of the last 40 years, has led to the development of many novel nanotechnologies, including enhanced vibrational spectroscopies [1, 2] and near-field optical microscopy [3–8]. The most widespread of these technologies exploit the local field enhancement around a plasmonic metallic nanostructure or the more intense “hot spots” formed between coupled plasmons in many nanostructures in order to efficiently interact with nanoscale objects. Using plasmons, fields can be both transferred to and extracted from sub-wavelength dimensions containing nano-absorbers and nano-emitters, such as molecules and quantum dots (Figure 1.1). Such structures supporting plasmons that readily couple with light have since become known as optical nanoantennae, in analogy with conventional metal radio wave antennae [9].

In the vast majority of plasmonic developments, nanostructures are made from noble metals, which, due to their highly mobile electrons, are especially good at sustaining surface plasmons in the visible region of the electromagnetic spectrum. This is particularly true for plasmons in a metallic nanoparticle, which develop highly localised fields on resonance with light as a result of field induced surface charge accumulation (Figure 1.1). These are known as surface plasmon resonances (SPRs) and lead to resonant field enhancement at the plasmon poles.

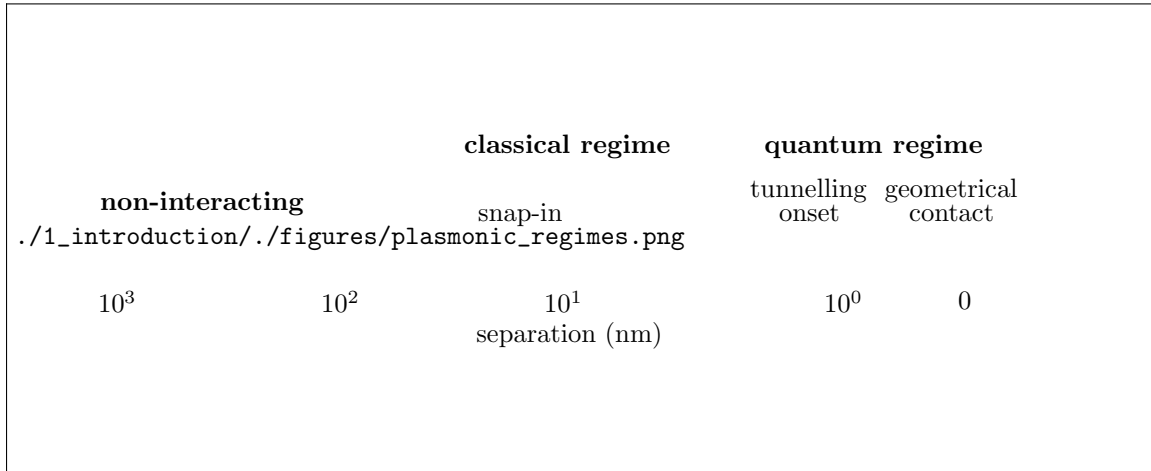


Figure 1.2: Regimes of plasmonic interaction. The diagram shows the coupling strength between two plasmonic particles across the full range of characteristic separation dimensions. At distances greater than the particle radius plasmons are uncoupled. Classical mode coupling begins at separations below the particle radius. Many nanoscale phenomena, such as capillary force/surface tension snap-in occur at these characteristic separations. Once the separation transitions to below 1 nm quantum mechanical effects begin to become important. The quantum regime is the point at which these effects significantly effect plasmonic interaction.

Sensing has become the primary application of plasmonic nanoantennae. Surface-enhanced Raman scattering (SERS) can be used to enhance weakly interacting¹ inelastic (Raman) scattering from vibrating molecules [10] by a factor of $|E/E_0|^4$ where $|E/E_0|$ is the field enhancement at the location of the molecules placed in the vicinity of plasmonic nanostructure. In this case the excited plasmonic mode is a spatially better match to the interaction cross-section of molecules than the much larger wavelength of diffraction-limited light. Scanning near-field optical microscopy (SNOM) is a similar technique by which near-field light is collected through a sub-wavelength-size aperture, a process that can be similarly boosted through use of a plasmonic aperture. The culmination of these developments is the recent ability to measure light scattering from just a few molecules within a single hot spot [11].

Realistically, however, fields can only be enhanced so far. By continuing to push the boundaries towards robust single molecule plasmonic sensing, intuition suggests that plasmonic systems must become increasingly smaller to confine light into even small volumes and further increase the localised near-field enhancement. Inevitably though, the characteristic dimensions of the nano-gaps sustaining the hot spots, or the particles themselves, becomes sufficiently small that quantum mechanical effects, such as quantum tunnelling, ballistic transport and non-locality, are no longer negligible and begin to adversely affect confinement (Figure 1.2). Plasmonics in these quantum mechanically-limited regimes currently only has a limited understanding due to difficulty in reliably accessing sub-nm length scales. To a certain extent this is primarily caused by difficulty fabricating structures with such small characteris-

¹Only 1 in 10^7 photons inelastically scatter from the bonds in a vibrating molecule.

tic features. Few reports have therefore conclusively shown the influence of quantum effects on plasmonic performance and it remains an interesting and relatively new region of plasmonics that still requires exploring.

The ideal way of experimentally mapping the quantum regime is to use precisely positioned individual nanoparticles coming closer together and transitioning from classical to quantum to contacted interaction regimes. Though possible in many ways, the dynamic control and precise positioning of a sub-nm cavity between two nanoparticles is not a trivial task. While there are methods for controlling nanoparticle positions, difficulty arises as to what measurements are then possible. A rich amount of fundamental physics exists within sub-nm gaps that can strongly influence plasmonic behaviour, therefore a system must be carefully designed to enable measurement of each significant effect. Sensitive measurements of charge transfer and forces, not compatible with individual nanoparticle experiments, are required to probe both plasmonic and quantum mechanical effects. Consequently, precise nanopositioning of an electrically contacted nanoparticle with force sensitivity is required in order to experimentally access and improve the understanding of the quantum regime of plasmonics.

AFM probes are appealing devices as a means of controllably progressing into the sub-nm regime whilst simultaneously making the necessary measurements to understand the quantum regime, though a plasmonic tip apex structure is a necessity. Metallic tip structures at a glance are promising plasmonic probes as characteristic apex dimensions readily fall well below the diffraction limit. Furthermore, a clear advantage of tip systems is the maturity of the many surface science techniques used for characterising nanoscale topology, forces and electronic properties. Techniques such as scanning tunnelling microscopy (STM) [12] and atomic force microscopy (AFM) [13] have formed the foundation of surface analysis studies since their inception. By combining AFM probe-based techniques with optical measurements further insight into quantum mechanical effects in plasmonic systems can be gained. This was the approach adopted by Savage *et al.* to initially investigate and reveal this domain [14] and remains the case throughout this project.

1.1 Project Outline

The primary purpose of this project is to demonstrate robust measurements of plasmonic gaps in the sub-nm regime, at the point when quantum effects become important, building upon the work conducted by Savage *et al.* [14]. A significantly modified microscope design is employed compared to that used by Savage *et al.* in order to incorporate a larger range of possible measurements and potential experiments. By using a combined atomic force-optical microscope and two opposing, plasmonic tips, plasmons can be dynamically probed using multiple, simultaneous, correlated measurements. A large amount of time and effort has been dedicated to the design and construction of a microscope capable of making simultaneous

measurements of the electronic, force and optical signals from a plasmonic tip dimer in order to better understand the quantum regime of plasmon coupling. Both the microscope technology and the sample fabrication technology are heavily developed to enable robust measurements on sub-nm gaps and improve upon the current standards of experiment.

A prerequisite of all experiments is the availability of plasmonic AFM tips with far-field SPRs, the simplest geometry of which is a spherical tip apex. Spherical AuNPs mounted onto two conductive AFM tips are used to dynamically form plasmonic nano-gaps. Though studies using commercially available spherical Au tips are still carried out, the sensitivity of measurements in the sub-nm regime requires more resistant probes. Despite the widespread use of tips in metal optics techniques, the application of nanostructured (optical antennae) tips for improved performance is a relatively recent idea. Little work has been reported on the modification of the sharp tip geometry and spherical apex modification for plasmonic purposes remains complex and expensive. To address these issues, a new fabrication technique using electrodeposition is developed as a simple method for producing spherically nanostructured metallic tips. The optical response of both sharp and spherical metallic tips is then characterised using a selection of techniques developed to identify the plasmons supported by each structure. Tips are then applied to Raman scattering to demonstrate the improvements when using nanostructured tips.

Finally, with all experimental components in place, interactions between two coupled tips are investigated, progressing into the domain of sub-nm plasmonic gaps. Current experiments in the quantum regime build upon both previous experimental efforts and the proposed theoretical foundations emerging in recent years showing that conductance is the dominant factor effecting the fundamental degree to which light can be confined and that a set of critical conductances exist which define the boundaries between each of the quantum regimes.

This report necessarily begins with the theoretical background required to understand plasmons and the relevant plasmonic phenomena within the scope of this project. The previous uses of tips for plasmonics, along with their current understanding, are detailed to motivate their use in experimental plasmonics. The experimental work carried out in this project is discussed in three parts:

- the production of spherical-apex plasmonic AFM tips by electrochemical nanostructuring
- the design and construction of a microscope capable of making stable measurements on an AFM tip dimer in the sub-nm regime
- experiments performed using combinations of plasmonic AFM tips in the microscope

These results are broken down into understanding the plasmonics of individual spherically-nanostructured tips followed by understanding of the coupling between two tips as their separation progresses into the sub-nm quantum regime and below.

As previously stated, light can be confined below the diffraction limit by exploiting plasmons. By transferring energy from a diffraction-limited photonic field into collective oscillations of conduction electrons, an enhanced electric field can be generated on the surface of a metallic nanostructure with nanoscale localisation. It is through the understanding and application of this phenomenon that nano-optics and sub-wavelength confinement is made possible. This chapter deals firstly with a theoretical description of electromagnetic fields and the optical properties of metals. From this basis the concept of a plasmon can be introduced and the different kinds of plasmons defined, illustrating how they interact within different spatial regimes. Through this behaviour, the study of charge transfer in plasmonic systems, specifically quantum charge transport, is addressed. Finally, the plasmonics of metallic tips is discussed in preparation for the experiments described in later chapters studying plasmon interaction through each of the characteristic spatial regimes.

2.1 Plasmons

Plasmons are a direct solution of Maxwell's equations at the boundary between a dielectric and a metal. Despite existing on length scales from 100 nm down to around 1 nm, the high free electron density of metals mean energy levels still retain their characteristic continuous conduction bands and quantisation effects can be ignored.¹ Hence, classical theory is able to accurately describe physical phenomena until the characteristic length scale drops below ~ 0.5 nm and a phenomenological approach using Maxwell's equations forms the basis of the mathematical description of plasmons.

¹A higher density of states means that energy levels are more closely spaced, hence metals with a large free electron density appear to have an energy continuum as opposed to discrete energy bands or levels at room temperature.

2.1.1 Electromagnetic Waves

Maxwell's equations universally describe the classical, dynamical behaviour of electromagnetic (EM) waves, representing the foundations of electromagnetism. In their differential form they are given by, where \mathbf{E} is the electric field, \mathbf{B} is the magnetic flux density, ε_0 is the permittivity of free space, μ_0 is the permeability of free space, ρ_{tot} is the (volume) charge density, \mathbf{J} is the current density and t is time. The variables ε and μ are the relative permittivity and permeability, respectively, and describe the electromagnetic properties of the medium in which the fields exist. The *electric displacement field* \mathbf{D} and the *magnetic field* \mathbf{H} can be introduced to include material dependencies and describe macroscopic fields, which are defined by, where \mathbf{P} is the polarisation (dipole moment per unit volume) and \mathbf{M} the magnetisation. Equations Eq. ?? and Eq. ?? can then be redefined as, to describe macroscopic EM fields within media. The charge and current densities now refer to only the external contributions, related to the internal contributions via $\rho_{\text{tot}} = \rho_{\text{ext}} + \rho_{\text{int}}$ and $\mathbf{J}_{\text{tot}} = \mathbf{J}_{\text{ext}} + \mathbf{J}_{\text{int}}$.

The displacement field arises due to polarisation of a material in response to an applied field and is related to the internal charge density by $\nabla \cdot \mathbf{P} = \rho_{\text{int}}$. Conservation of charge means that $\nabla \cdot \mathbf{J} = \partial \rho / \partial t$, which requires that $\mathbf{J} = \partial \mathbf{P} / \partial t$ (a result also achievable by differentiating Eq. ??). The final equation of importance is the relationship between the electric field and the current density, given by, where σ is the conductivity. These few relations are sufficient to understand the behaviour of electromagnetic waves in media.

Propagation of EM waves within a medium is governed by a wave equation relating both the spatial and temporal changes of a wave. Combining Eq. ?? and Eq. ?? leads to the general wave equation for EM waves in the time domain,² describing the propagation of an EM wave in a given medium. In the absence of both charge and current Eq. ?? reduces to, describing a wave propagating in both space and time with a velocity $v = 1/\sqrt{\varepsilon_0 \varepsilon \mu_0 \mu}$. In free space ($\varepsilon = \mu = 1$) this is the speed of light $c = 1/\sqrt{\varepsilon_0 \mu_0}$, with light slowed when in media to $v = c/\tilde{n}$ by a factor $\tilde{n} = \sqrt{\varepsilon \mu}$ known as the refractive index.

In general ε is a complex quantity, $\varepsilon = \varepsilon_1 + i\varepsilon_2$, and depends on the frequency of the EM wave, ω . Plasmons are a phenomenon resulting from this frequency dependence in metallic materials. The relative permittivity is therefore denoted $\varepsilon(\omega)$ and is referred to as the material's dielectric function from this point onwards. The concept of a plasmon can be discerned through this function alone. Equations are therefore simplified by setting $\mu = 1$ and removing any magnetic contributions. Since $\varepsilon(\omega)$ is a complex parameter with components $\varepsilon_1 + i\varepsilon_2$, the complex refractive can be expressed as $\tilde{n} = \sqrt{\varepsilon(\omega)} = n + i\kappa$, where n is the real part causing refraction and κ is the loss coefficient determining absorption in the medium. The complex refractive index and the dielectric function are then related via $\varepsilon_1 = n^2 - \kappa^2$ and $\varepsilon_2 = 2n\kappa$.

The dispersive properties of a material are found by solving Eq. ?? with $\varepsilon = \varepsilon(\omega)$, describ-

²Derived using $\nabla \times \nabla \times \mathbf{E} = \nabla(\nabla \cdot \mathbf{E}) - \nabla^2 \mathbf{E}$

ing the behaviour of a wave propagating through a non-magnetic, dielectric medium. For a propagating EM wave with frequency ω and wave vector \mathbf{k} in space \mathbf{r} of the form, Eq. ?? can be expressed in the frequency (Fourier) domain as,³ where $k = |\mathbf{k}|$ is the magnitude of the wavevector. The variable $k_0 = \omega/c$ is sometimes used in Eq. ?? when all quantities considered are wave vectors. From this equation the propagation behaviour of EM waves in media can be described.

Solutions to Eq. ?? depend on the orientation of the wavevector with the field. Transverse wave solutions ($\mathbf{k} \cdot \mathbf{E} = 0$) yield the dispersion relation for light, Inserting this into Eq. ?? gives a general solution for light propagating through a dielectric medium, The real component of the refractive index n slows the wave whereas the imaginary component corresponds to an exponential decay with characteristic length $1/\kappa$, representing loss within a medium.

Longitudinal wave solutions ($\mathbf{k} \cdot \mathbf{E} = k|\mathbf{E}|$) result in $\sqrt{\varepsilon(\mathbf{k}, \omega)}\omega/c = 0$, hence solutions only exists for $\varepsilon(\mathbf{k}, \omega) = 0$. Both these conditions are important when describing plasmons in the bulk of a metal (only longitudinal plasmons are supported) and on the surface (both transverse and longitudinal plasmons supported).

Lastly, it should be noted that if the material dielectric properties in ε are linear then \mathbf{D} can be expressed in Fourier space as,⁴ Combining Eq. ?? with the differential of Eq. ??, Eq. ?? and Eq. ??⁵ yields a relation between a material's conductivity and it's dielectric function, Both quantities are able to describe the same physics from a different perspective.⁶ Since $\text{Re}[\varepsilon]$ is related to both $\text{Im}[\sigma]$ and $\text{Re}[\tilde{n}]$, $\text{Re}[\sigma]$ must therefore be related to $\kappa = \text{Im}[\tilde{n}]$ and the attenuation of waves inside media. A large conductivity in a material therefore corresponds to large transmission losses with decay attributed to energy transfer to move electrons at the surface of the material. Furthermore, the relation between $\varepsilon(\omega)$ and σ becomes important when considering points of conductance in a plasmonic system and that plasmons exist as an oscillating current.

Using the framework outlined so far the optical properties of metals can be deduced along with the existence of plasmons. The discussion begins with the Drude model for the optical response of metals [15], which is used to first predict the behaviour of plasmons. From there the distinction can be made between plasmons within the volume of a metal and those confined to the surface, which are of most interest in plasmonics.

³Derived using the identities $\nabla \times \nabla \times \mathbf{E} = \nabla(\nabla \cdot \mathbf{E}) - \nabla^2 \mathbf{E}$, $\nabla^2 \mathbf{E} = -k^2 \mathbf{E}$ and $\partial^2 \mathbf{E} / \partial t^2 = -\omega^2 \mathbf{E}$ where $\nabla \cdot \mathbf{E} = 0$

⁴Metals are linear in this regime so this expression holds

⁵ $\partial / \partial t \rightarrow -i\omega$ and $\mathbf{J} = \dot{\mathbf{D}} - \varepsilon_0 \dot{\mathbf{E}} = \varepsilon_0 \dot{\mathbf{E}}(\varepsilon - 1) = \sigma \mathbf{E}$

⁶Choice of which variable to use is a matter of convenience and tradition. Either can be used to equally describe the electromagnetic response of a material. The conductivity is typically used to describe lower frequency phenomena while the dielectric function is used at higher frequencies.

2.1.2 Bulk Plasmons and the Optical Properties of Metals

Before studying the concept of a surface plasmon it is important to understand the optical properties of metals as bulk materials. The optical properties of a metal are dominated by the response of nearly-free electrons delocalised from the positive nuclei background. When light is incident on a metal, nearly free electrons at the surface respond to the field and are displaced in the opposite direction (since $\mathbf{F} = -e\mathbf{E}$). The field of the induced charge distribution cancels the electric field inside the metal. An EM wave impinging on a metal is internally screened, and therefore externally reflected,⁷ through the displacement of free electrons inside the metal surface. The strong reflectance gives metals their shiny appearance. This behaviour originates from Eq. ??, where a high conductivity reduces the field penetration inside the metal. The exponential decay of the wave into the metal, shown in Eq. ??, is characterised by the skin depth $\delta_m = c/2\omega\kappa$, the point at which the field has decayed by $1/2e$ of its original value.⁸ Light transmission through a metal becomes heavily attenuated once its thickness becomes greater than δ_m . The small values of δ_m exhibited by metals means that they fall within the *perfect conductor* approximation (zero internal field).

A metal starts to show a more “dielectric-like” behaviour when the frequency of incoming light is high enough that the inertia of the electrons means they cannot respond instantaneously, preventing screening and thus transmitting the incident light. Such effects begin to be seen in the visible region of the EM spectrum in the case of noble metals. Fields increasingly penetrate the metal up until ultraviolet (UV) photon energies, at which point most metals become transparent. This is known as the *ultraviolet transparency*.

Since the dominating cause of these effects stems almost exclusively from nearly free electrons, as opposed to bound electrons,⁹ the optical properties of metals can be classically described by the Drude model [15]. This model describes the motion of a free electron gas in response to an applied field. The equation of motion for a single electron in a time-varying applied field is given by, where m is its effective optical mass and $\gamma = 1/\tau$ is the electron collision frequency, the inverse of the relaxation time, τ . Using an effective optical mass as opposed to the actual electron mass incorporates band structure effects into the model. The electron collision frequency amounts to an effective coefficient of damping as in a mechanical oscillator. Inserting a harmonic driving field and assuming a similar oscillatory behaviour in the free electron displacement ($\mathbf{x} = \mathbf{x}_0 e^{-i\omega t}$) leads to a solution, There is a resulting polarisation $\mathbf{P} = -n e \mathbf{x}$ induced in the free electron gas, where n is the density of electrons. The

⁷Light excites electrons into a higher energetic state leading to re-emission upon decaying back to the ground state, or from a different point of view, the prevention of light from entering the metal means the incident field must be reflected.

⁸The skin depth is defined using $1/2e$ rather than $1/e$ to consider power instead of field.

⁹Optical properties derived from bound electrons are described by a Lorentz oscillator model.

./2_theory/./figures/dielectric_function.pdf

Figure 2.1: Plot of the dielectric function, given by the Drude model, for Au and Ag compared with empirical data. $\varepsilon(\omega)$ is calculated using Eq. ???. The plasma frequency is calculated using Eq. ??. The parameters of the curves are $n = 5.90 \times 10^{28} \text{ m}^{-3}$, $m = 9.11 \times 10^{-31} \text{ kg}$, $\gamma = 1/\tau = 1/1 \times 10^{-14} \text{ s}$ and $\varepsilon_\infty = 8$ for Au and $n = 5.86 \times 10^{28} \text{ m}^{-3}$, $m = 9.11 \times 10^{-31} \text{ kg}$, $\gamma = 1/\tau = 1/3 \times 10^{-15} \text{ s}$ and $\varepsilon_\infty = 3$ for Ag. Empirical data (Johnson and Christy, 1972 [16]) is shown for comparison to illustrate the importance of interband transitions. Differences between the Drude model (solid lines) and experimental results (circles) are caused by interband transitions not included in the basic Drude formalism.

resulting displacement field, obtained by substituting Eq. ?? into Eq. ??¹⁰, defines the dielectric function of a metal, where ω_p is the plasma frequency of the metal, given by, The optical properties of a metal can be discerned from the real and imaginary components of $\varepsilon(\omega)$, given by, The plasma frequency defines the point at which the metal transitions into a dielectric. For $\omega < \omega_p$, $\text{Re}[\varepsilon(\omega < \omega_p)] < 0$ and a free electron gas remains metallic in character, with electrons moving to oppose an incident field. Once $\omega > \omega_p$ the free electron gas, limited by inertia, cannot respond fast enough to the field and the metal becomes dielectric in character. For an ideal free electron gas with negligible damping the simplified expression, is often used. This is the often the case for optical frequencies close to ω_p where the imaginary component of $\varepsilon(\omega)$, dominated by $\omega\tau \gg 1$, becomes negligible. In reality, however, interband transitions in real metals increase $\text{Im}[\varepsilon(\omega)]$. The expression for the dielectric function can be modified to account for interband absorption caused by bound electrons by the inclusion of a constant ε_∞ . The dielectric function then has the form,

A plot of Eq. ?? is shown in Figure 2.1, along with empirical data, illustrating both why noble metals exhibit high quality, visible spectrum (400–700 nm, 1.5–3 eV) plasmonics, as well as the failings of the Drude model. Noble metals have $\text{Re}[\varepsilon(\omega)] < 0$ and small $\text{Im}[\varepsilon(\omega)]$ in the visible region, hence behave very similarly to an ideal free electron gas. The Drude model fails at higher energies as interband transitions are not included in the basic model. These transitions increase the absorption ($\propto \text{Im}[\varepsilon(\omega)]$) and are significant for $\lambda < 500 \text{ nm}$ in Au and

¹⁰Derived from $\mathbf{D} = \varepsilon_0 \mathbf{E} + \mathbf{P} = \varepsilon_0 \mathbf{E} - [ne^2/m(\omega^2 + i\gamma\omega)]\mathbf{E} = \varepsilon_0 \varepsilon(\omega) \mathbf{E}$

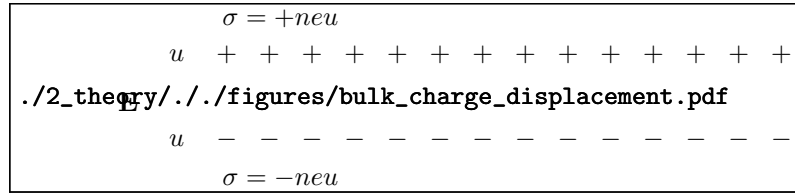


Figure 2.2: Charge displacement of a free electron gas under an applied field. The optical electric field displaces the electrons leaving behind the positive cores. The slab becomes polarised with opposing surface charge densities σ . The charge oscillations resonate when the field frequency is ω_p .

$\lambda < 300$ nm in Ag. A measure of the quality of a metal can be determined from its quality factor $Q = |\text{Re}[\varepsilon] / \text{Im}[\varepsilon]|$. The high Q of noble metals in the visible regions means they can easily respond to an incident field and screen it, behaving metallicity.

The plasma frequency ω_p in $\varepsilon(\omega)$ not only describes a metal-to-dielectric transition but also dictates the frequency of the collective longitudinal mode of oscillation. By substituting Eq. ?? into the dispersion relations for transverse and longitudinal waves it is clear that transverse waves are only supported if $\omega > \omega_p$ with a dispersion $\omega^2 = \omega_p^2 + k^2 c^2$. However, a collective longitudinal oscillation is allowed at $\omega = \omega_p$ since $\varepsilon(\omega) = 0$ in the absence of damping. In this case the free electron gas is displaced from the ionic core background a distance u due to the applied field to form surface charge densities $\sigma = \pm neu$ (Figure 2.2). The resulting depolarisation field¹¹ is $E = neu/\varepsilon_0$ and the motion of the free electrons is defined by, Simplifying this relation leads to, hence ω_p is considered the natural frequency of the system and the electrons resonate when driven at $\omega = \omega_p$. This is known as the bulk or *volume plasmon*. Since this is a longitudinal oscillation, however, light cannot couple with it. For this reason, volume plasmons cannot be excited and measured by means of optical techniques but require other experimental methods (e.g. electron energy loss spectroscopy (EELS) [17]). Optical plasmonic phenomena must therefore be a result of a different kind of plasmon.

2.1.3 Surface Plasmons

Surface plasmons (SPs), unlike bulk plasmons, are collective oscillations of conduction electrons tightly confined to the surface of the metal. As stated previously, light at an interface is not necessarily restricted by the diffraction limit. The maximum magnitude of the wavevector is set by $k_0 = 2\pi/\lambda$ with individual components restricted by $k = \sqrt{k_x^2 + k_y^2 + k_z^2}$. Consider Eq. ?? in the form, If a wave propagates freely in all three dimensions then it remains diffraction limited and the propagation constant $k_x < \tilde{n}k_0$. However if one or more of its wavevector

¹¹Gauss' law $\int \mathbf{E} \cdot d\mathbf{A} = Q/\varepsilon_0 = \sigma A/\varepsilon_0$, hence $E = \sigma/\varepsilon_0$. Alternatively $D = 0 = \varepsilon_0 \mathbf{E} + \mathbf{P}$ therefore $\mathbf{E} = -\mathbf{P}/\varepsilon_0 = -neu/\varepsilon_0$.

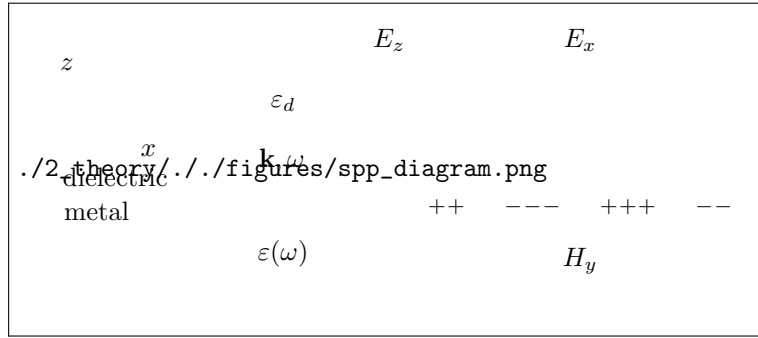


Figure 2.3: Diagram of a surface plasmon polariton (SPP). TM surface electron density waves (surface plasmons) couple with an evanescent wave originating from an EM wave to form a SPP. The SPP remains confined to the interface but can propagate across the surface.

components become imaginary ($k_{y,z}^2 < 0$) then it becomes possible that $k_x > \tilde{n}k_0$. This behaviour can occur at an interface, where surface waves take on evanescent character in the z -direction whilst propagating in the xy plane.¹² By coupling light into surface waves the diffraction limit can be beaten. Waves of frequency ω can acquire wavelengths many times smaller than their excitation wavelength. The SP is one such case of this phenomenon and occurs at metal-dielectric interfaces. Unlike in a bulk metal, electrons displaced by an applied field at the surface of a metal feel a restoring force due to the positive nuclei background. Transverse fields impinging on the metal surface at an angle are then able to manipulate the electron motion. SPs can therefore be excited by light as well as by the longitudinal waves needed to excite bulk plasmons, forming polariton quasiparticles under strong coupling with photons.¹³ This optical excitation is known as the surface plasmon polariton (SPP) and, as a result of it being optically accessible, is one of the most commonly studied plasmonic phenomena.


Surface Plasmon Polaritons

A SPP is a propagating transverse magnetic (TM) wave confined to the surface of a metal - the bound state between a photon and a SP. The TM nature of the wave indicates that \mathbf{E} has a component traversing across the interface as shown in the diagram of a SPP in Figure 2.3. No such solution exists for transverse electric (TE) surfaces waves (i.e. a component of \mathbf{H} passing through the interface).¹⁴ While confined in two dimensions to the planar boundary between a metal and a dielectric, the SPP can either propagate or become stationary as a result of interference **with itself or other plasmons**. The latter stationary form of the SPP is similar to the localised surface plasmons, described later.

¹²Evanescent meaning imaginary k_z therefore exponentially decaying amplitude in the z -direction.

¹³Polaritons are the name given to quanta or quasiparticles of light-matter interactions. Strong coupling describes the point at which a quasiparticle is no longer distinguishable between its two constituent components.

¹⁴TE and TM are also known as s - and p -polarisations, respectively.



./2_theory/./figures/spp_dispersion.pdf

Figure 2.4: Plasmon dispersion relations for the SPP and LSP. The dashed lines indicate the dispersion of light in both glass and air (vacuum) along with the surface plasmon frequency. SPPs can be described as photon-like or plasmon-like depending on their point of excitation. SPPs excited with large k and $\omega \approx \omega_{SPP}$ are considered plasmon-like while SPPs with low k are considered more photon-like. These have been known as Sommerfeld-Zenneck surface waves [18].

The SPP itself is described through its dispersion. As a TM wave propagating in the x -direction along a metal/dielectric interface, it has a spatial field profile in a space \mathbf{x} given by $\mathbf{E}(\mathbf{x}) = \mathbf{E}(z)e^{i\beta x}$ where $\beta = k_x$ is the propagation constant. The magnetic field in this configuration is then $\mathbf{H}(\mathbf{x}) = \mathbf{H}(y)e^{i\beta x}$. The behaviour of such a wave in Eq. ?? is described by, Both equations can be related using Eq. ?? and Eq. ?. Assuming a TM wave ($\partial E_y / \partial z = 0$, $\partial H_z / \partial z = 0$), propagating only in the x -direction with symmetry in y -direction, results in the field relations, In this instance the TM wave equation, and requirement for evanescent decay in the z -direction, mean that $H_y = A_d e^{i\beta x} e^{-k_{z,d} z}$ for $z > 0$ (in the dielectric) and $H_y = A_m e^{i\beta x} e^{k_{z,m} z}$ for $z < 0$ (in the metal). The components of the electric field can therefore be expressed as, inside the dielectric and, inside the metal, where $\varepsilon_m = \varepsilon(\omega)$ in the previously used notation. Continuity across the boundary ($z = 0$) dictates that $A_d = A_m$ and yields the relation, hence the ratio between wavevectors inside and outside of the metal depends on the relative change in dielectric constant across the boundary. It is this continuity relation that allows for the existence of SPPs in the TM configuration.¹⁵ To determine the SPP propagation constant β a further relation is needed to fix the wave vectors in a given medium with respect to the dielectric constant. Using the expression for H_y in the wave equation Eq. ?? yields a set of relations, which, when combined with Eq. ??, fully describe the fields around the interface. The propagation constant is then given by, This is the dispersion relation for a SPP, as is shown in Figure 2.4 along with the dispersion of light for both air and glass mediums.

From the dispersion curve it is clear that SPPs cannot couple with light within the same

¹⁵No such continuity equation exists for TE waves, hence SPPs cannot exist in this configuration.

medium as their dispersion curves do not cross. However, light from within a higher refractive index medium such as glass can generate evanescent waves and excite SPPs on a nearby metal/air interface. This method of coupling photons with surface plasmons, depending on the specific prism arrangement, is known as the Kretschmann (prism-metal-dielectric) or Otto (prism-dielectric-metal) configuration [19, 20]. Since a diffraction grating may also impart momentum onto a photon ($k_x \rightarrow k_x + n\pi$) a metallic grating can launch SPPs along a planar metal-dielectric interface. This phenomenon was first observed in 1902 by Wood, dubbed as Wood's anomaly [21], and only explained via surface waves many years later [22].

Closer inspection of the curve highlights one of the major features of a plasmon. While SPPs retain the frequency of the excitation field, their wavelength is considerably smaller than the diffraction-limited wavelength of light. Depending on where on the curve the SPP lies it can be considered to be either more photon-like or more plasmon-like. For small $\beta \approx k_0$ the SPP is similar to light grazing the interface (Sommerfeld-Zenneck waves)¹⁶ whereas SPPs with large k become more plasmon-like and their frequency saturates at the surface plasmon frequency. At this point the SPP can be considered electrostatic and becomes a SP. To some extent, SPs confined to a finite, continuous, non-planar surface, defining a nanoparticle (NP), can be considered to be the basis for a localised surface plasmon (LSP) or localised surface plasmon polariton (LSPP).

Localised Surface Plasmons

LSPs are collective oscillations of conduction electrons confined within a fixed sub-wavelength spatial extent. These can occur on any nanoscale curved surface but the effects are strongest, and most well-documented, on the surface of a metallic nanoparticle (MNP). Free electrons are displaced from the nuclei in response to an applied field and form a surface charge distribution, polarising the particle. Coulomb interaction between the poles of the surface charge distribution results in a restoring force within the particle. This gives rise to a natural frequency of oscillation, leading to a SPR when driven harmonically at the correct frequency. The particle geometry sets which multipolar surface charge distributions are supported, while its material properties and the dielectric properties of the surrounding medium set the restoring force. Each different multipolar charge distribution is therefore considered to be a unique LSP mode, identifiable by its SPR [23].

The simplest form of a LSP is the dipole resonance of a spherical MNP. Assuming the sphere radius $a \ll \lambda$ (the wavelength of light), the particle is considered to be in the quasi-static regime, where electrons move instantaneously in response to the incident field and its phase is ignored. Electrostatics, rather than electrodynamics, then becomes applicable to solve

¹⁶Sommerfeld-Zenneck waves are surface waves that appear throughout mechanics and electromagnetism that are confined to the interface between two different mediums.

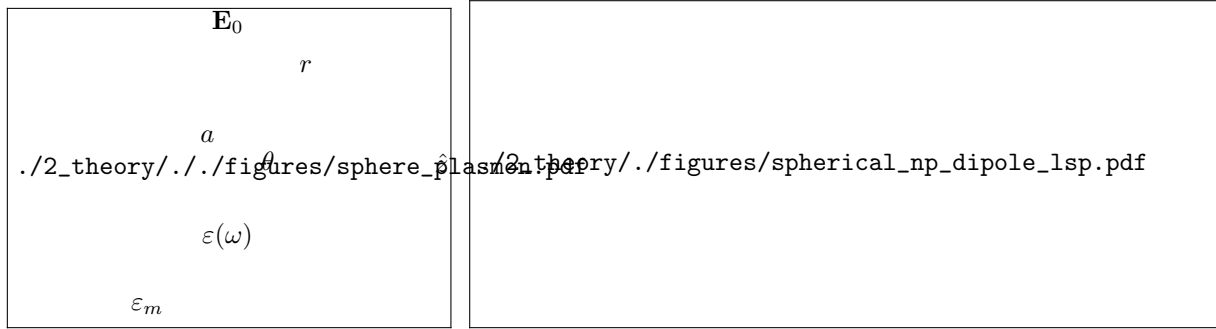


Figure 2.5: A spherical metallic particle in an applied electric field. The sphere is assumed to be in the quasistatic regime ($a \ll \lambda$). The aura around the particle indicates the phase of the free electron oscillations in the plasmon. Calculations of (a) the potential and (b) the magnitude of the electric field for a spherical nanoparticle on resonance ($\varepsilon(\omega) = -2\varepsilon_d$).

the problem. The electrostatic potential, φ , of the system is described by the Laplace equation, $\nabla^2 \varphi = 0$, with a general solution in a spherical geometry of the form [24], where l is the degree of spherical harmonic and m_l its projection, A_l and B_l are constants and $P_l^m(\cos \theta)$ are associated Legendre polynomials. For a sphere of radius a and dielectric function $\varepsilon(\omega)$ in a dielectric medium described by ε_d the solution is fixed by the boundary conditions $\varphi_{\text{out}} \rightarrow -E_0 z$ as $r \rightarrow \infty$ and $\nabla \varphi_{\text{in}}(r)|_{r=a} = \nabla \varphi_{\text{out}}(r)|_{r=a}$. This reduces to a solution [25], For a metal sphere the potential (plotted in Figure 2.5a) describes an induced dipolar surface charge distribution. The description is simplified by defining the dipole moment, where the polarisability, α , incorporates the frequency dependent behaviour and is defined as, The outside potential is then expressed as, This is simply the potential of an induced dipole superimposed onto the incident field. The electric field inside and outside of the sphere, calculated using $\mathbf{E} = -\nabla \varphi$ and given by, where $\mathbf{n} = \mathbf{r}/r$ is the radial unit vector, shows a similar phenomenon and is shown in Figure 2.5b.

Provided that the quasistatic approximation remains valid, the electrostatic result is simply multiplied with a harmonic time dependence to describe electrodynamic behaviour. An EM wave therefore induces a coherent, oscillating dipole moment $\mathbf{p}e^{i\omega t} = \varepsilon_0 \varepsilon_d \alpha \mathbf{E}_0 e^{i\omega t}$. The behaviour of electrons in the spherical MNP at optical frequencies, described using the dielectric function $\varepsilon(\omega)$, is then simply incorporated into $\alpha(\omega)$. For a good metal $\text{Re}[\varepsilon(\omega)] < 0$ and the denominator in Eq. ?? undergoes resonance¹⁷ at the Fröhlich condition when, This corresponds to excitation of a collective oscillation of conduction electrons on the surface of the sphere - the dipolar LSP. Its magnitude in real metals is restricted by damping of the electron motion leading to a Lorentzian-shaped resonance band - the dipolar SPR. Its relationship with ε_d means that the SPR can be tuned by varying the external dielectric medium. As seen in Eq. ??, the field from the induced dipole moment of the plasmon is superimposed onto the incident field leading to a resonant enhancement, both inside and outside the surface

¹⁷ $\alpha \rightarrow -\infty$ when $\varepsilon(\omega) + 2\varepsilon_d \rightarrow 0$

of the sphere. This is one of the fundamental properties of the plasmon, and one that is most exploited in sensing and sensor developments.

In the Drude model, with $\varepsilon(\omega)$ given by Eq. ??, the Fröhlich condition is satisfied when, which evaluates to $\omega = \omega_p/\sqrt{3}$ for a MNP in vacuum. As can be seen in Figure 2.4, the flat dispersion of a LSP mode means it crosses the light line at a single point. Light of the correct frequency therefore readily couples with LSPs without the need for SPP momentum matching mechanisms. In general, the optical spectrum of a MNP can contain a number of multipolar plasmon modes for which the resonant frequencies are given by [26], where the degree of spherical harmonics l denotes the charge distribution of a specific mode ($l = 1$ for dipole, $l = 2$ for quadrupole, etc.). However, these modes only exist outside of the quasistatic regime in larger MNPs or more complex geometries. For nobles metals, such as Au and Ag, the fundamental $l = 1$ mode occurs in the visible region of the EM spectrum ($\lambda = 520$ nm for Au and $\lambda = 360$ nm for Ag in vacuum or air [24], redshifted in the presence of other media [27]), leading to them often being the plasmonic metal of choice. Additionally, the polarisability changes with NP geometry due to differing restoring forces acting on the surface charge distribution. Changes from a spherical shaped NP therefore lead to tuning of the SPRs across the visible spectrum. This geometrical dependence is well known [28–30] and has been exploited in many applications over the past decade, e.g. infrared (IR) photothermal therapy [31–33].

The larger the separation between opposing poles of surface charge, the weaker the restoring force. A larger particle, or similarly an elongated particle (a nanoellipsoid or nanorod), will therefore have lower energy resonances. Simple changes can be made to the theoretical (quasistatic) model to account for an ellipsoidal geometry, and thus somewhat understand the geometrical dependencies incorporated into the polarisability. Insertion of a geometrical correction to the polarisability leads to the definition [24, 34], where i is the index of each anisotropic axis with a geometrical factor, The resonance condition along each axis then becomes, By increasing the size of an axis, decreasing its associated geometrical factor, the resonance condition decreases from $\varepsilon(\omega) = -2\varepsilon_d$, redshifting the SPR. The more elongated the particle becomes, the larger the redshift until the restoring force is weakened to the point that each lowest-order antenna SPR no longer exists.

Optical Observation of Surface Plasmon Resonances

Depending on the microscopic dipole moment of excited plasmons, their fields can be radiative and hence macroscopically observable. This depends on the geometry of the plasmons time-varying charge distribution. Antenna-like dipolar plasmons bear similarity with the Hertzian dipole, an infinitesimal oscillating current source which both absorbs and radiates EM waves. The relationship between the current, $\mathbf{I}(t)$, carried by the dipole of length d and the radiative

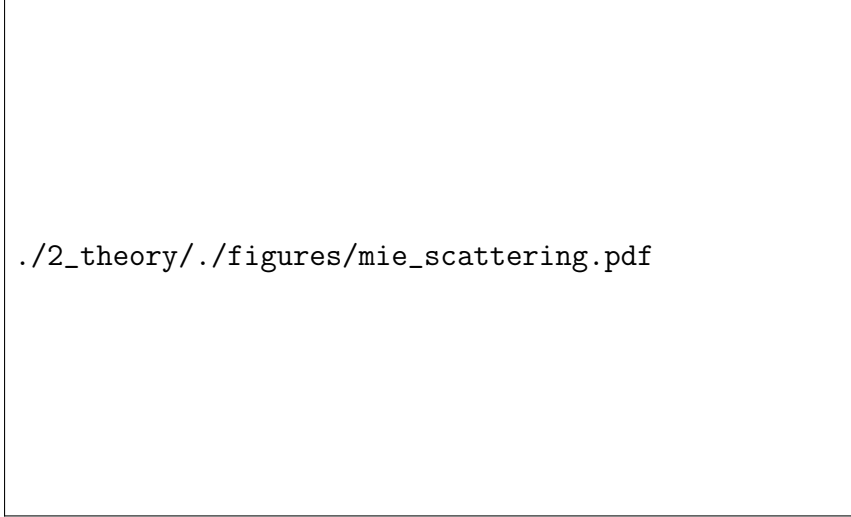
electric field around it is given by [35], The radial behaviour of the electric field around an object can be split into three distinct regimes - the *near-field*, Fresnel regime and the *far-field* or Fraunhofer regime. At short distances the $(kr)^{-2}$ term dominates to form the near-field but quickly falls off with increasing distance. The remaining $(kr)^{-1}$ term defines the far-field. The Fresnel regime forms the intermediate stage between the two. The boundary between the near-field and the far-field is defined as the point at which $kr = 1$ where $r = \lambda/2\pi$ (hence why sub-wavelength optics deals with the near-field).

Plasmons similarly have the ability to both resonantly absorb and scatter incident fields. The absorbance and scattering cross sections determining interaction with a spherical MNP are given by [36], Since $\sigma_{\text{scat}} \propto V^2$ and $\sigma_{\text{abs}} \propto V$, absorption dominates in smaller particles whilst larger particles scatter more strongly. The extinction cross section, commonly used in spectroscopy, can be calculated using $\sigma_{\text{ext}} = \sigma_{\text{scat}} + \sigma_{\text{abs}}$. The size of each cross-section, i.e. the spatial extent over which light interacts with the MNP, depends on α and is increased on resonance. Hence, MNPs optically appear strongly coloured and much larger than they actually are.¹⁸

For example, when on resonance with the dipolar LSP, both cross sections are enhanced by the polarisability resonance from $\mathcal{O}(a \sim 50 \text{ nm})$ to $\mathcal{O}(500 \text{ nm})$. The increased size of the cross-section is comparable to the wavelength of light, meaning LSPs efficiently couple with photons in the far-field. The LSP mediates energy transfer between the near-field and the far-field and acts to match the electromagnetic modes of nanoscale absorbers/emitters, such as phonons (Raman) and radiative energy levels (quantum emitters, fluorescence), with those of a diffraction-limited photonic mode via an oscillating charge density [37]. A plasmonic NP is often therefore described as an *optical antenna* in a similar manner to a device that converts between radio waves and an electrical current is named a radio antenna [9, 38]. LSP modes which readily couple with the far-field are then sometimes referred to as *antenna modes* and become important when designing resonant structures for specific sensing applications.

Whilst the quasistatic approach is useful to first demonstrate the field enhancing capabilities of a MNP, the description breaks down once the size of the particle becomes closer to the excitation wavelength. Retardation effects between the field and the electrons mean that phase differences between the charge oscillations and the incident field become important. At this point Mie theory (electrodynamics) [39] is required to describe the spectral response of spherical MNPs. Mie theory provides a more general description of the optical response of spherical MNPs. Using this approach the spectrum of a MNP can be decomposed into superimposed multipoles, alluding to the existence of higher order LSP modes in larger MNPs. The spectral response of spherical AuNPs of varying sizes is shown in Figure 2.6, demonstrating the

¹⁸Consider that σ_{scat} for a AuNP is enhanced $100\times$ on resonance, meaning it's area cross-section is $\sqrt{100/\pi} = 6\times$ wider than it's radius, hence why a 50 nm AuNP looks like a 300 nm green sphere when imaged.



./2_theory/./figures/mie_scattering.pdf

Figure 2.6: Mie scattering cross-sections for AuNPs of increasing diameter. The 520 nm resonance position of the dipolar LSP mode of a AuNP in the quasistatic approximation is indicated by the dotted line. The resonance stays at 520 nm until $d > 80$ nm then redshifts. The emergence of higher order modes following a similar behaviour is seen once $d > 100$ nm.

redshift and broadening of lower order modes with increasing particle size and the excitation of higher order modes.

To summarise, by utilising the particle material, geometry and polarisation anisotropy its SPRs can be tuned across the entire UV–NIR spectrum to tailor to individual applications. However, even when exciting on resonance, a single particle can only provide a relatively small field enhancement. An alternative approach to exploiting LSPs is therefore to couple the fields of many plasmons together. Through coupling, the confined fields in nanometric-size gaps between MNPs can be enhanced by many more orders of magnitudes.

2.2 Plasmon Coupling

Both the resonant field enhancement and the confinement of a surface plasmon can be improved by bringing a second surface plasmon into close proximity. Similar to coupled harmonic oscillators and dipoles, plasmons couple together via Coulomb forces once brought together, forming normal modes of oscillation across interacting charge distributions. The charge distribution of the resulting normal modes depends highly on the particle separation and is strongly confined to the dielectric space between metallic surfaces where charges strongly interact. These normal modes are therefore more generally known as *gap plasmons* and lead to tuneable SPRs [40, 41] and significant increases in field enhancement, enabling single molecule spectroscopy [42, 43].

Coupled plasmons are a feature of many metallic nano-systems with closely spaced metal-dielectric interfaces, including metal-insulator-metal (MIM) and insulator-metal-insulator (IMI) ■

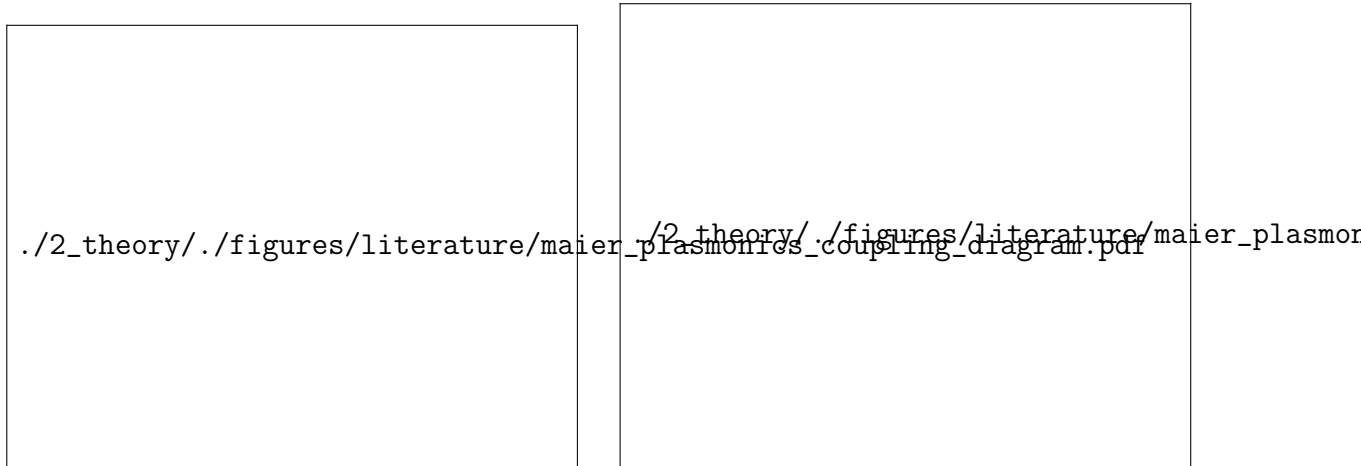


Figure 2.7: Experimental and theoretical plasmon coupling. Dipolar plasmons in chains of spherical AuNPs couple depending on field orientation [24] (left). Experimentally measured plasmon resonance energies in coupled AuNP chains show the gap-dependent tuning due to coupling [45] (right). The dotted line corresponds to a r^{-3} point dipole model.

waveguides [24, 44] and systems containing multiple MNPs [40, 41, 45–49] or nanoparticles-on-mirror (NPoM) [42, 50–54]. For the purposes of this work, discussion is restricted to the ideal case of coupled LSPs between two closely spaced MNPs, closely representing the experimental system, though the description of coupling is valid for many other cases involving SPs. Furthermore, in each example of coupled systems, the physics can be reduced to interactions between neighbouring charge distributions. Understanding the simple dimer system is therefore important to fully understand even more complex geometries.

In the simplest description, Coulomb interaction between the free electrons in adjacent metallic introduces an additional coupling force, pulling charge towards the gap between metallic surfaces. A greater amount of charge accumulates on the gap-facing metallic surfaces. As particles move closer together this force grows, more strongly confining the charge and increasingly polarising the gap region. The resonance frequency of the individual plasmon mode shifts from ω_0 by $\Delta\omega$ depending on the strength of coupling. The sign of $\Delta\omega$ depends on whether the coupling is attractive or repulsive. Similar to coupled oscillators, the two coupling configurations (normal modes) are the in-phase bonding and anti-phase anti-bonding modes. Compelling evidence for these modes has been seen many times, with particularly good results found using chains of AuNPs [45], as shown in Figure 2.7. In general, light drives the free electrons of two sub-wavelength particles in phase resulting in the bonding configuration and a redshifting coupled plasmon with decreasing interparticle separation.

The primary effect of this kind of plasmon coupling is increased confinement of the electric field to the dielectric gap medium, leading to much larger field enhancements that can be exploited for sensing. For a strongly confined gap mode there is very little field in the metal with almost all field confined within a small lateral mode within the gap [55]. This is known as

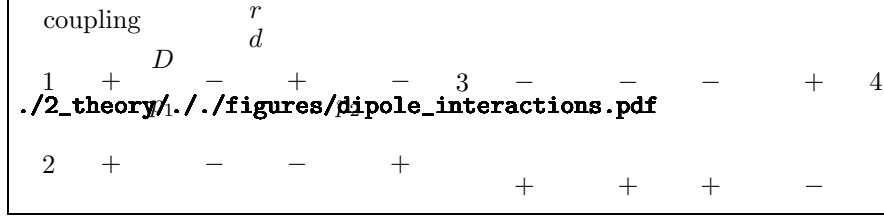


Figure 2.8: Diagram of dipole interactions. The distance between dipoles of length D is r with an edge-to-edge separation d . Configurations 1 and 3 are comparable with plasmon coupling as a result of sub-wavelength structures being driven by a single external light field. Configurations 2 and 4 are generally unphysical or non-radiative in plasmon dimers without asymmetry or phase retardation.

a plasmonic “hot spot”. Through this mechanism alone the field enhancement $|E/E_0|$ can be increased by more than an order of magnitude [56, 57]. Hence, in recent years, the interests of the plasmonics community have shifted from individual plasmonic nanostructures to coupled systems in order to maximise nano-optical performance. This has led to the progression into sub-nm plasmonic cavities, the study of which is a focus of this project. The development of a theoretical model for such small systems begins with the classical models of plasmon coupling with additional complexity added until quantum mechanical effects become apparent.

2.2.1 Classical Models of Plasmonic Coupling

Two analytical classical models exist to describe plasmon coupling. The first and simplest model continues the description of the dipole plasmon present in small (quasistatic) MNPs and introduces dipole-dipole interactions. The second model of plasmon hybridisation is more complex and successfully models higher order modes of charge oscillation.

Dipole-Dipole Model

In its simplest case, interactions between dipolar plasmons in small MNPs appear similar to dipole-dipole interactions [45, 46, 58–60]. These exhibit the same behavioural dependence on separation and relative orientation with respect to the incident field. Examples of some commonly considered dipole-dipole interaction geometries are shown in Figure 2.8. In each situation the electric field incident on a dipole \mathbf{p}_1 is perturbed by the presence of a second dipole \mathbf{p}_2 a distance r away, whose fields as given in Eq. ?? are superimposed onto the incident field at the location of \mathbf{p}_1 . The result is in an effective field given by, where \parallel and \perp denote the orientation of dipoles relative to the dimer axis. The sign of the second term in each equation determines the effect of coupling whilst its strength falls as r^{-3} due to $V \propto p_1 p_2 r^{-3}$ [61]. The polarisability of the MNP is then modified by the interaction field, changing the frequency at which it becomes resonant. For two dipoles aligned end-to-end ($p \parallel r$) and driven in phase, coupling is attractive (increased \mathbf{E} , Eq. ??), leading to a decrease (redshift) of the

resonant frequency. Conversely, the interaction between two dipoles aligned side-by-side ($p \perp r$) is repulsive (decreased E , Eq. ??), causing an increase (blueshift) of the resonant frequency. These describe the in-phase interactions between two dipole. Anti-phase configurations, as shown in Figure 2.8, behave in the opposite manner to the in-phase counterparts as the direction of the Coulomb force reverses. These configurations are often ignored in quasistatic dimers since light can only drive in-phase oscillations. Electron-based techniques such as EELS are instead used to probe these modes. Using EELS with AuNP chains, the validity of the dipole approximation was confirmed, showing good agreement with the experimental data shown in Figure 2.7 [45].

The dipole-dipole model is only an approximation to actual plasmonic coupling and does not adequately account for the spatial charge distribution. It can be somewhat improved by taking into account the finite particle size. Since the internal restoring force within particles, scaling as D^3 , contributes to the potential, the interaction energy goes as $(r/D)^{-3}$ as opposed to r^{-3} [62]. Furthermore, this quantity is redefined to better represent a dimer using the gap size, d , as $(d/D) = (r/D) - 1$. The resonant wavelength shift due to attractive coupling can then be approximated using a “plasmon ruler” equation [62, 63], where a is the coupling strength and τ is a decay constant. In essence, this model describes an interesting phenomenon - that plasmon coupling is scale invariant. Dimers comprised of larger particles interact more strongly for the same separation than smaller dimers. However, their relative shifts depend on how the gap size compares with the particle size. In recent years this relation still shows good agreement with experimental data but the approach remains limited to describing only dipolar modes in simple geometries [47].

Plasmon Hybridisation

A slightly more complex model, known as plasmon hybridisation, was developed between 2003 and 2004 to more generally explain the formation and behaviour of coupled modes [26, 64, 65]. In this model, plasmon resonances are mechanically modelled as resonant oscillations of an incompressible fluid confined within an equilibrium geometry [26]. The plasmon resonances of a more complex particle geometry are then solved by decomposing it into coupled resonances of two simpler particle geometries [26, 65]. This is done in analogy with the ideas underpinning molecular orbital hybridisation and the hybridisation of quantum energy states. Using this logic, the theory equally describes the plasmon resonances of two coupled simple particle geometries [64] or a particle coupled with its image charge in a surface [66]. Under these circumstances, the multipolar modes of each of the individual dimer particles energetically split into two hybridised modes representing the bonding (in-phase) and anti-bonding (anti-phase) configurations. This behaviour is shown in Figure 2.9.

Unlike the dipole-dipole model, plasmon hybridisation is capable of predicting higher order

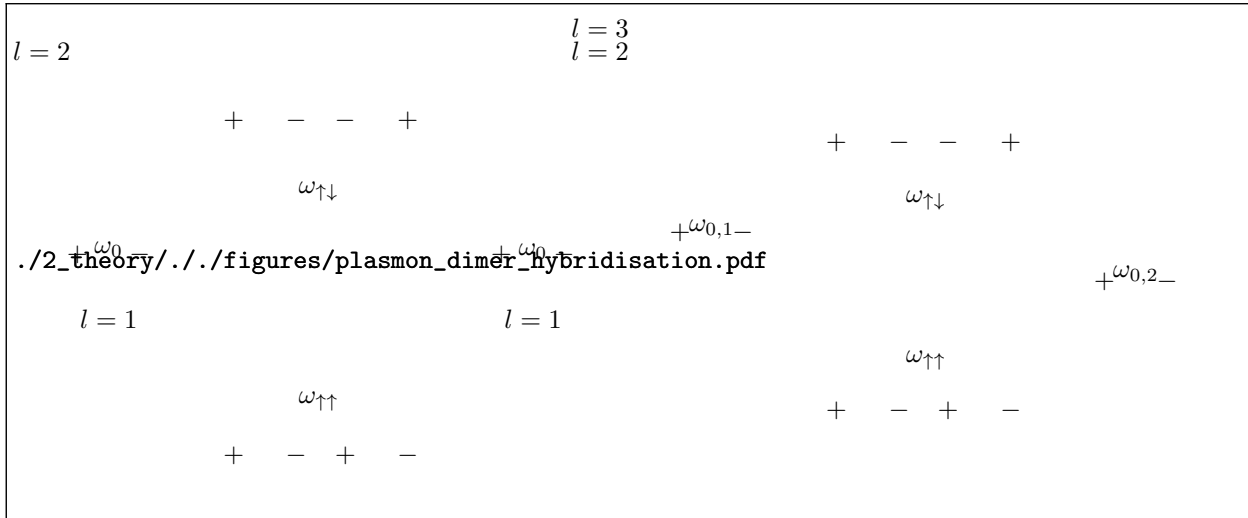


Figure 2.9: Diagram of plasmon hybridisation between coupled plasmons in a nanoparticle dimer. Plasmons are coupled along the dimer axis. Coupling leads to bonding and anti-bonding modes for each set of interacting l modes (left). Interaction with higher order l modes lowers the overall energy of lower order coupled modes (green lines). Only the bonding ($\omega_{\uparrow\uparrow}$) mode in the symmetric (homo-)dimer has a net dipole moment and is therefore observable. Cancellation of the net dipole moment means the anti-bonding ($\omega_{\uparrow\downarrow}$) mode remains optically dark. On the contrary, asymmetry in a (hetero-)dimer means both modes stay bright (right). In this case, the lower and higher energy individual modes shift to form the bonding and anti-bonding hybridised modes, respectively. This diagram is adapted from [64].

multipolar modes in a coupled dimer system as well as dealing with more complex geometries. It is therefore valid for describing larger dimer geometries and smaller gap sizes. As with dipole-dipole interactions, the bonding and anti-bonding hybridised modes redshift and blueshift from their initial mode positions upon decreasing the separation, respectively. These shifts in the plasmon energies are shown in Figure 2.10. However, the addition of higher order modes to the classical description of plasmon coupling, and their interaction with adjacent modes of similar energies, modifies the rates of each mode's shift, as shown by the green lines in Figure 2.9 [64]. These interactions leads to a further redshift of each affected mode, though only in the case of small gaps or larger particles when higher order modes are excited.

In each classical approach it is the resulting dipole moment of each coupled mode that dictates its radiative properties. The in-phase, bonding mode exhibits a large dipole moment and strongly couples with light whereas the anti-phase, anti-bonding mode has no net dipole moment in a symmetric, quasistatic system and thus remains dark. This remains the case until the anti-bonding dimer mode acquires a finite net dipole moment, either through particle asymmetry (difference material, size or shape) or phase retardation across the dimer (large particles, non-quasistatic),¹⁹ at which point it becomes more radiative and hence exper-

¹⁹Phase retardation of the driving field across the dimer breaks the coupling symmetry, allowing anti-phase modes to be excited.



Figure 2.10: Hybridised plasmon energy shifts for spherical AuNP dimers. Homodimer (left) and heterodimer (right) plasmon energies are calculated in both the axial (top) and transverse (bottom) coupling configurations. Spheres are 10 nm in diameter in the homodimer and 10 nm and 5 nm in the heterodimer.

imentally observable using optical methods. Alternatively, local excitation of specific charge distributions using EELS allows for measurement of dark modes [67, 68]. Should both bonding and anti-bonding modes be bright and gaps decrease enough that a blueshifting anti-bonding mode approaches on a higher order redshifting bonding mode, an anti-crossing will occur and modes exchange symmetry. This causes anti-bonding modes to eventually redshift into geometrical contact.

Whilst each of the previously described analytical models has found some success in describing experimentally observed plasmon coupling in simple systems, their approaches are limited in scope. Neither model directly calculates electrodynamics and solves the actual electromagnetic problem. Instead, they use analogies to similar electromechanical systems to provide a useful insight into the mechanism of plasmon coupling. The electrodynamics of a particular plasmonic problem are now often solved using computationally demanding, numerical techniques, in which the electrodynamics are solved at each boundary within a system.

2.2.2 The Dynamical Optical Response of Plasmonic Dimers: Transitioning from Capacitive to Conductive Plasmonic Coupling

Using modern numerical simulation techniques, such as the boundary element method (BEM) and finite-difference time-domain (FDTD) approaches, the full separation-dependent optical

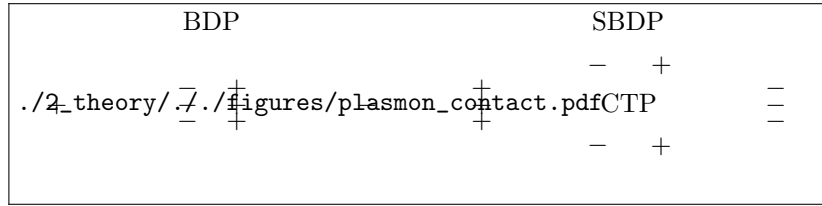


Figure 2.11: Diagram showing the emergence of charge transfer and screened bonding (crevice) plasmons on geometrical contact in a nanoparticle dimer. The field generated by the bonding dimer plasmon (BDP) is screened from the gap by the conductive contact, forcing capacitive coupling to the crevice gap in the form of the screened bonding dimer plasmon (SBDP). The dominant charge oscillation is then the charge transfer plasmon (CTP) through the conductive bridge and across the whole structure.

response of a plasmonic dimer has been calculated as particles transition from non-interacting to coupled through into geometrical contact [55]. In these calculations, the lowest order plasmons hybridise, redshift and more intensely scatter as the separation decreases, with higher order modes eventually emerging. Classically, this leads to a large number of modes being present in nanometric-size gaps. The lateral confinement of the field between particles of radius R separated by a gap of width d is estimated using \sqrt{Rd} [55]. As higher order modes become more intense, scattering from lower order modes decreases. Despite this, their field enhancement continues to rise [69]. These plasmons become so confined that they no longer couple with the far-field. This behaviour continues until particles are nearly touching into geometrical contact.

Once touching, bonding hybridised plasmons abruptly transition into charge transfer plasmons (CTPs) - charge oscillations spread across the full extent of the connected dimer. These are widely observed in geometrically contacted or overlapping plasmonic systems [46, 70]. A dipolar CTP emerges at lower energies as screened $l = i$ hybridised plasmons are expelled out of the gap, transitioning into $l = (i + 1)$ CTPs due to their similar charge distributions [55, 71–73]. Their resonances blueshift, diminishing in intensity and broadening in width as a result of significantly increased currents. The lower energies of CTPs are associated with a spatially larger dipole, as shown in Figure 2.11, indicating that they blueshift with increasing particle overlap. Their broad width compared with capacitively coupled plasmons is caused by dissipation in the junction and can be linked with behaviour described by Eq. ??.²⁰ As with the particle approach, a large continuum of higher order CTP modes is found in calculations of overlapping dimers with an abrupt formation on geometrical contact.

Classical predictions of plasmon coupling break down at small, sub-nm gaps where the continuum of excited higher order modes redshift to a singularity as $d \rightarrow 0$, and the field

²⁰For a spherical MNP dimer with a bonding hybridised dipolar plasmon (BDP) and bonding hybridised quadrupolar plasmon (BQP) the corresponding CTP modes are typically labelled as the CTP and CTP'. The CTP' is often labelled as the screened bonding dipolar plasmon (SBDP) due to the similarities in the charge distributions between a second order CTP and first order bonding mode.

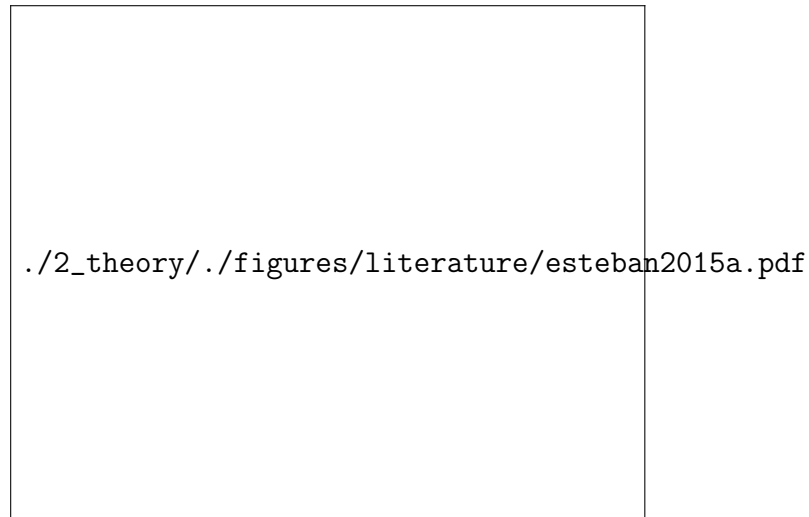


Figure 2.12: Calculated plasmon energies of a spherical AuNP dimer as a function of gap separation using a number of computational models [74]. The classical local approach is valid for separations greater than 2 nm. Below this non-locality smooths the gap and adequately describes mode behaviour until 3 Å. At this point quantum models must be used. Figure taken from [74].

enhancement increases infinitely. This behaviour is completely unphysical and is rectified once non-locality and quantum mechanical effects are considered. A comparison of the models taking these into account is shown in Figure 2.12. Quantum mechanical effects begin to affect plasmon coupling under two conditions - either the particles become sufficiently small that quantum non-locality and non-local effects (finite, non-negligible electron wavefunction spill-out from the particle) become important or the gap size decreases to scales on which quantum tunnelling and non-locality of the gap surfaces can no longer be ignored.

Non-locality, the spill-out of electrons from the surface of the metal, smooths the gap geometry, and consequently the spectral trends. The redshift into contact is heavily reduced compared with classical predictions. Smoothing of the sharp edges in the gap rectifies the continuum of higher order modes, which are then harder to excite, leaving only the most fundamental dimer modes. Redshifts are reduced since electrons move further into the metal on approach, suppressing coupling [74]. The emergence of CTPs and screening of the bonding hybridised modes prior to geometrical contact are predicted only once quantum charge transfer effects are accounted for. The onset of quantum tunnelling means charge is transported across the gap without requiring geometrical contact, neutralising some of the accumulated plasmon charge. Tunnelling is then followed by ballistic charge transport prior to returning to a classical description of plasmonics. These two effects, due to their significance in dimer systems, are considered in more detail.

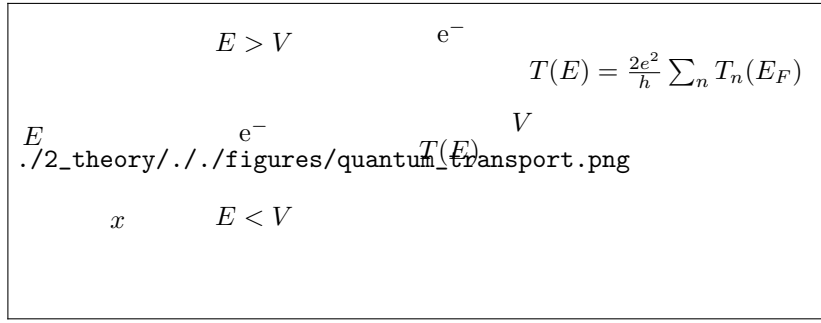


Figure 2.13: Diagram of quantum charge transport between two reservoirs of free electrons. If the Fermi energy of electrons is below the barrier potential (1) then there is a finite transmission probability $T(E_F)$ of tunnelling through the barrier. If the Fermi energy becomes larger than the potential barrier electrons are free to move through a number of quantised conductance channels of conductance $2e^2/h$.

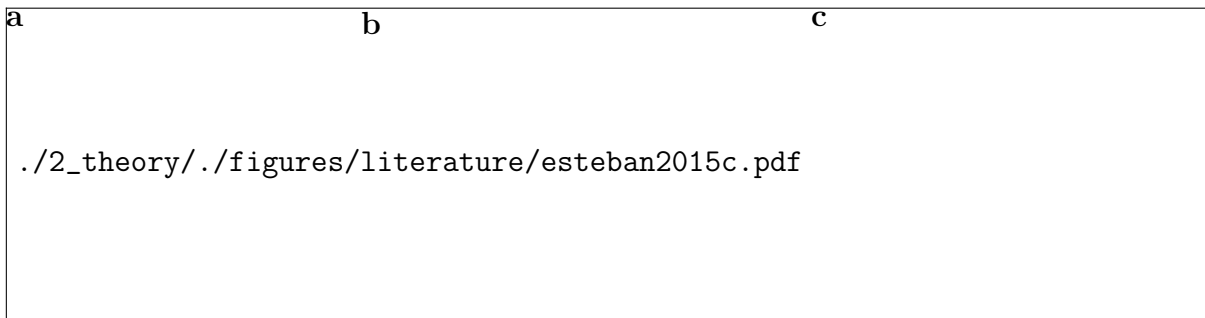


Figure 2.14: Potential barrier shapes for various gap widths and tunnelling transmission probabilities as a function of separation and material [74]. Calculated potential barrier shapes between two Au particles as a function of separation (a) with corresponding transmissions (b). The inclusion of long-range image charge interactions is compared with a simple short-range barrier model. Realistic barrier shapes are more rounded than the simpler rectangular assumption. Overlap between rounded potential edges decreases the barrier height with reduced separation. Tunnelling increases exponentially as the gap width reduces, with increased tunnelling caused by the smaller rounded barriers. Transmission depends on the work function of a material with differing transmission probabilities at a given separation (c).

Quantum Charge Transport: Electron Tunnelling and Ballistic Transport

The quantum charge transport properties of a system consisting of two reservoirs of free electrons separated by a potential barrier are determined by how the height of the potential barrier compares with the Fermi energy of each reservoir. For two metals separated by an insulating gap the potential barrier will be larger than the Fermi level. Classically, electrons with energies below the potential barrier cannot reach the other side. Electrons can only conduct through via quantum tunnelling, in which electrons incident on thin barriers have a finite probability of passing directly through the barrier as opposed to going over it. This is shown in Figure 2.13.

The potential barriers and transmission probabilities of a tunnel junction between two

reservoirs of Au are shown in Figure 2.14. In a simplistic model, the potential layout is considered as a 1D rectangular barrier and the tunnelling probability increases exponentially with decreasing barrier width, going as [75, 76] $T = T_0 e^{-\beta d}$. Many different expressions for tunnelling behaviour exist due to the large number of parameters that influence it (e.g. work function, barrier potential, barrier shape, applied bias, temperature, charge hopping [76]) and the extension of it into 3D gap morphologies, however the exponential decay is always present.²¹ This behaviour holds for large gap sizes but begins to fail in small (2 Å) gaps where the rectangular barrier shape assumption no longer holds (Figure 2.14a,b). The barrier height begins to decrease with separation on overlap of the rounded edges. Tunnelling then becomes even more likely as the separation decreases. Since the transmission depends on the Fermi energy of free electrons in a material and the potential of the barrier region in between, different materials have different tunnelling responses. For example, tunnelling is far stronger in Na than in Au (Figure 2.14c) [74]. Finally, the current generated by tunnelling depends on the number of tunnelling channels currently available in a junction and the transmission coefficient of each channel [77].

Once the barrier falls below the Fermi level (at $\sim 1\text{--}2$ Å), provided that the contact is short enough that motion is ballistic (no scattering), conduction electrons can move freely between the two reservoirs via a number of discretely quantised, 1D conduction channels under the application of an applied bias. The bias in the plasmonics case stems from the field induced by light. Each channel has a transmission probability $T(E_F) = 1$ and a conductance given by $G_0 = 2e^2/h$, the conductance quantum [78]. The total conductance depends only on the number of open channels, a quantity depending typically on the width of the conductive region. This results in a conductance described by the Landauer formula²² [78], where n is the number of transmission channels. Though still firmly in a quantum domain, ballistic transport is a form of conductive contact as opposed to a tunnelling phenomenon. Classical behaviour is only recovered if the length of the constriction increases to the point at which electrons begin to scatter or the width increases to allow many channels. In this event, the conductance is classified as diffusive with a conductance given by $G = \sigma A/d$.

Quantum Charge Transport in Plasmonic Nanogaps

The effects of quantum charge transport were first predicted in small ($R < 2$ nm) NaNPs using full quantum mechanical, time-dependent (TD) density functional theory (DFT) calculations [77]. Since these calculations consider the behaviour of each electron, they are currently limited in complexity to small systems containing less than 2000 electrons. Quantum effects in larger metallic nanostructures are predicted by the quantum corrected model (QCM), a classical

²¹At least within a low bias approximation, which is generally valid in the context of this thesis.

²²Full derivation of the Landauer equation and quantised conductance is found in the appendices.

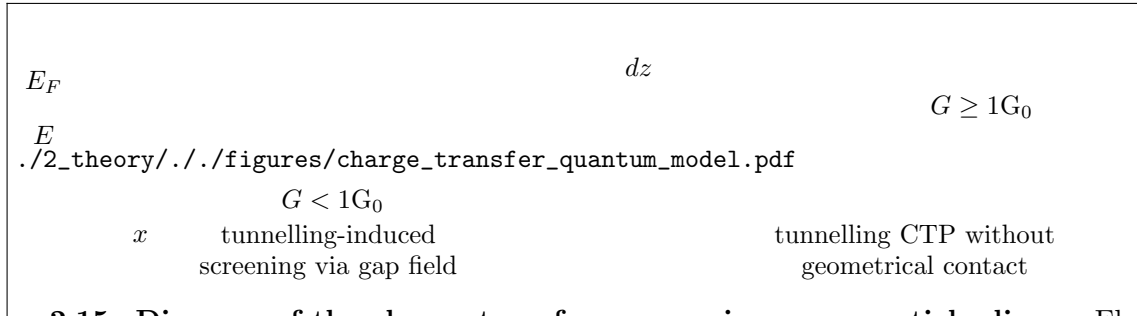


Figure 2.15: Diagram of the charge transfer process in a nanoparticle dimer. Electrons are considered non-local and spill out from the gap surfaces. Long-range image charge interactions also further round the potential barrier. Tunnelling at large distances neutralises optically-driven charge accumulation on gap surfaces, reducing coupling. At smaller separations the particle Fermi level can become greater than the gap potential barrier, permitting conduction instead of tunnelling. This is the origin of gap current and CTP excitation.

model which includes the effects of non-locality and uses an effective gap dielectric function that takes into account the conductivity induced by quantum effects using pre-calculated values from TDDFT [69]. Both the QCM and TDDFT show agreement on the effects of tunnelling and conduction on plasmon coupling in NaNPs, with QCM predictions of the plasmon energies in a AuNP dimer shown in Figure 2.12. Experimentally, evidence of quantum transport effects in plasmonic gaps has recently been found using optical spectroscopy [14, 79, 80], EELS [81], SERS [80], photoluminescence [82] and third-harmonic generation measurements [83].

In numerical simulations, the onset of tunnelling creates a conductive bridge through which electrons can transmit during each half optical cycle. Charge transfer across the junction neutralises some of the plasmon charge on gap surfaces, locally preventing charge accumulation and lessening the local capacitive interaction. Tunnelling increasingly screens coupling leading to a reduction in the rate of redshift. The appearance of this additional contribution to coupling signifies entry into the *crossover* regime [77]. At these separations, typically 5 Å in Na, the barrier remains above the Fermi level. The most prominent effect of screening is a drastic decrease of the field enhancement in the gap as bonding hybridised modes are gradually expelled from the gap [69, 77]. In theory, this prevents small gaps from being useful as SERS structures, motivating the need to fully understand such effects.

The conductance of gap sizes characteristic of tunnelling is too small to excite CTPs, hence only screening is initially observed. Once the gap size reduces to the point at which the barrier falls below the Fermi level a dimer transitions into a conductive state where $T(E_F) = 1$ and conductances are given by Eq. ???. This is the *conductive* or *CTP* regime. A diagram showing the changeover in conduction mechanisms is shown in Figure 2.15, similar to the DFT calculations presented in [77]. In recent quantum simulations this critical gap width is found between 1–2 Å. A similar drop in barrier heights below the work function of Au is found in Figure 2.14a between 2.65 Å and 1.06 Å. The free flow of electrons permits a large amount of current through the junction and enables CTP excitation [77]. The current

immediately increases screening so much that bonding hybridised plasmons decouple and undergo a blueshifting transformation into CTPs. In initial quantum calculations [77] the fundamental CTP is not shown but is found in later TDDFT calculations appearing near to geometrical contact once the conductance rises sufficiently [69, 81].

Though initial simulations considered only small NaNPs it is proposed that in larger nanoparticle dimers the boundary to the quantum regime would be extended to larger separations as larger nanoparticles have more closely spaced energy levels (reduced quantum size effects) and therefore more available conductance channels [77]. In essence, this means that the conductance required to cause these effects remains the same but is achieved through the cumulative contribution of many individual conduction channels. The QCM seemingly reproduces this effect with CTP excitation and blueshifts occurring in $R = 25$ nm Au particles at around the same 2–3 Å separation as in $R = 2.17$ nm Na particles, despite the lower rate of tunnelling between Au surfaces. This indicates that a larger surface generates the same tunnelling conductance as a smaller, more conducting junction, which is enough to produce the same amount of charge transfer in time.

A simple estimation of this critical distance is given in [14]. The conductive regime is said to dominate once the charge stored in a plasmon becomes less than the charge involved in charge transfer, i.e. the fraction of conductive charge is greater than 50%. The tunnelling conductivity in a rectangular barrier model is, where $k_e = \sqrt{2m\varphi}/\hbar$ is the electron wavenumber at the work function, φ . The distance at which this leads to a majority of charge transfer is calculated as, where λ is the wavelength of the plasmon and $\alpha = 1/137$, the fine structure constant. Evaluating this for Au ($\varphi = 4.8$ eV) at an 850 nm plasmon wavelength yields a critical separation of 1.6 Å. If instead the larger conductivity from DFT is used, the equation predicts a critical gap size of 3.1 Å, the same value as is shown in QCM spectra. This is the point at which plasmons change from being majority capacitively coupled to majority conductively coupled.

Preliminary experimental measurements of the optical scattering from a dynamic spherically-tipped Au AFM probe dimer clearly show the aforementioned effects. Two coupled plasmon resonances, denoted A and B, begin to weaken during the final 7 Å of the approach into contact (Figure 2.16a) [14]. Distances are determined by comparing with QCM spectra. Modes A and B blueshift upon decreasing past a critical separation of 3 Å and begin to regain intensity. A mode, C, strengthens going into contact. These are the signatures of bonding hybridised modes transforming into CTP modes as field is expelled from the gap and conductive channels bridge the gap. Agreement between experimental and theoretical spectra also reaffirms the assumption that the smooth changeover between capacitive and conductive plasmons occurs once charge is split equally between them.

Though experimental tip dimer spectra and QCM spectra have some discrepancies due to

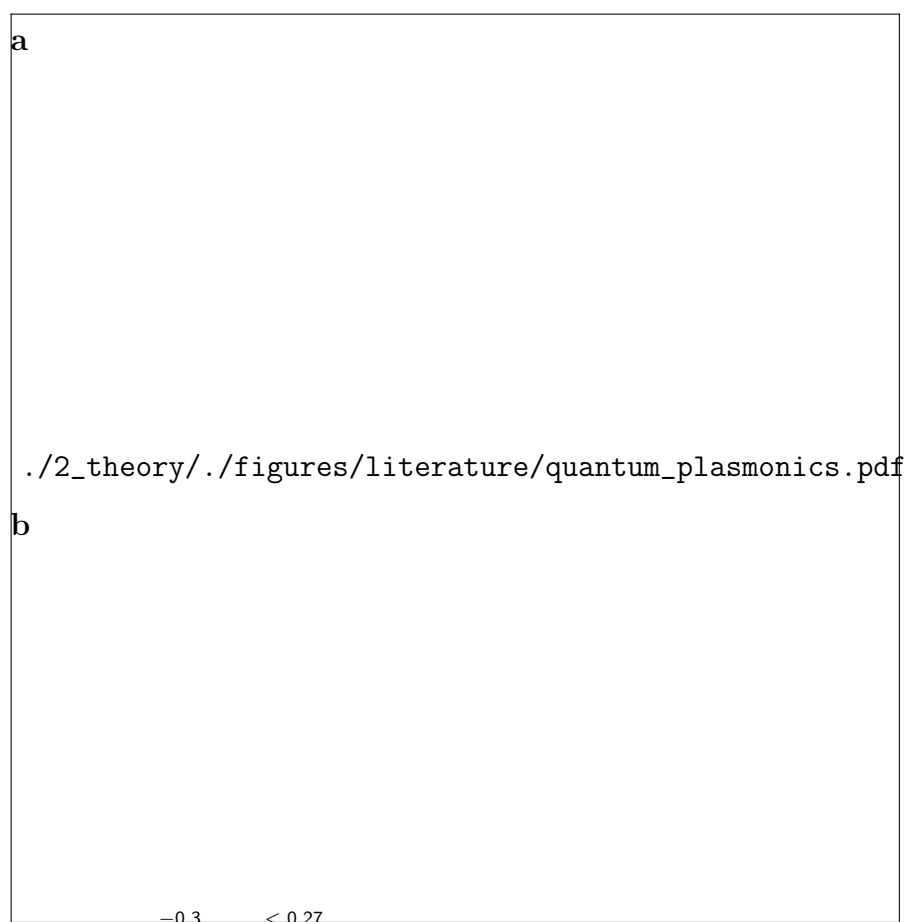


Figure 2.16: Examples of experimental measurements of the effect of quantum tunnelling on plasmonic gap systems through direct monitoring of the plasmon resonances.

(a) Supercontinuum dark-field scattering measurements of two 300 nm diameter spherical Au tips in a dimer configuration with reducing separation, transitioning below 1 nm and into the quantum regime [14]. (b) EELS measurements of 10 nm AgNPs being induced closer together by the electron beam [81].

the difficulty in simulating such large tip structures, they qualitatively agree. Further agreement with DFT calculations is found in EELS measurements on 10 nm AgNP dimers, brought together under the influence of the electron beam (Figure 2.16b) [81]. In this system the dimer exhibits screening at 5 Å and the blueshifting transformation between bonding modes and CTPs begins at 3 Å along with the excitation of the fundamental CTP. The agreement between both experiments, the QCM and DFT calculations reinforces the idea that quantum tunnelling screens plasmon coupling and the rising conductance after ballistic conductive contact leads to the rise of CTPs. The observation of a critical distance of 3 Å in many systems of different sizes, shapes and metals is also intriguing and poses further questions of what exactly the conductance is at that point.

A small number of recent experiments have also now begun to report effects attributed to conduction and quantum tunnelling. Alkanedithiol molecules of various lengths have been



Figure 2.17: TDDFT calculations of 16 Å faceted NaNP dimers arranged with different facet alignments [85]. Aligned facets leads to the smallest field enhancement and the earliest onset of charge transfer effects at 5 Å. Vertex alignment results in an atomic-scale lightning rod effect and increased field localisation. CTP excitation is more difficult in this configuration, occurring at 0 Å, due to the small contact but screening is made easier for the same reason, occurring at 7 Å. The figure is taken from [85].

used to discretely tune the gap separation of AuNP dimers, with attenuation and blueshifting of the BDP with molecules smaller than pentanedithiol [79]. Similar results are found when using intercalating surface-assembled monolayers (SAMs) [84]. Further investigations into sub-nm plasmonic gaps have also shown behaviours attributed to quantum tunnelling, though inferred from properties depending on the field enhancement as opposed to direct measurement of SPRs. A decrease in signal intensity in both the SERS peaks [80] and photoluminescence [82] in nano-gap systems, for example, are signatures of quantum tunnelling screening the coupled plasmon field.

A final feature to note about quantum effects is their variability with gap morphology. It has recently been shown that atomic-scale morphology changes can dramatically change the plasmonic response through the sub-nm regime [85]. This is demonstrated by considering 16 Å faceted NaNPs dimers in various configurations, shown in Figure 2.17. With flat surfaces aligned the conductance is maximised with CTP and an abrupt blueshift seen as early as 5 Å. In contrast, with facet vertices aligned a CTP only begins to emerge after contact between atoms. Screening in this arrangement is observed earlier at around 7 Å, likely due to charge

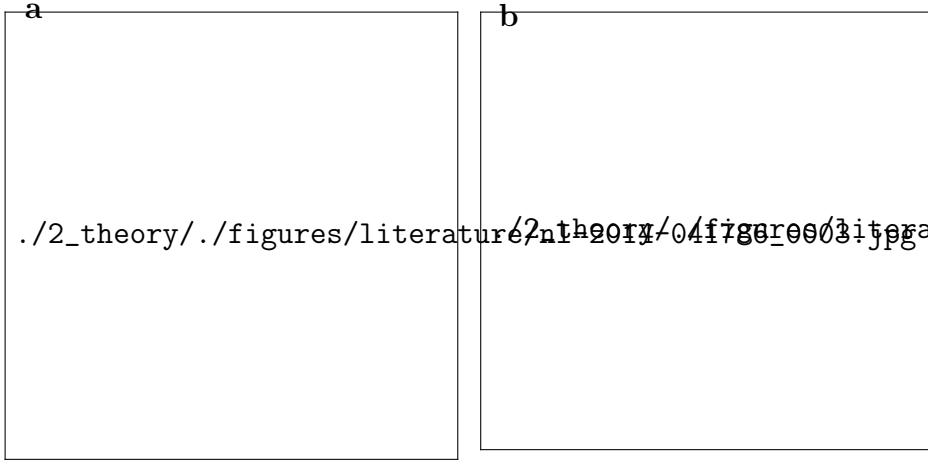


Figure 2.18: Experimental and theoretical scattering spectra of 80 nm AuNP on a planar Au mirror separated via variable conductance molecular spacer layer [86]. Variable conductance molecular SAMs are formed from fractional mixing of BPT (insulating) and BPDT (conductance). The blueshift and attenuation of the coupled plasmon begins at $2G_0$ with the screened mode emerging once $G > 5G_0$.

only having to neutralise a small surface area. The facets demonstrate an atomic lightning rod effect that increases the field in the gap whilst minimising the conductance. All other configurations average to the expected result predicted using a spherical particle model. This demonstrates that experiments can in some sense become limited by surface roughness or even atomistic surface defects.

Limits of Critical Behaviour in Conductive Plasmonic Nanogaps

Both the blueshifting portion of the screening effect and CTP excitation require a conductance threshold to be surpassed in order for these effects to occur. Thresholds have been defined for a dimer containing a classical conductive linker, where the gap between particles of radius R has a width d , conductivity σ and linker radius a [71]. The formation of screened plasmons occurs at low conductances with a critical conductance for the dipolar bonding plasmon given by, The conductance can be reduced to a conductivity threshold by removing a factor of $\pi a^2/d$ yielding, The threshold is intrinsically independent of geometry and depends only on the conductivity. For larger contact widths or shorter linker lengths the threshold increases to overcome the increased capacitive coupling. Experiments maintaining a fixed geometry whilst increasing the gap conductivity using fractional mixing of similar conductive and insulating SAMs have succeeded in showing a blueshift of coupled plasmons with an estimated $2G_0$ threshold [86], as shown in Figure 2.18. A similar $2G_0$ threshold is also found in theoretically considered 1 nm dimer linkers [71].

A second, much larger, threshold exists for CTP formation, occurring at, which can similarly be reduced to a conductivity threshold, Unlike screening, CTP formation depends not only on the conductivity but the junction geometry. The geometry factor (R/a) represents

the ratio between the total charge in the particle and the amount which can pass through a gap with fixed conductivity. Having a large conductivity means the junction does not have to be as wide, relative to the particle size, to accommodate enough current to maintain a CTP. Hence, dimers linked by a highly conductive metallic link can sustain a CTP with only a small nanometric-scale contact area. This has been demonstrated by threading together AuNP dimers fixed with a hollow spacer molecule using high power laser pulses [73, 87].

Interestingly, qualitative agreement between QCM calculations and full quantum mechanical calculations suggest that the quantum nature of the system is of little importance. Even though the QCM uses a classical, resistive gap with conductance values characteristic of quantum transport, quantum effects on gap plasmons are accurately replicated. This implies that, despite the quantum nature of such small gaps, the effects on plasmon coupling only depend on the amount of charge transfer and not the mechanism by which it occurs. This links together work done using particle positioning [14, 81] with studies of interacting plasmonic system coupled with molecular linkers [79, 84, 86]. Quantum tunnelling and non-geometrical conductance still remains an interesting case, however, since both forms of conduction are unavoidable once gap sizes decrease below 0.5 nm. This is why the point at which the electric field is expelled from the gap is described as the quantum limit to plasmon confinement [14]. For this reason, it is important to fully understand the relations between plasmonic hot spots and sites of (quantum) charge transfer.

Although charge transfer effects have been shown in previous reports by varying the conductivity of a fixed gap, there has yet to be a report showing the optical response of a dynamic dimer structure correlated with its electronic response. It is the aim of this project to successfully demonstrate and explain the possible ways in which electrical and plasmonic phenomena are related using a dual plasmonic nano-tip dimer. Metallic nano-tips are a plasmonic geometry currently receiving significant attention from the plasmonics community. In order to use nano-tips to determine the effects of quantum tunnelling on plasmonics, their supported plasmons must first be described.

2.3 Plasmons in Tips

Significant efforts have been made to advance nanoscale surface characterisation by developing new optical tools and integrating optics into existing nanoscale topological measurements. Metallic tips were investigated due to the widespread use of scanning probe microscopies (SPMs), such as AFM, and STM. The similarity in size between metallic nanostructures and the sub-wavelength-size apex of tips initially suggested that visible plasmons would be expected, enabling resonant near-field enhancement. Prior to any spectral characterisation studies to understand their near-field response, tips were applied in combined SPM-optical

microscopes to achieve sub-wavelength localisation and enhancement of optical signals. As the next logical step from SERS and SNOM, the sharp apex of tips were exploited to develop the spin-off techniques of tip-enhanced Raman scattering (TERS) [88–91] and apertureless scanning near-field optical microscopy (a-SNOM)²³ [92–97]. These are also known collectively as tip-enhanced near-field optical microscopy (TENOM).²⁴

The concept for TENOM was first proposed in 1985 [98] but it was not until 2000 that reports first emerged using tips to enhance Raman spectroscopy [88–91]. All measurements were carried out in inverted microscopes with either an AFM [88–90] or STM [91] mounted on top. Two of the initial measurements suggest the overall Raman enhancement has a lower limit of $\sim 10^4$ [88, 89], hence a field enhancement of around 10. A third independent measurement utilising evanescent wave excitation obtained an enhancement factor of 80 from a single tip apex, equivalent to the summed enhancement of many SERS hotspots on a Ag island film [90]. Since then Raman enhancements in the region of 10^7 – 10^9 have been measured [99].²⁵ Whilst SERS enhancement factors have also increased significantly in recent years, the TENOM approach remains popular since the tip can be scanned across a sample. For this reason, techniques such as TERS are widely considered to become the successors of SERS. However, for this to be the case, nanotips require the capability to controllably and reproducibly enhance the near-field. Understanding the electromagnetic response of metallised tips has therefore become of significant importance in recent years. Since the use of tips for observing fundamental plasmonics is also a central part of this project it is beneficial to understand the underlying concepts and mechanisms of TENOM.

TENOM is ideally classified as a local excitation approach as opposed to a local scattering approach [103], though the two are not independent. Figure 2.19 shows the general approaches to TENOM. In the tip scattering approach the non-radiative near-field, comprising evanescent waves, is perturbed by the presence of the tip, leading to scattering into radiative modes. In the tip excitation approach, the tip is resonantly excited to induce a large, local, near-field enhancement and used as a sub-diffraction-limited light source, from which localised scattering can be measured. This process can be much more efficient than the pure scattering approach but depends on the optical antenna properties of the tip. In both cases, the resolution of scattering images is sub-diffraction limited and set by the size of the tip radius (~ 50 nm).

To optimally exploit light scattering from nanoscopic tips, tip-based systems have been generally designed in either the side-illumination and bottom-illumination configuration (photon

²³Also known as scattering scanning near-field optical microscopy (s-SNOM).

²⁴These are also sometimes known as field-enhancing near-field optical microscopy (FENOM) since apertured techniques do not necessarily exploit plasmonic enhancement as much.

²⁵A clear distinction is made between the field enhancement, $|E/E_0|$, and the Raman enhancement, $|E/E_0|^4$, when stating enhancement factors. In the literature the terms “field enhancement” or “enhancement factor” are generally used interchangeably between the magnitude of the near-field and the improvement in the Raman signal.

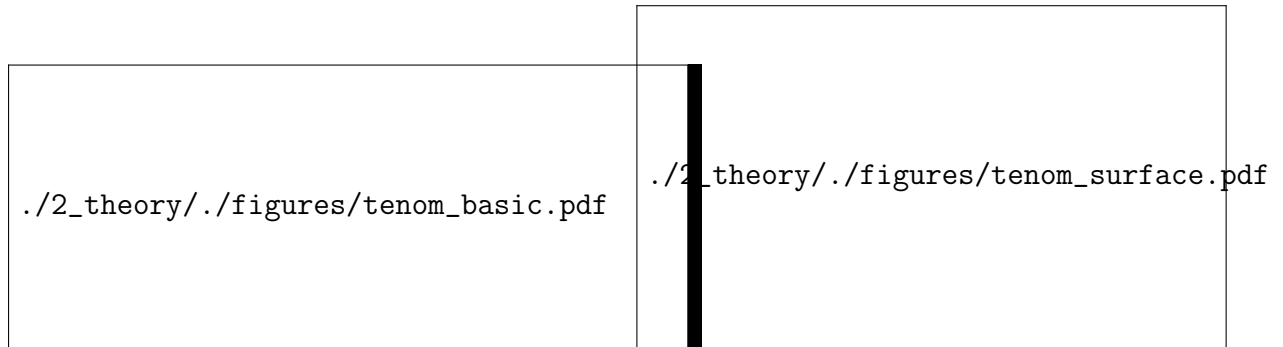


Figure 2.19: Concepts of TENOM. Basic TENOM systems constitute a tip and a sample (left). Tips can perturb evanescent surface waves, generated by high-NA TIR, and scatter them into the far-field ($1 \rightarrow 3$) [100, 101]. Photons illuminating the tip can induce a weak dipole localised to the tip apex, which can scatter the near-field ($2 \rightarrow 3$). More recent TENOM arrangements employ a metallic substrate to couple with the tip and further localise the field into a “hot spot” (right). Coupling of plasmons between the tip and the substrate can be achieved by exciting SPPs on the substrate using evanescent waves (1) or by focusing light on the MIM gap such that the tip dipole induces an image dipole in the substrate (2). Both mechanisms lead to scattering of light from the gap into the far-field (3). SPPs launched onto the planar surface (either via the tip or evanescent waves) can radiatively decay into $NA > 1$ ($1, 2 \rightarrow 4$) [102].

paths shown in Figure 2.19), setting the collection and, more importantly, the tip excitation geometry. Side-illumination has been used successfully in a number of cases [11, 101, 104, 105] but suffers generally from far-field scattering overshadowing the near-field. More complex optical techniques, such as using polarisation-resolved or interferometric approaches, are then required to overcome this. Bottom illumination, the more dominant design, utilises evanescent waves generated by $NA > 1$ illumination undergoing total internal reflection (TIR). TIR results in minimal background scatter outside of the illumination aperture with only the near-field scatter collected. Collection is achieved using either the central $NA < 1$ aperture of the high NA illumination objective [106–111] or a secondary low NA objective [112–114]. Whilst this does require that both the sample and any metallic substrate are optically transmissive, evanescent wave generation can excite SPPs in both a metallic substrate and the tip once brought within the near-field. For these reasons, it is important to consider the optical geometry when interpreting any presented TENOM results.

2.3.1 The Electromagnetic Response of Tips

The electromagnetic response of tips can be broken down into individual components that constitute the enhancement mechanism. The two main optical components are the lightning rod effect and a resonant plasmon contribution for metallic tips [115–117]. Each component is maximised when the incident field is along the tip axis [118]. The plasmonic component has been the focus of study in recent tip-based work, however progress in sharpening tips has also

led to increases in the lightning rod component. Both components are important to consider when attempting to understand optical measurements involving tips.

Regardless of plasmonic behaviour, metallic tips intrinsically exhibit a lightning rod effect under the application of an applied field, instilling a non-resonant component of near-field enhancement. From the definition of the electric field $\mathbf{E}(\mathbf{r}) = -\nabla\varphi(\mathbf{r})$ it is clear that the electric field strongly depends on geometry, with field lines perpendicular to the equipotential conductor surface. The more curved a surface, the more compressed the field lines become around its equipotential surface due to accumulation of surface charge.²⁶ A simple model, calculated by solving Laplace's equation for a tip-shaped electrode, shows this behaviour in Figure 2.20. Consequently, even without a plasmonic component, sharp tips provide a promising platform for localised near-field enhancement.

The expected plasmonic component also arises from the curvature of the metal-dielectric interface at the tip apex. Curvature allows for both SPP excitation and localisation at the apex due to adiabatic nanofocussing [37, 44, 119–122]. This can lead a number of localised plasmon modes in the predicted spectra of tips, however none of these will have an antenna-like geometry to couple well with far-field light. As highlighted when discussing ellipsoidal MNPs, strong, antenna-like LSPs are unlikely to be excited at the apex of a sharp tip since lack of a second metal-dielectric interface prevents accumulation of the opposite surface charge to the apex. Thus, there can be no strong restoring forces or SPRs. The extended size of the typical tip structure ($\sim 20\text{ }\mu\text{m}$) prevents any potential low-order antenna-like plasmons from existing. Calculations for shorter tip geometries (nanococones or nanoellipsoids) show visible-NIR LSPs [123, 124], however these redshift and diminish with increasing tip length, leaving only the smooth response of the lightning rod effect increasing towards the IR [116, 125]. The standard, sharp metallic tip geometry therefore makes for a poor *plasmonic* optical antenna unless the optically-dark SPP modes can be accessed.

Evanescent waves are capable of exciting some of these modes, with evidence for localised

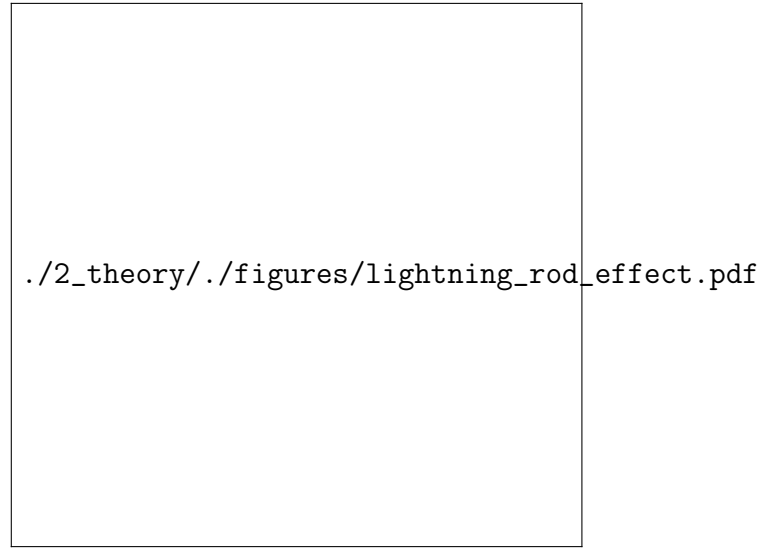


Figure 2.20: Calculated magnitude of the electric field around a tip showing the lightning rod effect. Compression of the field lines around the sharp corner of an equipotential surface leads to a localised, non-resonant field enhancement. Poisson's/Laplace's equation is solved for a tip structured electrode with a surface charge distribution separated by some distance from a planar metal counter electrode of the opposite surface charge.

²⁶Since $E \propto 1/r^2$ the electric field is larger in regions of smaller curvature.

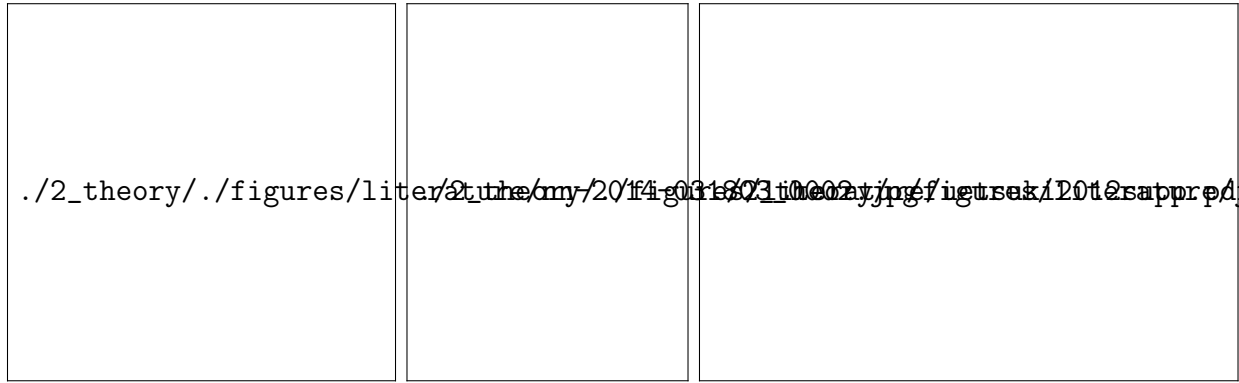


Figure 2.21: SEM images of metallised tips exhibiting random nanostructures. Images are taken from [110] (left), [114] (middle) and [130] (right). Each SEM shows randomised grains deposited using evaporation. These are thought to enable LSP excitation if located at the apex.

apex plasmons found through resonant scattering of evanescent waves [100, 101, 126], resonances in the TERS background [127, 128] and depolarised scattering images [110]. The addition of a degree of nanostructuring also allows for more localised plasmons [106, 110, 129, 130]. Spectral resonances between 600–800 nm have been observed in scattered evanescent waves from the surface of a prism by a Au tip with W giving a comparatively flat spectrum [100]. These are attributed to SPPs. Shifts of ~ 75 –100 nm have been observed between Ag and Au tips with a Si_3N_4 underlying tip material, redshifting resonances by ~ 30 nm compared with solid metallic tips [101, 126]. This dependence on both the tip metal and underlying material has been highlighted numerous times due to the prevalence of the two dominant tip geometries of sharply etched metal tips and metallised (metal-coated) non-metallic tips.

Surface roughness imparted onto metallised tips by the coating procedure is likely to introduce localised plasmonic components which light can couple to, mimicking small 10–50 nm MNPs [110]. Similar behaviour has been used to explain the origin of SERS in rough metal films [1, 2]. Each grain acts as a point at which photons couple and plasmons radiate, hence a grain located at the apex can plasmonically enhance and scatter the near-field. This behaviour is of importance in metallised dielectric tips coated using evaporation²⁷ [106, 110, 130] or chemical reactions [129], some examples of which are shown in Figure 2.21. Even with the frequent application of TENOM, there have been very few spectral measurements of scattering from tips from which to better understand tip plasmonics. Optimum tip parameters, such as coating thickness, for maximum field enhancement are still being debated and characterisation of performance is still carried out using TERS [131].

Complete theoretical understanding of a tip’s electromagnetic response is challenging due to difficulty in modelling tips. Their sub-wavelength apices and large ($\sim 20 \mu\text{m}$) overall conical or pyramidal structure lead to complications when simulating their response, and approaches

²⁷Evaporation conditions used to roughly nanostructure a tip are similar to when depositing metal islands.

attempting to circumvent these limitations often cause physical inaccuracies in the result. Overly simplistic models, such as modelling only the tip apex, usually as a spherical or ellipsoidal MNP, fail to take into account the actual tip geometry, resulting in the existence of unphysical MNP-like modes at the tip apex. Similar multipolar modes are exhibited by truncated tip models with finite lengths less than $1\text{ }\mu\text{m}$ [123, 124], behaving more like nanopyramids [132, 133]. Zhang *et al.* [116] calculate that between lengths of 200 nm and infinity a tip transitions between supporting low order LSPs, then higher order LSPs, followed by only weak SPPs. LSPs are supported only when the entire tip structure is smaller in size than the focus, allowing light to drive in-phase collective oscillations of the conduction electrons. As the tip becomes larger, phase retardation occurs and higher order LSP modes dominate. Once the tip becomes larger than the focus, the case for almost all standard SPM tips, collective oscillations are no longer possible, leaving only weak LSPs concentrated at the apex and SPPs, whose periodic response in the field enhancement disappears with tip lengthening due to increased losses. Furthermore, the single metal-dielectric interface at the apex means that any LSPs similar to those in MNPs have much weaker dipole moments and are therefore much darker [134]. For realistic tip lengths all plasmon modes eventually disappear into a smooth, lightning rod continuum increasing into the IR [116].²⁸ As a result, smooth, sharp tips do not couple well with far-field light.

Coupling with Metallic Substrates

An alternative strategy is to couple tips with a planar metallic substrate and form a plasmonic MIM cavity to better localise light [44, 112, 114, 128, 135–137]. In this instance, a weakly-excited dipole in the tip can induce an image dipole in the metallic surface to form a more strongly-confined coupled mode in the gap. Specifically, pairing a Au tip with a Au substrate greatly enhances the field localisation and strength, more so than when paired with a Pt surface [135] or a non-metallic surface [134]. This is attributed to better optical polarisability of the Au substrate. In these cases the Raman enhancement has been shown to rise to $\sim 10^7$ – 10^9 [114]. Coupling can be achieved by either exciting the tip dipole or through SPP excitation on the underlying metallic substrate [112, 114]. Unlike the coupling between MNP plasmons, theory suggests that the coupling between a Au tip and a Au surface only minimally shifts the gap resonance [134].

One final tip-based plasmon excitation mechanism of interest that has been discussed in recent years is electrical excitation. Similar to the use of EELS in electron microscopy, tunnelling electrons can be used to excite plasmons in an STM geometry. Since tips are typically illuminated with a single wavelength of light it becomes difficult to discern plasmonic

²⁸The apparent sharpness of the apex increases with wavelength as the field becomes larger relative to the apex curvature. Thus the lightning rod effect is greater at longer wavelengths [116].

features hidden in the collected light. Electrical excitation circumvents this limitation as electrons need only to have sufficient energy eV that a portion transferred to the conduction electrons is enough to excite SPs with frequencies $\hbar\omega \leq eV$. Electrical excitation also functions to both remove background light contributions to spectra by removing the illumination source.

Using tunnelling current excitation, light has been observed from both the tip-air-metal substrate gap [127, 128] and the interface between the metal substrate and its underlying dielectric [102]. Broad resonances, which redshift with decreasing tip-sample separation, are found superimposed onto TERS spectra when operating in the STM configuration [127, 128]. These suggest the formation of a MIM gap mode. Light detected from metal-glass interfaces is leakage radiation from SPPs on the metal-air interface. Since light cannot leak from SPPs at the metal-air interface the detected light must be scattering from gap plasmons between the tip apex and the surface. It is thought that 95% of the emission is due to SPP excitation rather than LSP excitation [102].


2.3.2 Challenges associated with Tip Plasmonics

Since the initial measurements of tip enhancements and plasmons, techniques such as TERS and a-SNOM have become widespread. However, they are not currently reliable enough to be considered as a standard technique. Difficulty controlling the tip near-field is both a result of the irreproducibility of the tip geometry and a lack of understanding of the optical processes governing the enhancement, leading to large variations between reported field enhancements and TERS contrasts. A selection of these, reported between 2000 and 2011, are shown in Figure 2.22, showing the variability of TERS. The current challenges with TENOM are therefore improving the reproducibility of the near-field enhancement between tips [110, 111, 138] and achieving a better understanding of the tips themselves [116].

Factors determining the efficiency of TENOM include experimental excitation/collection geometry, tip sharpness, surface metal morphology, material influences and tip/apex orientation. From Figure 2.22 it is clear that sharper STM tips result in larger field enhancements than metallised AFM tips and comparative studies have shown similar trends [107, 139, 140]. Intuition suggests that the lightning rod effect must play a significant role in the near-field enhancement process. Theory showing drastic increases in the lightning rod effect after only small increases in sharpness (20 nm to 10 nm) gives some evidence towards this [116, 131], potentially explaining the varying measured field enhancements over time and between experiments. However, sharpness-induced enhancements can only be improved to a point as recent theory indicates the existence of a quantum limit set by nonlocal effects [141].²⁹ Understanding how to optimise the plasmonic component in tips is therefore a priority.

²⁹Field enhancement saturates as the potential around any finer structural imperfections becomes smoothed due to electron spill-out (non-locality).

Figure 2.22: Comparison of TERS field enhancements and contrasts reported between 2000 and 2011 [99]. STM tips, likely due to their increased sharpness, outperform AFM tips. Ag tips outperform Au tips. Larger enhancements are observed in systems where there is an underlying thin, noble metallic film. Statistical correlations still remain somewhat weak, showing the current variability in TERS experiments, attributed to irreproducibility of enhancing tips.



./2_theory/./figures/literature/pc630379_f8.jpg

Materials choice, as with much of plasmonics, heavily influences any plasmonic behaviour. Ag tips generally outperform Au tips under visible light, although these claims highly depend on the underlying tip material and metal morphology. Only the metal and its morphology are important in solid STM tips and thickly metallised AFM tips, where plasmon energies are insensitive to any potential underlying materials. On thinly coated (< 40 nm) AFM tips, plasmons are tuned by the metal film thickness [125] and the refractive index of the underlying tip material. Tuning can vary drastically between materials such as Si, SiO₂, and Si₃N₄ [113, 140]. These high index materials can shift SPRs into the infrared and out of resonance with the pump laser frequency. Careful consideration must therefore be given when pairing a tip with a laser [107, 108, 130, 142].

A large amount of variability stems from surface metal morphology. Reliance on randomised apex geometries, as shown in Figure 2.21, for LSP excitation greatly limits reproducibility. Furthermore, this granularity is rarely taken into theoretical account when attempting to mechanistically explain TENOM. The orientation of the tip, along with the roughened apex, with respect to the sample and the incident excitation field is also known to influence near-field enhancement [107, 110].

Finally, variability between similar measurements can stem simply from differences in tip placement, optical setup, whether coupled with a mirror, and the specific illumination/collection geometry or optics used. As tips are rarely characterised there is little traceability between measurements from which to systematically determine the relevant causes for difference. It is highly likely, however, that geometrical limitations are the current dominating limitation restricting the progress of TENOM, leading to research into new tip geometries with better optimised, well-known optical responses.

2.3.3 Tip Modification, Nanostructuring and Optical Antenna Tips

The mode mismatch caused by the size difference between diffraction-limited light and the nanometre scale results in a 3–4 order of magnitude coupling efficiency loss [121]. As described previously, a SP acts as an optical antenna. A good optical antenna has the ability to effectively modify the density of electromagnetic states such that the far-field radiation impedance is efficiently matched with the impedance of a near-field evanescent mode and vice versa [9, 103]. The antenna opens up scattering pathways between near-field emitters and the far-field by connecting wave states (k -vectors) via new intermediate states (the plasmon). Evidence suggests that sharp metallic tips, in their standard form, are not particularly good optical antennae, with most modes unresponsive to far-field light. To improve their coupling efficiency, standard sharp tips have been modified or nanostructured to introduce the necessary intermediary plasmon states [143]. Whilst previously achieved by roughening the metal surface, more reliable and reproducible methods have been developed in recent years to controllably

nanostructure the tip and engineer the optical response.

Gratings imprinted onto the side of tips can transform the apex into a nanoscale, single wavelength light source as SPPs excited on the grating propagate to the apex and re-radiate on 10 nm length scales [144].³⁰ Far-field illumination remains spatially separated from the apex, suppressing background scatter and allowing only near-field scattering from the apex to be measured, producing background-free TERS signals [37, 121]. Nanostructuring of the tip apex has been investigated in order to engineer and tune an optical antenna precisely at the apex. Tips are structured with distinct, sub-wavelength-sized metallic features in order to create the necessary antenna-like LSPs to enable far-field excitation in the visible region of the EM spectrum. Etching [145, 146], focussed ion beam (FIB) machining [147–149], selective deposition [150], MNP pickup [151], and nanostructure grafting [152] have all been successfully used to nanostructure optical antenna tips. Scattering resonances in the visible-NIR spectrum have been directly measured on a subset of these [149, 150] while other reports use improvements in the field enhancement as a measurement of antenna quality [146, 152, 153]. In such cases the field enhancement can be improved by an order of magnitude through LSP excitation [147, 148, 153].

Lack of a strong plasmonic contribution from sharp Au metallised tips to TENOM is further evident from direct comparison with Au nanotip probes. A Si tip with the apex replaced by a Au nanocone outperforms a standard Au AFM tip by 120% in the side illumination geometry [152]. Similarly, cutting the Au coating off past the apex also enables LSPs [150]. Each of these modifications is carried out using FIB machining and is therefore highly controllable, though costly in time and resources.

The simplest geometry to impart onto a tip apex is a sub-wavelength metal sphere. By doing so the tip gains LSPs similar to those in an isolated spherical MNP. The specific SPRs depend on the sphere material and geometry along with the attachment method since the base tip structure determines the local adjacent dielectric medium. Coupled SPRs between two spherical Au tips have been previously observed in the far-field [14], but no characterisation has yet been done. Additionally, a 20 \times increase in field enhancement and spatial resolution has been measured when using a photochemically-fabricated AgNP-on-Si tip compared with a sharp Ag tip [153]. These demonstrate that spherical metallic tips have the potential to improve TENOM if they can be fully understood.

To date there are very few reported methods of simply nanostructuring a tip without the need for FIB, electron microscopy or complex chemistry. A significant portion of the allocated project time was dedicated to determining a simple approach for chemically producing plasmonic tips, specifically targeting the spherical tip apex geometry. Other than their successful application in TERS and fundamental plasmonics studies, the origin of SPRs in spherical

³⁰Single wavelength operation results from adiabatic nanofocussing of only a single $\lambda = 800$ nm mode.

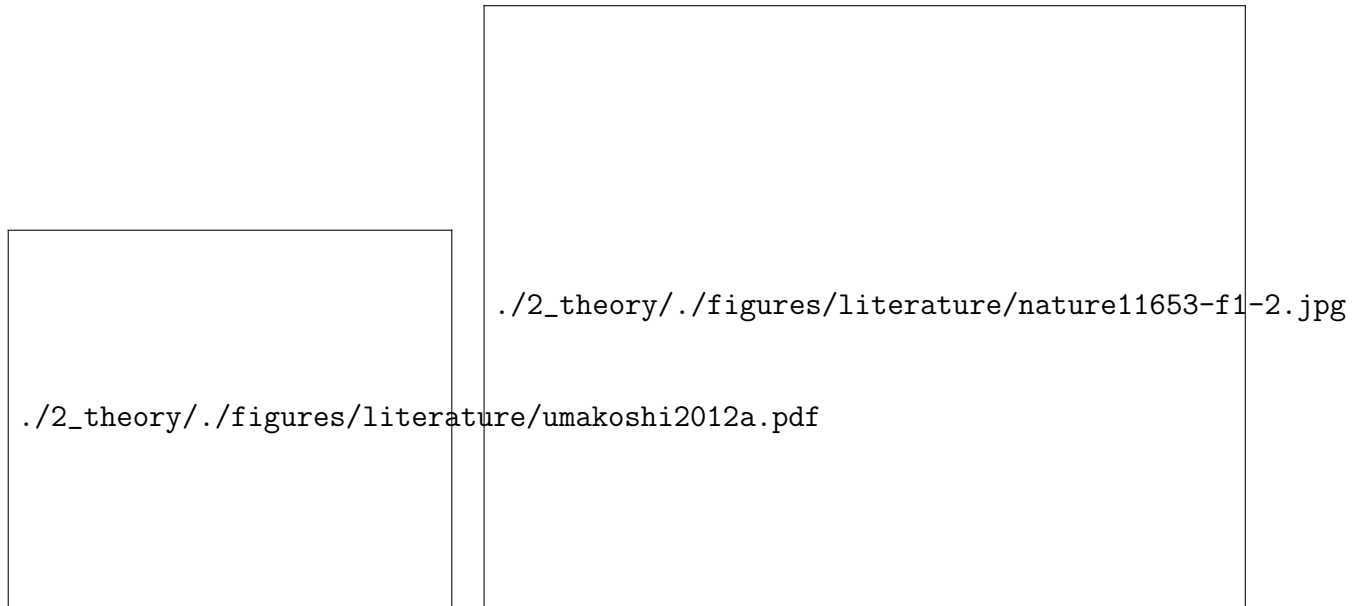


Figure 2.23: Examples of spherical tip fabrication and surface plasmon resonances. (left) Photochemically fabricated AgNP-on-Si tips for TERS [153]. Field enhancement is increased $\sim 20\times$ compared with sharp Ag tips when using 488 nm illumination with a 1.4 NA objective in an inverted microscope. (right) Experimental evidence of LSPs in 50 nm Au-coated, 150 nm radius spherical AFM probes (NanoTools B150) [14]. The large radius minimises sensitivity to axial tip-tip alignment, increases scattered signal levels, and supports higher-order plasmonic cavity modes in the visible spectrum. Resonances are far-field excited using a supercontinuum laser source in a side-illumination configuration. Separation-dependent coupling between two spherical tips confirms plasmonic behaviour.

tips has not yet been fully investigated. Very little work has been done to reliably produce, characterise and understand the optics of spherically nanostructured tips. Furthermore, there is still work needed to similarly investigate the optical response of sharp tips, comparing them directly and quantitatively with nanostructured tips. Both types of tips can then be compared in both fundamental studies and near-field enhancement applications.

2.4 Conclusions

The coupling of plasmons in metallic nanostructures is now widely exploited in order to enhance and confine optical fields on nanometric scales. In order to maximise enhancement, the characteristic scales of these gap structures is rapidly approaching the sub-nm level where quantum mechanics can no longer be ignored. As recent results have shown, charge transfer in such small gaps can lead to the emergence of new plasmonic phenomena and a break down of classical field confinement. This regime must therefore be well understood if the characteristic length scales of plasmonic devices are to continue decreasing.

The effects of electron tunnelling in sub-nm plasmonic gaps have only been touched upon

in recent years and still requires significant investigation. To this extent, tips whose plasmons readily couple with light provide a useful platform for dynamically studying the fundamental plasmonics of nano-gaps. Their well-developed experimental geometries for topological measurements form the basis of microscopes integrating optics and tip-based surface techniques. By using such a setup, tunnelling plasmonics can be further investigated by controllably reducing a gap into the sub-nm regime.

To date there have been no direct correlated measurements between plasmon resonances and quantum transport effects. Tunnelling has been inferred from direct measurements of plasmon resonances without electronic measurements [14, 81] and from variables influenced by the gap field enhancement, which in some cases provide electronic measurements [79, 80, 83, 84]. The effects of quantum charge transport, specifically the relations between screening and CTP excitation, can be better understood with correlated electrical and force measurements. By using an experimental geometry related to AFM these measurements become possible.

Chapter 3

Electrochemical Fabrication of Spherical AuNP-Tipped AFM Probes

As discussed in the previous chapter, nanostructuring a tip can create the necessary geometry and electromagnetic interfaces to support antenna-like plasmons. This enables coupling with far-field light and can improve the plasmonic performance of such tips. Consequently, this also means that excited plasmons scatter into the far-field and are therefore experimentally observable. This is a crucial property when using tips to measure fundamental plasmonics. Because of this, one of the major aims of this project is to produce robust nanostructured, plasmonic tips. The spherical geometry is targeted for its simplicity.

Fabrication of spherical tips has previously been achieved by mounting single nanoparticles onto the apices of tips. This concept has been reported numerous times over the last decade [154], beginning with the use of fibres as mounting structures [155–158] and progressing onto the use of SPM tips [130, 153, 159–161]. Whilst mounting nanoparticles onto SPM tips is more difficult than with fibres the additional capabilities of the SPM tip have made such tips desirable. However, these tips typically require complicated assembly processes to precisely secure a single NP at the apex of the tip, greatly increasing their fabrication time and costs. More recent methods have attempted to address the complexity issue by directly depositing nanoparticles onto the apex by exploiting localised chemical reactions. Nevertheless, these techniques have still been limited by cost or required specialist equipment [157, 160], incompatible with SPM probes [146, 156] or subject to limitations in nanoparticle growth, either in size [162] or material [153]. Non-metallic spherical tips on AFM probes have been created using methods such as vacuum-processing diamond-like carbon growth (NanoTools B-series). These nanotips can then be made plasmonic through evaporation of a metallic coating. Even in recent years it still remains a challenge to simply and efficiently produce spherically nanostructured tips.

Electrochemical deposition is highly suited to the tip geometry because of the large field enhancement localised at the sharp apex point. Due to its significantly reduced radius of

curvature, the equipotential surface resulting from an applied voltage leads to the compression of field lines at the tip apex. This strongly increases the field amplitude in the vicinity of the tip apex and is known as the lightning rod effect. Under such conditions the rate of electrochemical reactions is significantly increased around the tip apex. By exploiting this localised field enhancement it is possible to grow a spherical MNP directly onto the tip apex. Whilst use of the lightning rod effect for electrochemical growth has been used to grow dense forests of MNPs [163, 164] it has yet to be applied to the fabrication of single MNPs at a tip's apex.

Selective growth of MNPs onto the apices tips is difficult using traditional methods of electrochemical deposition but can instead be achieved by using single-pulse, high-field electrochemical growth. This chapter describes the process of pulsed electrodeposition for apex-selective nucleation and growth of AuNP AFM tips. The process of electrochemistry is first described followed by discussion of the method by which spherical AuNP-tipped AFM probes are produced.

3.1 Electrochemical Deposition

Electrochemistry is defined as the study and application of chemical reactions occurring on the surface of an electrode that are either caused by or generate an electrical current. Electrochemical growth, or electrodeposition, is a method of which for depositing a solid material from solution. In general, this requires two electrically connected electrodes, submerged in an ionic solution (electrolyte), with a potential difference. Depending on the electrode potential, and how it compares with the energy required to activate a specific chemical reaction between ionic species, ions are either removed or created at the electrode-electrolyte interface through the addition or removal of electrons, respectively. Electrically connecting electrodes allows excess electrons donated at the anode to transfer and fill the electron deficit at the cathode. An electrochemical cell reaction is therefore split into two half-reactions - electron capture and electron generation. These reactions are known as *oxidation* and *reduction*, which combine to form an overall *redox* reaction. Oxidation occurs at the anode whilst reduction occurs at the cathode. The current flow between electrodes at a given potential is therefore a measurable representation of the underlying reaction rate with electrode potentials setting the range of possible redox reactions. Thus, electrochemistry is a powerful technique, containing an in-built method of directly monitoring the state of the chemical process.

Each oxidation and reduction reaction has an associated standard potential, E° , characterising the potential required to add or remove an electron from the chemical species. Chemical species with highly negative standard potentials can readily donate electrons and are known as reducing agents. Chemical species with highly positive standard potentials are more likely to be reduced and are therefore known as oxidising agents. In general, having $E^\circ < 0$ means

the chemical species is highly likely to dissociate into ions, while $E^\circ > 0$ means a chemical species is more likely to be found in a charge neutral or lesser charged state. Electrons move to equilibrate an in-built potential set by the difference between standard potentials at each electrode, $V_{\text{cell}} = E_{\text{ox}}^\circ - E_{\text{red}}^\circ$, and the resulting current can be used to power an external load.¹ This is the origin of the battery effect.

Electrodeposition is an opposite effect caused by either applying a voltage across a cell containing metal ions (standard electrodeposition) or by using a reducing agent (electroless deposition) [165]. If both redox half-potentials are overcome a redox reaction is activated. Metal ions from the solution are reduced onto the cathode surface, via a half-reaction, The redox reaction is expected to be satisfied by oxidation of the SO_3^{2-} species, however complementary water splitting reactions are also expected at higher potentials. Two sets of half-reactions for the water splitting are [166], and, both resulting in a redox reaction of $2\text{H}_2\text{O}(\text{l}) \longrightarrow 2\text{H}_2(\text{g}) + \text{O}_2(\text{g})$. The standard potential of Eq. ?? is $E_{\text{ox}}^\circ = -1.23\text{ V}$ ($E_{\text{red}}^\circ = 1.23\text{ V}$ for Eq. ??). In general, both these reactions occur simultaneously with a build up of H^+ at the anode and a build up of OH^- at the cathode. Using this solution, significant growth occurs once $V < -0.6\text{ V}$, as has been experimentally determined, with an increase in the number of reactions once $V < -1.23\text{ V}$.

3.2 Initial Fabrication of Spherical AuNP-Tipped AFM Probes

Selective nucleation and growth of a single nanoparticle at the apex of an AFM tip requires using pulsed electrodeposition, an incredibly uncommon method. The reason for this is that standard methods are designed to produce an even metallic coating rather than growth at a single point. For tips, growth must initially be completely field dependent, taking advantage of the tip's lightning rod effect, but not over sufficient time that smoothing of the apex curvature takes place, reducing the apex field and diverting growth around the resultant neck. By applying a high potential in a short pulse all metallic surface ions are immediately reduced. Charge transfer in this domain can be considered instantaneous and nucleation readily takes place. Accumulation of surface charge therefore does not occur and thus the double layer never forms. Growth in this regime is limited only by mass transport.

A simple method is used to successfully demonstrate that a spherical AuNP can be electrochemically grown at the apex of a metallic AFM tip. Conductive coatings are required for the electrochemical reaction, therefore Au- and Pt-coated AFM tips are used (BudgetSensors

¹Consider the example of a battery constructed of a Zn cathode and Cu anode in a $\text{Cu}_2\text{O}/\text{Zn}_2\text{O}$ electrolyte connected via a salt bridge. The half-reactions are $\text{Cu}^{2+} + 2\text{e}^- \longrightarrow \text{Cu}$ ($E^\circ = 0.339\text{ V}$) and $\text{Zn} \longrightarrow \text{Zn}^{2+} + 2\text{e}^-$ ($E^\circ = -0.76\text{ V}$) with an overall reaction $\text{Zn} + \text{Cu}^{2+} \longrightarrow \text{Cu} + \text{Zn}^{2+}$. The potential of this reaction is $\phi_{\text{Cu}} - \phi_{\text{Zn}} = 0.339 - -0.76 = 1.099\text{ V}$.

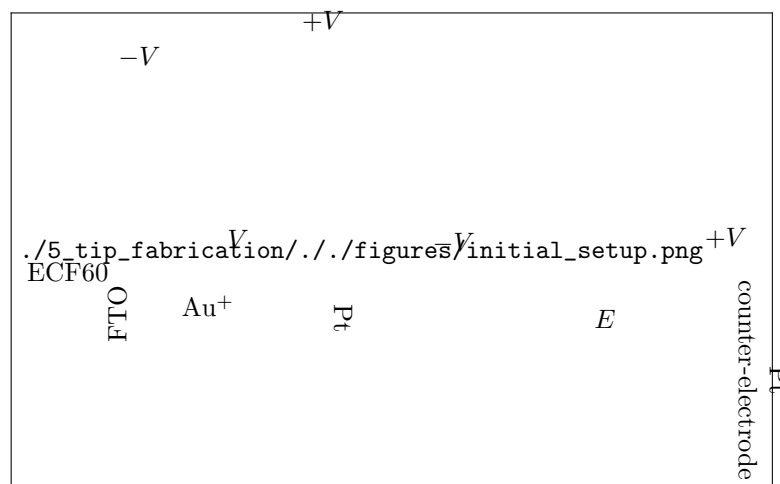
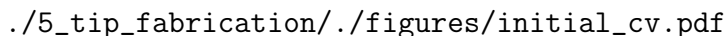


Figure 3.1: Experiment geometry for pulsed electrochemical deposition of Au onto an AFM tip. Electrochemical cell for growth of Au onto the apex of an AFM tip. Termination of field lines at tip apex due to the lightning rod effect enhances localised electrochemical growth for single NP growth.

GB/E series). The adhesion of molecular layers can prevent deposition of Au therefore tips must be cleaned thoroughly prior to deposition. Tips are pre-treated with 20 min O_2 plasma to remove organic contaminants from the surface prior to growth. A simplified two-electrode system (AutoLab PGSTAT 302N potentiostat) is employed for growth since both cell geometry and electrodeposition solution are kept the same between fabrications. AFM probes are attached to fluorine-doped tin oxide (FTO) conductive glass, used as a working electrode, opposite a Pt wire counter-electrode, spaced 10 mm apart (Figure 3.1). FTO glass is cleaned through sonication in 10 min steps using de-ionised (DI) water, ethanol and finally acetone. Metalor ECF60 is used as the electroplating solution with no additives. Simultaneous fabrication of both Au and Pt tips can be carried out by contacting multiple tips, closely spaced side-by-side on the same FTO surface.

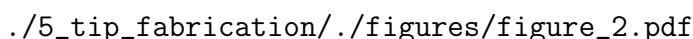
Linear sweep voltammetry of a single AFM tip in ECF60 (Figure 3.2) shows that substantial Au growth starts at around -1 V. This is larger than what is usually expected in ECF60. Differences are attributed to the potentials being referenced to the counter electrode instead of the solution, thus increasing the required potential difference. Further increases in growth are attributed to the activation of water splitting reactions, confirmed by the generation of bubbles at each electrode at higher potentials. An increase from theoretical reduction potentials can also be caused by temperature which factors into the reaction thermodynamics [165]. The current inevitably becomes limited by mass transport causing the observed saturation at highly negative potentials.

A single high-voltage pulse is applied to nucleate and grow a single AuNP at the tip apex. Due to the large field amplitude at the tip apex, field lines from across the cell terminate at the apex, inducing ions to drift towards the tip apex prior to undergoing reduction (Figure 3.1b).



./5_tip_fabrication/./figures/initial_cv.pdf

Figure 3.2: Linear sweep voltammetry of a single AFM cantilever in ECF60. The AFM probe is held by an Al clamp cathode out of solution, replacing the standard FTO electrode to show growth characteristics of only the tip. The remaining geometry is the same as in Figure 3.1.



./5_tip_fabrication/./figures/figure_2.pdf

Figure 3.3: Comparison of AuNP-tipped AFM probes, fabricated on various base structures using -8 V pulses of different lengths. The first three tips were produced simultaneously using a 200 ms pulse on (a) a commercial Pt tip with no pre-treatment, (b) a plasma-treated Pt tip, (c) a plasma-treated Au tip. (d) Duplicate spherical tip produced separately on a plasma treated Pt tip using a 100 ms pulse.

Multiple combinations of applied voltage and pulse times are investigated to optimise growth parameters. Growth of Au onto the AFM tip is confirmed by current dynamics, revealing a 2–3 ms initiation followed by relaxation to continuous diffusion-limited growth within a few 10s of milliseconds. Scanning electron microscopy (SEM) imaging, carried out on a LEO GEMINI 1530VP FEG-SEM Scanning Electron Microscope, is used to characterise the resulting growth morphology.

SEM images of four tip samples fabricated at -8 V are shown in Figure 3.3, three of which were fabricated simultaneously on one FTO glass slide, to show the effects of tip pre-treatment and exposure time in the applied field. These images demonstrate that spherical AuNP tips can be reliably fabricated using the proposed electrodeposition procedure. AuNP growth diameters between 150–450 nm are achieved using 100–200 ms pulses across the electrochemical cell on both Pt and Au tips. Evidence of growth localisation to the high field regions is

clearly exhibited by the formation of spherical AuNPs at the tip apex. The morphologies obtained differ with and without plasma pre-treatment. Using tips as supplied leads to a smooth sphere at the tip apex, resulting from the lightning rod effect, followed by a broad neck and semi-uniform Au coating across the exposed surfaces of the tip (Figure 3.3a). Plasma treatment removes organic contamination and can also oxidise the surface [167, 168]. Removal of contaminants prevents growth at defect sites. The formation of an insulating metal oxide layer prevents growth on surfaces, limiting growth only to sharp regions with a small radius of curvature (Figure 3.3b–d). These regions remain conductive and the electric field is large and highly localised. Because Au is more difficult to oxidise than Pt, the shielding effect is different for plasma-treated, Au-coated AFM probes, which exhibit significant localised nanoparticle growth on all exposed surfaces (Figure 3.3c). Longer pulse times result in bigger diameters of spherical AuNP, as shown in Figure 3.3b and Figure 3.3d. A 200 ms pulse leads to a spherical AuNP on the Pt tip with a diameter of ~ 450 nm (Figure 3.3b), while the diameter of the AuNP is 150 nm with a 100 ms pulse (Figure 3.3d).

3.2.1 Dependence of Tip Morphology on Voltage and Underlying Nucleation Mechanisms

To investigate the dependence of fabricated tip morphology on the pulsed voltage across the electrochemical cell, the growth of AuNP on Pt tips at different applied voltages is further studied. SEM images of such fabrications along with corresponding current transients are shown in Figure 3.4. Images show that apex-selected growth occurs only once the voltage is more negative than -3 V. This voltage dependence is attributed to changes in deposition mechanism with field strength. At low voltages ($V \geq -2$ V), electrodeposition forms smooth film coatings (Figure 3.4b) similar to direct-current electrodeposition. Under these conditions growth is dominant over nucleation and the field profile caused by the lightning rod effect is eventually evened out, yielding smooth rounded tips. Even with 500 ms exposure time no apex-selective growth is observed despite the charge transfer being equivalent to AuNP tip growths at more negative potentials.

The electrodeposition morphologies on tips fabricated at potentials more negative than -2 V can be understood to a certain degree by considering it as the boundary for nucleation. Additional insight can be provided by further considering the most common nucleation mechanisms known from AuNP growth on planar electrodes [169]. These are progressive and instantaneous nucleation. During progressive nucleation, nuclei form at a time t then grow, increasing the size of the diffusion zone around them, thereby preventing further nucleation within that zone. At the end of progressive nucleation there are many nuclei of different sizes due to the different times at which they each originally nucleated. During instantaneous nucleation all nuclei are formed at $t = t_0$ and then grow at the same rate until their diffusion

./5_tip_fabrication/./figures/tip_voltage_dependence.pdf

./5_tip_fabrication/./figures/current_transients.pdf

Figure 3.4: Voltage dependence of pulsed electrodeposition onto Pt tips. Comparison between a standard Pt AFM tip (a) and AuNP growth on plasma-treated Pt tips (b-f) using 150 ms pulses for voltages between -8 and -3 V and a 500 ms pulse at -2 V. This shows the change in deposition mechanism as the magnitude of applied field strength is increased, with no spherical growths above -3 V irrespective of exposure time. (g) Current transients from current traces measured during fabrication of tips shown in (b-f), offset by the saturation current density (-10 , -31 , -34 , -78 , -142 mA cm $^{-2}$, respectively). (h) Variable-independent reduced current transients (coloured lines) measured at various applied voltages during fabrication compared with theoretical curves for progressive (dashed) and instantaneous (solid) nucleation current transients [169].

zones overlap. The overlap of diffusion zones stunts growth as the finite ion flow is split between the two nuclei. For a sparse distribution of nuclei the end result is a set of equally sized particles. For more standard electrodeposition the current transients for progressive and instantaneous nucleation are given in the Scharifker and Hills (SH) model by, and, respectively, where t_{\max} is the time at which the current density maximises at i_{\max} . Usually the transition to instantaneous nucleation occurs after reducing the potential by only 0.2 V from the onset of progressive nucleation potential [170], however this behaviour has not been investigated on short time scales and large, negative potentials where conditions are severely different and the assumptions used to develop the SH model break down.

Increased nucleation is observed at -3 V where spherical tip growth is initiated under a progressive nucleation mechanism. Some preferential growth is exhibited at the tip apex

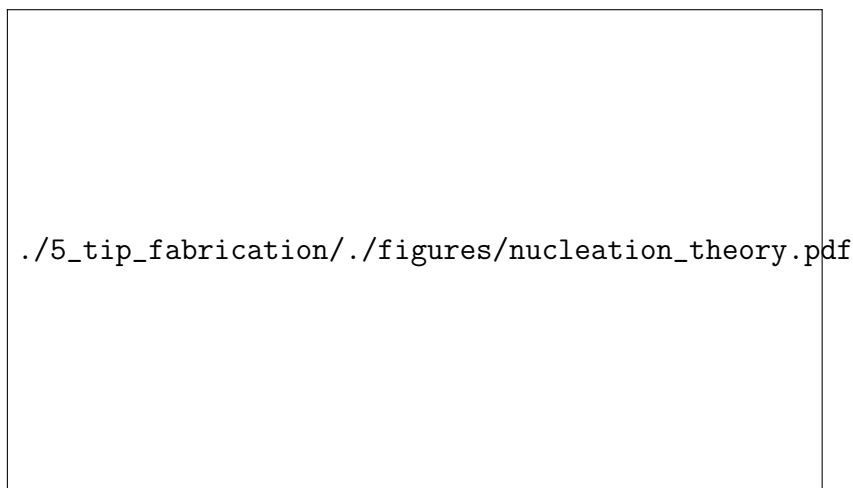


Figure 3.5: Reduced current transients for the two extremes of nucleation [169]. The normalised current, $(i/i_m)^2$, is plotted as a function of time normalised to the maximum, t/t_m . Dashed lines show reduced transients from linear transitions between instantaneous nucleation, assuming instantaneous nucleation occurs first then decreases.

but a strong diffusion boundary has not yet formed, as evidenced by the large number of nucleated particles and variation in particle size (Figure 3.4c). For more negative voltages ($V \leq -4$ V) nucleation becomes more selective, leading to cleaner surfaces and improved apex localisation (Figure 3.4d-f). This is due to a transition to instantaneous nucleation, in which a fixed number of particles nucleate at selected active sites upon application of a field [171]. This occurs preferentially at sharp edges where the field is highest. Further selectivity may occur through depletion of ions in the vicinity of the growing tip, preventing additional growth sites. This helps to produce an isolated AuNP at the tip apex. Increasing the magnitude of the voltage increases the number of active sites available for nucleation and more of the tip surface surpasses the field threshold for instantaneous nucleation. Hence, using less negative voltages while still remaining in an instantaneous nucleation regime minimises the number of active nucleation sites, leading to cleaner spherical growth at the tip apex.

A changeover in nucleation mechanisms is also observed in current transients (Figure 3.4g)² as the shape distinctly changes when decreasing the voltage below -2 V. The largest change in transient shape occurs at -3 V, indicating the onset of shorter time-scale nucleation. Elongation of the transient time is likely caused by contribution to the current from progressive particle nucleation throughout the exposure. Much sharper, short time-scale current transients are observed for potentials more negative than -4 V, supporting the hypothesis of an instantaneous nucleation mechanism as the fast current decay indicates the saturation of all active sites, leaving only diffusion-limited growth.

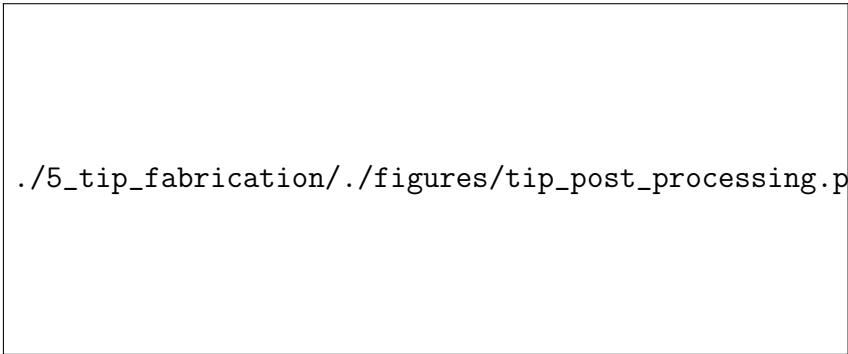
²Current measurements are interpolated to create a smooth line through data points. Transients are analysed by first making a quadratic interpolation of experimental data points before data reduction to extract the reduced current transients. This approach is used due to the limited number of points available in the peak region.

The influence of instantaneous nucleation for isolated AuNP tip growth is further evident in comparisons to theoretical (SH model) reduced current transients for diffusion-limited progressive and instantaneous nucleation (Figure 3.4h). Reduced current transients are normalised to $(i/i_{\max})^2$ and plotted against t/t_{\max} to remove variable dependencies, where i_{\max} and t_{\max} represent the peak current and corresponding time. In general, for less negative deposition potentials (-2 V), nucleation resembles more closely progressive nucleation and growth, while at more negative potentials ($V < -4\text{ V}$) it resembles more closely instantaneous nucleation. This correlates well with the SEM images shown in Figure 3.4d-f. Variations from theory occur due to the variable field profile present across the tip leading to localised instances of both progressive and instantaneous nucleation contributing to the overall current. It should be known that the SH model is built upon assumptions such as random nucleation and provides valid results only for the limiting cases of only progressive or instantaneous nucleation, for which the validity fails in such a selectively grown system [172].

A simple model can be developed from SEM images and current transients. Whilst the large surface area of the FTO glass likely dominates the behaviour of the current density, SEM images do indeed show localised changes in the morphology of the tip. When the apex of the tip has a field profile above the threshold for instantaneous nucleation, a single particle may nucleate at the apex and quickly grow. As it nucleates quicker than the rest of the tip its diffusion zone increases to prevent other particles nucleating nearby. This leads to a clean single AuNP growth at the tip apex. If the threshold for instantaneous nucleation is not met then many smaller particles form around the apex (Figure 3.4c). On the other hand if too much of the tip nucleates instantaneously (very large overpotentials) then the chance for a clean growth is also heavily reduced (Figure 3.4f) since many particles nucleate around the apex prior to the expansion of substantial diffusion zones. The choice of voltage is therefore imperative to ensuring selective growth of a single AuNP at the apex.

3.2.2 Decontamination of Tip Surfaces and Post-Fabrication Processing

After each batch of fabrications, tips are imaged using SEM to study surface morphology. Characterisation is necessary to determine the specific apex morphology but leads to contamination issues. Exposure to the electron beam is known to deposit layers of carbon onto samples. Despite washing tips in DI water and ethanol after deposition to remove any leftover chemical films, the surface of the tip inevitably contains carbon contamination after imaging. To ensure good electrical contact, AuNP tips must be cleaned before use. Although plasma cleaning is used to remove organics from the surface before fabrication it can oxidise the surface. Submerging tips in piranha solution ($3\text{ H}_2\text{SO}_4:1\text{ H}_2\text{O}_2$) for 10 min proves to be an effective method for removing organics from the surface of the Au without introducing



./5_tip_fabrication/./figures/tip_post_processing.pdf

Figure 3.6: Post-processing effects of piranha solution. Low volume and temperature piranha solution removes organics from the Au surface while large volumes at 120 °C smooth the surface.

any adverse surface layers.³ Though it can still oxidise (or hydroxylate) surfaces it is to a lesser extent compared to plasma treatment. Tips treated with piranha solution electrically contacted more often than tips left untreated after SEM imaging.

The activity of piranha solution degrades over time with some indication that small volumes of the solution loses effectiveness after only 15 min. During its initial stages, the piranha reaction is extremely exothermic with temperatures reaching up to 120 °C. The overall temperature of the solution is determined by the volume of solution used. The heat generated in larger volumes takes longer to dissipate, maintaining a higher average solution temperature. The morphology of tips can be somewhat adjusted by exposing tips to piranha solution with varying temperatures and exposure times. Tips cleaned in small (5 ml) volumes show no changes in morphology whereas those treated in a large (100 ml) volumes are found to have smoothed surfaces (Figure 3.6). This effect is attributed to the increased solution temperature enabling surface atom rearrangement into more energetically favourable configurations. No comparison is made with other high-temperature solutions, such as boiling water, since the cleaning of tips is also desired. Should a fabrication fail, or their morphology damaged, Pt tips can be returned to their original state by using Au etching solution (Sigma standard Au etchant) to remove any deposited Au. This effectively reduces the effective cost per successfully nanostructured tip.

3.3 Conclusions

By using electrochemical deposition, the simple fabrication of spherical metallic tips has been successfully demonstrated. Tips can be fabricated within a short period of time and with high throughput using pulsed electrochemical deposition, exploiting the sharp tip geometry

³Piranha solution is a strong oxidising agent and works via H_2SO_4 quickly dehydrating organics. H_2SO_4 and H_2O_2 react to create oxygen radicals which oxidise the remaining carbon molecules into elemental carbon. The overall result is the decomposition of organic matter into carbon, CO_2 and water.

to nucleate and grow a single nanoparticle at the apex. Though simple and cheap compared with many other techniques, control of growth morphology quality still presents issues. The many free variables in the system are problematic for morphology control and are yet to be fully understood and optimised. As a result, there is currently little ability to predict the size and shape of growths. Nevertheless, the deposition process succeeded in its original purpose of providing spherical AuNP tips for plasmonic applications that can be electrically contacted to measure charge transfer through a plasmonic nanogap.

Several advantages emerge from apex-selective single nanoparticle electrochemical growth. The capability for simultaneous nanoparticle growth on many tips ensures a high throughput process, while morphology and size is controlled by voltage and time. This provides a viable method for producing tips capable of expanding the user-base of plasmonics and furthering research into applications of TERS and SNOM. Furthermore, the spherical nanoparticle growth method introduced here is not restricted to specific metals, and many different composite systems can be created with this apex-localised growth technique. For example, silver nanoparticle tips could give a large optical response and field enhancement under visible illumination (although oxidation is sometimes an issue). This technique could therefore become a simple route to effectively improve TENOM across a broadband wavelength range.

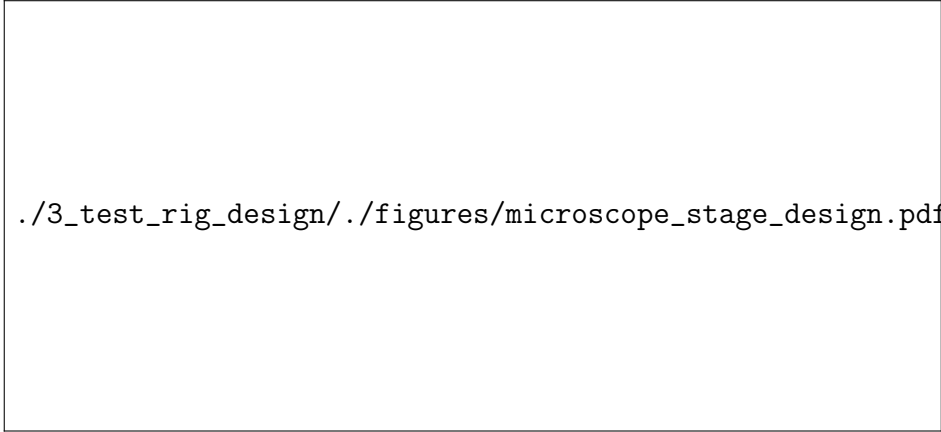
AFM tip experiments are performed in a custom-built microscope for optical spectroscopy with simultaneous force and electronic measurements. The microscope is fully automated¹ and capable of running a variety of experiments, primarily to study the optical response of tips. Its primary function is to take the tips of two opposing AFM probes, align them into a tip-to-tip dimer geometry and demonstrate nm-scale precision spatial control. Using such a setup, the plasmonic behaviour of both individual and coupled tip systems can be investigated. In this chapter the principles behind the operation and design considerations of the microscope system are discussed in depth, with sections split between the mechanical and optical design of the microscope followed by integration of the electronics and AFM module for force measurement.

4.1 Mechanical Design

Measurement of the physical properties of two nanostructures on the sub-nm scale in ambient conditions is a difficult challenge. For a microscope to be able to perform such measurements requires many careful considerations, the result of which is a compact experimental platform resistant to both vibrations and thermal effects.

The most important parts of any microscope are the sample stage and objective lens. For stable optical measurements these have to be locked together and mechanically referenced in a symmetric configuration to prevent mechanical or thermal drift between the sample of interest and the focal spot of the source. The short mechanical reference distance in an inverted microscope design provides the best stability and the microscope platform (Figure 4.1) is designed based on this concept. Mechanical drift is minimised by maintaining a close reference point between the sample and the objective. In this case the sample stage is tightly pocketed into a top plate from which the objective is screwed so that any vibrations between sample and objective occur in phase. Thermal drift is minimised by exploiting symmetry such that

¹A custom Python application used to control the microscope and all experiments



./3_test_rig_design/./figures/microscope_stage_design.pdf

Figure 4.1: Mechanical design of the microscope. The main features of the inverted microscopy platform are highlighted, including two independent nanopositioners, one with piezo control, situated on a removable breadboard plate above the focus of an objective. Breadboard holes enable the mounting of optomechanics close to the sample. The top plate features a sealed lid with gas inlets for environmental control.

any expansion is around the objective and that all mechanical plates expand at the same rate. Cast aluminium is used for plate construction for its lower coefficient of thermal expansion compared to regular aluminium, whilst still remaining cheap and easily machinable compared to steel or titanium. The overall microscope platform is constructed 200 mm above the table on 1.5" diameter steel posts. The 200 mm height maintains stability without the need for cross-linking and is spacious enough to accommodate optics. The microscope platform and all important optics are mounted onto an anti-vibration stage to reduce vibrations. All optics are mounted in either cage or lens tube, held 5 mm off the table and locked together, for stability.

The typical experiment sample setup is shown in Figure 4.2a. Samples are mounted onto either of two 3-axis slip-stick translation stages with 12 mm of travel and fine piezo control (SmarAct GmbH, SLC-1720-S w/ MCS), of which one is mounted onto a 3-axis piezo translation stage (PI GmbH, PI-733.3CD) for finer motion control. The top platform design is modular and easily removable, with a tight-fitting socket precise enough to relocate the sample stage to within 10 μm after removal. Multiple adapters are used to mount different samples onto the stage. A cover slip holder is used for nanoparticle characterisation while AFM chip holders (Figure 4.2b) are designed to mount tips. AFM probe mounts are made from machinable glass-ceramic (MACOR, Corning inc.) in order to prevent thermal expansion (good coefficient of thermal expansion $\alpha_{T,\text{MACOR}} = 9.3 \times 10^{-6} \text{ K}^{-1}$, compared to other machinable materials' $\alpha_{T,\text{aluminium}} = 23.1 \times 10^{-6} \text{ K}^{-1}$, $\alpha_{T,\text{titanium}} = 8.6 \times 10^{-6} \text{ K}^{-1}$ or $\alpha_{T,\text{ABS}} = 30.4 - -73.8 \times 10^{-6} \text{ K}^{-1}$ [166]) and to electrically insulate the mounts from the nanopositioners. The copper clamps holding the AFM probes are contacted to enable biasing of the junction between tips and measurement of the current through the junction.

The grounded experimental chamber is sealed to control the gas environment (switchable

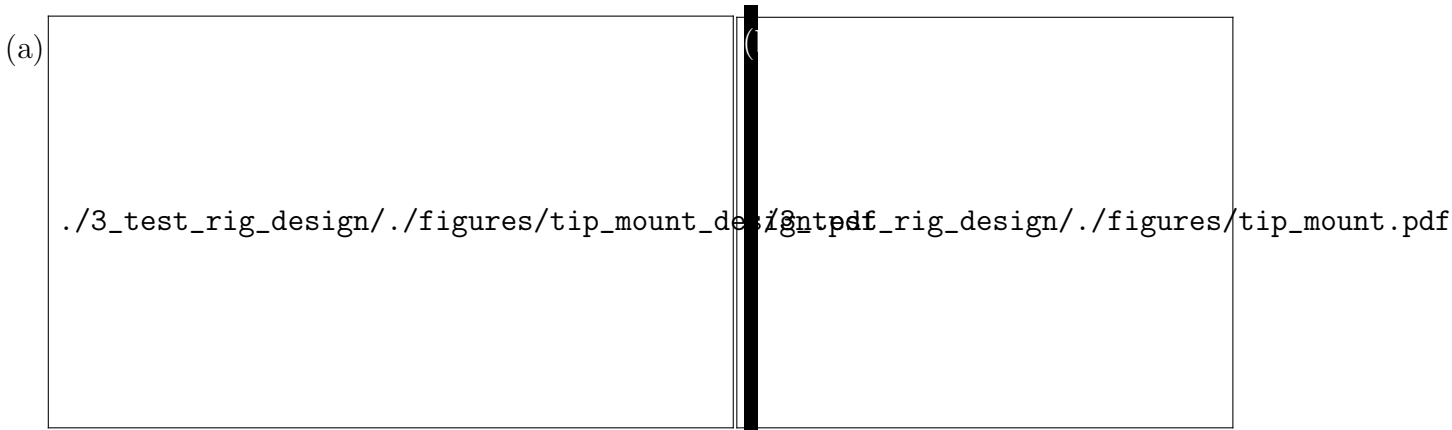


Figure 4.2: Design of the dual tip microscope stage. Images are annotated with the key design features incorporated into the sample stage. (a) Design of the dual tip mount stage and dark-field illumination mechanics. Each nanopositioner with tip mount clamp is connected to an external electronic circuit. A 3D-printed, plastic collar is attached to the objective, holding a 1 mm diameter optical fibre for dark-field side-illumination of tips. A temperature and humidity sensor is attached to the back of the plate for environmental monitoring when the chamber is sealed. (b) Design of the tip mounts. Tips are placed in a rectangular groove in the insulating MACOR plate and held in place by an angled Cu clamp. Electrode solder tags are screwed down onto the clamp to electrically contact the tip. Mirror substrates are stuck onto the bottom of the mount to provide an easily accessible, in-situ spectral referencing point for incident illumination.

between a line containing air bubbled through water and a nitrogen line to control humidity) and act as a faraday cage to reduce electromagnetic interference (EMI) incident on the sample. The chamber is equipped with a low pressure, one-way valve and a needle valve to control the gas flow. Silencers are attached to the gas inlets with a foam surround to prevent air currents. The presence of a sealed chamber is enough to stabilise the sample against external air currents and help maintain a constant thermal equilibrium around the sample. A low magnification basic microscope, constructed from a disassembled webcam CCD, is attached to the roof of the chamber to aid alignment of samples with the objective focus. Metal contacts connect the roof to the grounded base to form the Faraday cage. Optical windows on the sides of the chamber are used to insert secondary lasers perpendicular to the objective axis, used primarily with the AFM module. They also allow for external monitoring of the stage positions from the side.

4.2 Optical Design

Dark-field (DF) spectroscopy is the primary optical method used to study plasmonic nanostructures. The optical design employs the concept of reimaging spatial filters into the correct planes for efficient DF spectroscopy, leading to a compact design. Employing reimaging means that beams are not necessarily required to propagate exactly along the optical axis, minimising the number of long, empty beam lines, typically used for alignment. By reimaging the

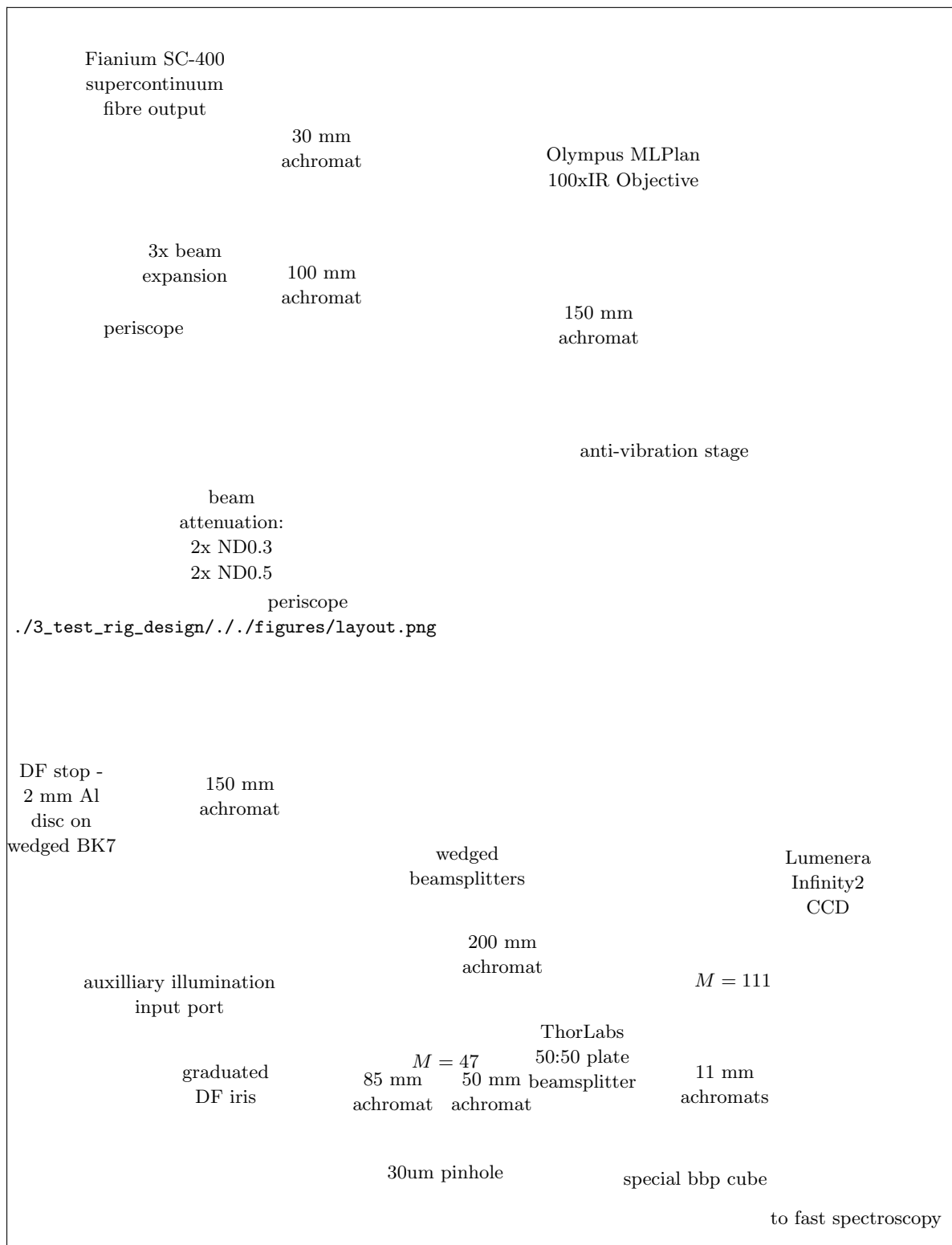


Figure 4.3: Diagram of the full optical layout and specification of the microscope. All optics are accounted for except for silver periscope mirrors, which transfer the beam between platforms of differing height.

front and back focal planes of the objective, spatial and Fourier k -space filters are placed in the corresponding planes, ensuring optimum filtering performance and minimal aberration. A detailed schematic of the microscope platform and the surrounding optical bench layout, containing the specifications of all optics used, is found in Figure 4.3.

Both image and Fourier planes are set through careful placement of each set of lenses. The required minimum degrees of freedom for beam alignment are accounted for by mirrors placed in the focal and Fourier planes. Those in Fourier planes change the position of the beam without affecting its shape, whereas those placed in focal planes only change the beam shape without shifting the position in the objective focus.² The position and shape of the beam are therefore independently adjustable, greatly simplifying beam alignment. This advantageous technique results in a high beam quality, and, as a direct result of the lack of long, iris-containing beam lines, a compact microscope.

A long working distance objective is required for imaging and spectroscopy. A bright-field (BF) long working distance IR objective (Olympus LMPlan 100 \times IR, 0.8 NA) is used to access wavelengths above 700 nm, for which the more convenient DF VIS objectives (Olympus LMPlan 100 \times BD) exhibit a sharp cutoff.³ A DF illumination/collection configuration is necessary for spectrally studying scattered light from a nanostructure. Dark-field refers to the use of high-angle illumination, the reflections of which are filtered to collect only low-angle scattering from the focal plane. A large numerical aperture (NA) is required to properly study nanostructures in DF as it means light is collected across a large acceptance angle with a small focal length and large magnification. Since DF illumination is not supported on BF IR objectives, light needs to be brought in externally in a side-illumination geometry. A 3d-printed objective collar is used to hold a 1 mm diameter optical fibre ~ 1 –2 mm from the sample, outside of the objective collection angle, to which a cold white LED is fibre coupled. The fibre is fed through a breadboard hole in the top plate and sealed so as to preserve the environmental chamber integrity. The fibre outputs a broad cone of light which illuminates samples over a large area.

Use of a ultra-high brightness supercontinuum laser source (Fianium SC-400, 4 W, 480–1750 nm) enables single nanostructure spectroscopy with exposure times around 10–50 ms. The beam is expanded to fill the back aperture of the objective and apertured into a ring to mimic DF illumination using a DF disc stop. The inner diameter of the ring is set at 2 mm and the outer diameter is set by the back aperture of the objective, in this case 4 mm. This technique is a pseudo-DF method denoted supercontinuum dark-field (SDF). Reflective neutral density filters totalling ND 1.6 (2.5% transmission) are placed in the beam line to reduce the incident power on the sample. The majority of the incident power is lost at the DF stop. Further attenuation results from the 10:90 (R:T) beamsplitter used to relay the laser

²Diagrams indicating the principles of beam alignment using reimaging are found in the appendices.

³A comparison of the two available 100 \times objectives is found in the appendices.

into the microscope. At this point the power is reduced to 1 mW, as measured on a bolometer (Coherent, inc.) behind the objective.⁴ This prevents laser damage to samples. Whilst the power is seemingly low and comparable with high-brightness incoherent light sources, the focussing ability of the single mode laser results in an intense, diffraction-limited, white light focus not possible with incoherent sources. For an assumed broadband spot size around 1 μm the focal intensity is $\sim 10^8 \text{ mW cm}^{-2}$.

The incident light is apertured and reimaged directly onto the back focal (Fourier) plane of the objective, as opposed to aperturing close to the objective back aperture. This prevents diffractive artefacts in the conjugate plane of the collected light. The ring aperture means that the focus is illuminated only at high-NA as with conventional DF spectroscopy. Scattered light is then filtered by a DF iris in the return beam path to remove any signal contribution from reflected, high-NA illumination. Reimaging allows both the DF iris and stop to be located away from the objective for convenient access and easy adjustment. Alternative designs using optics mounted at the objective back aperture do not benefit from having the stop and iris in conjugate planes and may require motorised irises if not accessible by hand. For this experiment a simple graduated dark-field iris is sufficient for external use to filter the collected light signal.

Since incident power is not an issue, and in many cases requires significant attenuation, the microscope is optimised for efficient collection. The 10:90 beamsplitter used for laser input means only 10% of collected light is lost when returning back through the main microscope arm. Furthermore, all optics in the system are optimised for light between 500–1100 nm.⁵ The angle-dependent Fresnel coefficients of the glass used in all optics components mean that *p*-polarised light is favoured during transmission throughout the microscope collection path.⁶ A 90° turning periscope is placed after the first reimaging lens to reverse the linear polarisations of light so that the stronger *p*-polarisation component is orientated along the tip axis.

Subsequently, collected light is split into imaging and spectroscopy paths using a second (50:50) beamsplitter placed before the DF iris. CCD imaging is both used to align and characterise the laser focus and to centre samples onto the targeted laser illumination spot. Sample imaging uses light collected from the scattered white side-illumination LED light to produce DF images whereas the laser light is not DF-filtered in this path. Images are magnified 111 \times .⁷ Light passing along the spectroscopy path is DF-filtered to remove any contributions to the scattering signal from reflected light. A graduated iris is used to remove the 2 mm outer-

⁴Power characterisation found in the appendices.

⁵Broadband optimisation is achieved via exclusive use of Ag mirrors, Edmund Optics VIS-NIR AR coating on lenses, COMAR NIR and ThorLabs visible or visible-NIR coated beamsplitters.

⁶All beamsplitters have some degree of polarisation sensitivity due to Fresnel coefficients of the glass used. Reflectance can be a factor of 2 different between orthogonal linear polarisations. For comparison of glass reflectances and Fresnel coefficients see the appendix.

⁷Magnification is calculated by the ratio of focal lengths, $M = f_2/f_1$.

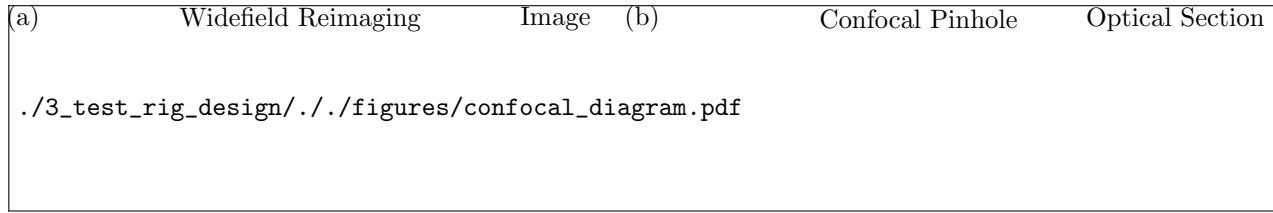



Figure 4.4: Diagram of optical sectioning in confocal microscopy. (a) Out of focus light from nearby reimaged focal planes leads to blur and a decrease of resolution in images. (b) Images spatially filtered in the focal plane by a confocal pinhole localise light from only a select volume that is sufficiently focussed to pass through the pinhole aperture.

ring of the returning beam. The iris is placed in the image plane of the DF stop for the most accurate filtering and optimum performance. The two beamsplitters present before the DF iris are wedged to prevent ghost images, which transmit through the closed iris and create spectral artefacts. However, the 5 mm thickness of wedged beamsplitters means increased dispersion and the limited availability of broadband AR coatings results in reduced reflectance in the NIR. Additionally, the DF-filtering process only works to remove light reflected out at the same angle. Angled samples (such as the facets of tips) can reflect light into the low-NA collection, creating spectral artefacts. It is for this reason that the flat tip facets are even visible in a dark-field configuration.

4.2.1 Confocal Localisation of Spectra

Since the laser focusses to a diffraction-limited spot on the sample, spectra are collected from a small sampling volume. This single mode input forms the first component of confocal localisation. Further spectral localisation is achieved by confocally filtering the image plane after the DF iris using a 25 μm pinhole to collect light from only the central focal spot. Only light in focus on the pinhole may pass through it. By rejecting out of focus light the image becomes an optical section with a tighter depth of focus. The size of the pinhole sets both the lateral and axial width of the transmitted light and leads to both spatial masking and optical sectioning in the objective-sample plane, as shown in Figure 4.4. Spectra are therefore acquired from a localised sampling volume, as set by the location of the 47 \times demagnified pinhole image. The location of this spatial mask image in the objective focus is controlled by a mirror before the confocal filtering array. A slip-in disassembled webcam is used to image the Fourier plane before and after confocal filtering to check pinhole alignment. Since the depth of focus scales as M^2 (or NA^2) the placement of the pinhole along the beam path is not critical. Choice of pinhole diameter, however, is important.

Confocal filtering not only improves image contrast but also improves upon the wide-field, diffraction-limited resolution by up to a factor of $\sqrt{2}$, depending on pinhole diameter, at the cost of image brightness [173–176]. This stems from the removal of higher diffraction orders by



./3_test_rig_design/./figures/confocal_pinhole_choice.pdf

Figure 4.5: Optimum confocal pinhole size across the visible-NIR spectrum. A 25 μm pinhole is chosen for most experiments. Confocal performance is then achieved above 500 nm.

the pinhole. The resolution of a microscope is often quantified using the Rayleigh criterion - the distance from the maximum of the PSF (expected to be an Airy function) to the first minimum [177]. A decrease in the Rayleigh criterion of diffraction-limited resolution is expected in an epi-illumination geometry, going from $r_{\text{lateral}} = 0.61\lambda/NA$ down to $r_{\text{lateral}} = 0.44\lambda/NA$ at best. Decreasing the pinhole diameter therefore not only decreases the optical section thickness but also the minimum resolvable lateral distance to a certain extent.

For a realistic detector aperture the collection point spread function (PSF) is convoluted with its aperture function, D_p , giving an image PSF $I = |h_1|^2(|h_2|^2 * D_p)$ [178]. The resulting resolution depends on a quantity v_p , the detector width, which can be related to the actual pinhole diameter, d_p , through [178], The full-width half-maximum (FWHM) of the PSF retains the full, $\sqrt{2}$ improvement if $v_p \leq 0.5$, but this leads to a significant loss in brightness. An increased resolution is still in effect until $v_p \geq 4$, at which point the wide-field behaviour is recovered. Practically, $v_p \leq 2$ for optimal lateral resolution and $v_p \leq 4$ for optimal depth resolution. Optimising for $v_p = 2$ means that for a 0.7 NA, $M = 47$ system $d_p/\lambda \leq 43$, i.e. 21 μm at 500 nm and 47 μm at 1100 nm. A plot of v_p across the visible-NIR spectrum for a number of pinholes is shown in Figure 4.5, highlighting the relevant confocal regimes. For a given pinhole size that acts confocally in the visible, the intensity of some NIR wavelengths will be reduced since v_p drops below 1, however this loss is acceptable to maintain higher resolution in the visible region of the spectrum. A 25 μm pinhole size is determined to be optimal in this microscope based on this analysis and the range of available pinhole sizes.

Once filtered only the spectral content of the beam is of interest rather than the image so strict adherence to conjugate planes is no longer necessary. The beam is split 50:50 into two signals, with one going to the benchtop spectrometers and the other to a fast spectroscopy path.⁸

⁸The fast spectroscopy technique is developed and implemented but otherwise not used in any experiments

The benchtop spectroscopy signal is further split into linear s and p polarisation components using a broadband polarising beamsplitter cube (Melles-Griot 300–1100 nm). Broadband polarisers (Thorlabs 500–1500 nm) oriented along the s and p axes are placed at the cube output ports to increase the extinction. Each polarised signal component is then finally focussed into multi-mode fibres, using short focal length (11 mm) lenses to achieve a spot size smaller than the fibre core. 100 μm fibre core is used instead of 50 μm to reduce laser speckle in spectra since the confocal pinhole diameter already localises the signal. The spectral signal from each of the fibres is recorded using TE-cooled, benchtop spectrometers (Ocean Optics QE65000 and QE Pro) with integration times between 10–50 ms. The sensitivity of the Si detectors in the spectrometers drops off beyond 900 nm, imposing a limit to detectable signals of around 1100 nm. The supercontinuum laser imposes a 480 nm spectral cut-on, resulting in an overall effective measurement window of 500–1100 nm.

Measured spectra are background-subtracted, to remove dark counts, and referenced to the spectral density of the supercontinuum illumination as transmitted through the microscope optics. Use of the intense supercontinuum source means low integration times below 20 ms are sufficient to near saturate the spectrometer for a high quality signal to noise. The high brightness of the supercontinuum laser at these exposures also means that the relative intensity contribution from external light sources is negligible. The coherence of the supercontinuum laser means that conventional referencing using scatter from a white diffuser to map the illumination spectral density is not possible. Instead, reflections from thin, reflective substrates attached underneath the piezo-mounted tip mount are used as a reference. Different substrates are used depending on the sample. For metallic samples the substrate is matched to the metal so only structural spectral features are observed. Otherwise either a Ag mirror or glass slide are sufficient for referencing as they provide relatively flat reflectances across the visible-NIR spectrum. The DF iris is kept fully open during reference acquisition to ensure the full spectral content of the incident beam is measured and to avoid introducing referencing artefacts. As optics are very rarely broadband between 500–1100 nm, all non-essential pathways are closed when acquiring spectra to prevent artefacts. Back reflections off lenses are found to superimpose a weak duplicate of the illumination spectrum onto spectra since the reflections are translated in k -space and are therefore not completely filtered by the DF iris.

4.2.2 Characterisation of Microscope Performance

During most experiments the power incident on samples is kept below 1 mW corresponding to a focal intensity of $\sim 10^8 \text{ mW cm}^{-2}$. This is used to maintain sufficient signal quality whilst preventing damage or destructive changes to nanoscale Au samples (typically 50 nm Au coatings). Beam profiling is used to characterise beam propagation in the microscope and determine its

in the current project. For this reason it's operation is omitted from this work.



Figure 4.6: Beam profiling of dark-field filtered supercontinuum illumination (red) and scattering collection (green) beam lines. Supercontinuum laser light is reflected back from a Ag mirror in the objective focus to characterise the illumination pathway. The spectroscopy pathway is characterised by coupling a 532 nm laser into a single mode fibre and passing it through the collection optics with the DF-iris closed to 2 mm. The stated axial distance z is twice the displacement of the mirror to account for reflections to the focal plane. Lateral distances are calculated using the CCD array size and pixel dimensions. (a) Lateral beam profile of the illumination and collection focusses as measured on the CCD. (b) Intensity cross sections through the lateral beam profiles of the illumination and collection. (c) Axial cross section through the focus of illumination and collection beams. (d) Normalised summation of spectrometer counts of confocally localised supercontinuum light passing through the collection optics.

ability to collect DF spectra. Profiling is carried out using focal scans of both light reflected from a Ag mirror and light scattered from an 80 nm AuNP, measured simultaneously on a CCD and a spectrometer. The CCD is used to laterally profile the beam through the focus while the spectrometer characterises the confocal profile and spectral distribution of the light. Both the illumination and collection pathways are profiled. The illumination pathway is profiled using the DF-filtered supercontinuum beam while one of the collection fibres is removed from its spectrometer and coupled to a 532 nm single mode laser in order to profile the collection pathway.

Figure 4.6 shows both the lateral focal spot on the CCD and relevant cross sections along the optical and focal axes for both the illumination and collection optics, along with depth-profiling using broadband-integrated spectra. Figure 4.6a shows the beam structure in the

./3_test_rig_design/./figures/axial_chromatic_aberration.pdf

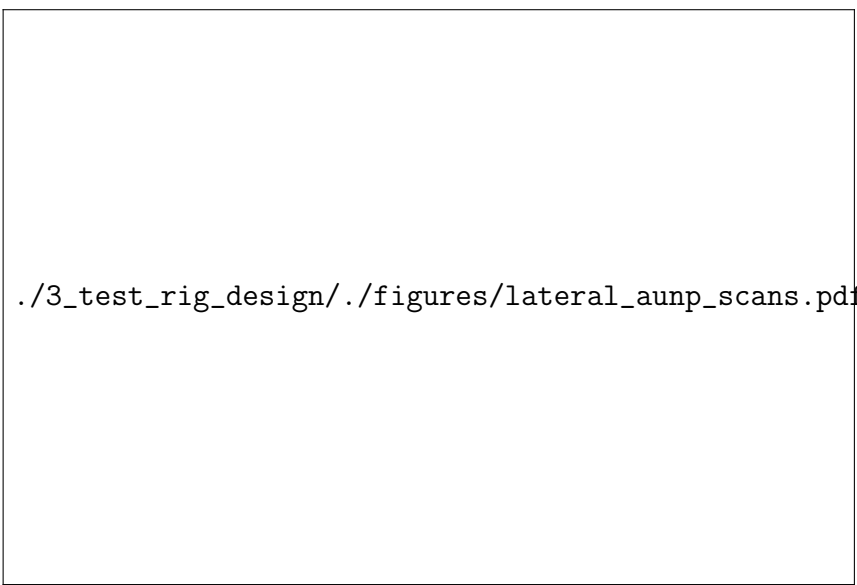
Figure 4.7: Axial chromatic aberration at each wavelength through the objective focus.

The image is formed from spectra of the *s*-polarised component of a reflection from a Ag mirror scanned through the focus. An intensity plot normalised for each wavelength is shown to determine depth of focus. The white indicates the position of maximum signal along the optical axis for each wavelength and shows the distinctive bowing curve of chromatic aberration.

focus. The single mode fibre output exhibits the characteristic Airy profile expected of a Gaussian beam while the ring aperture of the supercontinuum beam leads to more power concentrated in the outer rings of the focal pattern (Figure 4.6b). The measured FWHM of the collection beam is (460 ± 20) nm with a beam waist ($1/e$ width) of (540 ± 20) nm. The $47\times$ demagnified image of the $25\text{ }\mu\text{m}$ pinhole is expected to be 530 nm. The focal radius of a single mode Gaussian beam (the beam waist) is given by $w_0 = \lambda/\pi NA$, which results in a collection NA of 0.62 ± 0.02 . Measurement of a Rayleigh criterion length of (530 ± 20) nm indicates the beam is focussed through 0.61 ± 0.02 NA. Uncertainties on these calculations of the NA are small since the 532 nm wavelength is well known. Both calculations of the NA only partially agree due to beam focussing at the diffraction limit and both show a collection half-angle of $(38.0 \pm 0.5)^\circ$.

The axial cross section of beams (Figure 4.6c) shows the focussing of the high angle ($0.64\text{--}0.8$ NA, $40\text{--}53^\circ$ incident angle) supercontinuum ring. The boundary between incident and collection beams is measured to be around 0.62 in both beam angle and spot size measurements since the DF iris diameter and the DF stop diameter are both set to 2 mm. The axial beam profile, however, measures the angle of light from the focus to below $(21 \pm 1)^\circ$ (0.35 NA). This is likely caused by observation error due to the low intensities at high angles. After confocally filtering the depth of focus, as measured on the CCD beam profile, is on average $4\text{ }\mu\text{m}$ across the supercontinuum wavelength range (Figure 4.6d).

Figure 4.7 shows the individual wavelength components that make up the integrated spectral signal in Figure 4.6d. As expected the depth of focus increases with wavelength. The depth varies from $(2.8 \pm 0.1)\text{ }\mu\text{m}$ at $\lambda = 500$ nm to $(6.4 \pm 0.1)\text{ }\mu\text{m}$ at $\lambda = 1100$ nm. The chromatic structure of the beam is non-linear and shows that the colour maxima for $\lambda < 550$ nm and $\lambda > 800$ nm occur slightly offset from the pinhole position. Overall this does not de-



./3_test_rig_design/./figures/lateral_aunp_scans.pdf

Figure 4.8: Hyperspectral scans of AuNPs used to characterise the lateral PSF with different confocal pinhole diameters. (a-c) Wavelength slices of AuNP scans on resonance using 25 μm and 50 μm diameter pinholes and finally no pinhole, respectively. (d) The extracted PSF from line profiles across the images (a-c). (e) Spectra of AuNPs imaged. Localisation is observed with reduced pinhole diameter as the concentric illumination rings are cut.

tract much from the measured spectra since intensity differences in the chosen focal plane are normalised with the reference spectrum.

Lateral localisation is more important to consider than axial sectioning. Scattered light from a sub-wavelength size nanoparticle provides a point source from which the PSF can be measured across a small, resonant bandwidth. By (raster-) scanning a strongly-scattering MNP under the beam its point scattering response is convoluted with the beam structure in the focus. The size of the confocal pinhole determines how much of this beam structure is laterally filtered prior to spectroscopy and thus, by measuring the scattering spectra, the actual PSF, as seen by the spectrometers, can be mapped across a broad range of wavelengths. It is this function that determines the specific locations from which spectra are collected and becomes particularly important when attempting to measure localised scattering from an extended nanostructure.

Figure 4.8 shows scattering profiles extracted from AuNP scans, demonstrating the effective spectral PSF for a range of pinhole diameters. 80 nm AuNPs on glass resonantly scatter at 550 nm due to excitation of the dipolar LSP. A single AuNP was chosen on which multiple scans were performed, changing and realigning the confocal pinhole in between each scan. Wavelength slices at the AuNP SPR (Figure 4.8a–c) show the lateral effective PSF. Without a pinhole in place the spectral PSF is a convolution of the focal beam profile shown in Figure 4.6a. The spectrometer sees the scattering from all the concentric rings in the focus so localisation of spectral features would only be somewhat possible. Decreasing the pinhole diameter filters

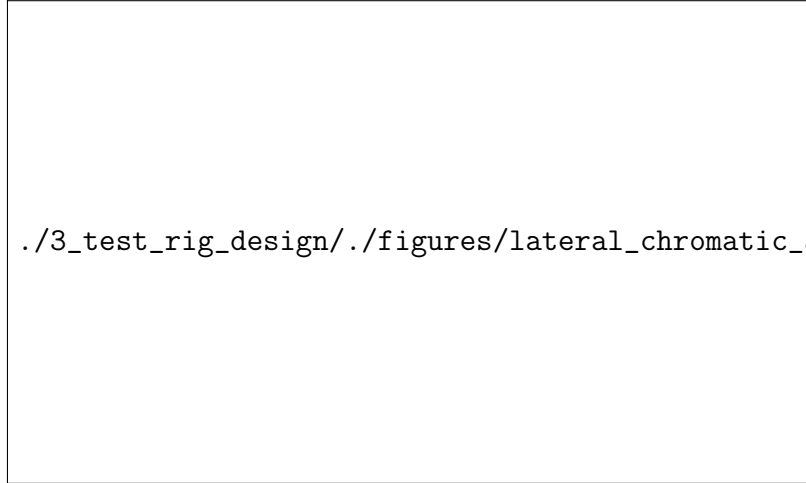


Figure 4.9: Measurements of lateral chromatic aberration across the plasmon resonance scattering bandwidth from hyperspectral images of AuNP. The central position of the scattering centroid is extracted from images at each wavelength. Changes in centroid position with wavelength signify chromatic aberration.

scattering from the focus and removes the contributions to spectra from the outer rings until spectra can only be acquired from the central spot. This guarantees localisation of observed spectral features to a finite-sized region. The FWHM of the scattering signals on resonance are (255 ± 25) nm with the 25 μm pinhole in place, (260 ± 25) nm with the 50 μm pinhole in place, and (300 ± 25) nm without a pinhole. The FWHM at 900 nm for the case of the 25 μm pinhole is 410 nm for reference. Due to the single AuNP being the only source of scattering in each of the scans the measured spectrum is the same for all pinholes (Figure 4.8e). Though the resolution is not improved by a great amount, use of the smaller pinhole does guarantee better spectral localisation, as seen by the presence of only the central maximum in its PSF.

Fitting the centroid at every wavelength in the spectral data cube identifies lateral chromatic aberration in the microscope. This is an important parameter to consider when using hyperspectral imaging or when acquiring spectra. For example, if the chromatic aberration is systematic and fitted then a correction offset can be added to hyperspectral data cubes at each wavelength. Spectra from each pixel can then be further recombined into regular RGB images by integrating the spectra at each pixel with RGB pixel spectra.

Figure 4.9 shows the centroids of the PSFs across the SPR band for each pinhole diameter. Scattering centroids are extracted from each wavelength slice using discrete image moment analysis, where i, j denote the moments of the x, y axes.⁹ The position of maximum scattering is then given by, Displacements are scaled relative to the centroid position on resonance where

⁹Note that the discrete image moments are based on the continuous moment theorem with moments given by

$$M_{ij} = \int_{-\infty}^{\infty} \int_{-\infty}^{\infty} x^i y^j f(x, y) dx dy.$$

the signal is highest. The centroid position drifts almost linearly by 80 nm in the x -direction and 80 nm in the y -direction. Since the pinhole only filters the outer rings of the PSF there is very little difference in the centroid positions between pinholes. As the range of centroid displacement in each direction is well below the diffraction limit and corresponds to only a few pixels offset in each image, the aberrations are not considered to negatively impact spectroscopy.

To summarise, a microscope platform has been designed to accommodate various sample geometries, specifically AFM tips. Single nanostructure spectroscopy is enabled by utilising an ultra-high brightness supercontinuum laser in a dark-field optical geometry and capable of measuring spectra between 500–1100 nm with short exposures, as low as 10 ms. Beam profiling clearly shows that the supercontinuum dark-field technique works as expected and that spectra are collected from a small volume in the objective focus due to confocal localisation.

4.3 Electronics Design

By applying a voltage, V , and measuring the current, I , the conductance, G , of a conductive junction between tips can be determined using $I = GV$. Using this, quantum electronic transport can be measured and correlated with optical measurements to gain a sense of spatial separation and the extent of charge transfer across the gap.

The experimental chamber contains two triaxial connectors, one attached to each Cu tip clamp, to send and return electronic signals, permitting biasing and electrical measurement of the gap between AFM tips. Electronic signals are controlled and redirected using a control box, which attaches to the chamber triax cables. Electronics are split between an a.c. circuit that drives a resonant capacitive tip alignment procedure and a d.c. circuit for electrical measurements. The d.c. electronics are further split into low and high bandwidth measurement

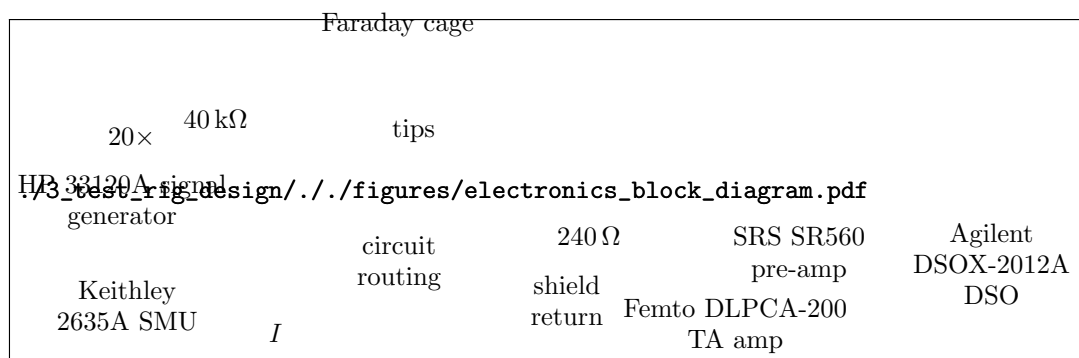


Figure 4.10: Block schematic of the electrical circuit design. The central routing box allows switching between a.c. and d.c. circuits and low-and high-bandwidth d.c. measurements. The a.c. circuit is used to align two AFM probes together while the d.c. circuit is used to measure spatially dependent signals from the gap between two AFM probes.

circuits. The low bandwidth (< 10 Hz) circuit measures electronics continually over long time periods, typically giving spatial information linked to sample separation. The high bandwidth circuit operates on a trigger to capture single shot events on much shorter time scales. Both d.c. circuits are typically ran simultaneously while the a.c. and d.c. circuitry is manually switchable. A block schematic of this system is shown in Figure 4.10.

The a.c. circuit consists of a signal generator connected to a $20\times$ voltage amplifier to drive the junction capacitance. This is used to resonantly drive an AFM cantilever into oscillation and align tips into a tip-to-tip dimer configuration. A $40\text{ k}\Omega$ current limiting resistor is placed after the amplifier to prevent damage to the tip junction in the event of a direct conductive contact.¹⁰ The return signal from the circuit is then terminated at ground. The separate d.c. circuit consists of a source-meter unit (SMU) circuit for low-bandwidth (sub-10 Hz) measurements with a switchable high-bandwidth measurement extension. The SMU (Keithley 2635A) is used to apply a voltage across the junction and measure the current. The switchable high-bandwidth path routes the current through a $10^4\times$ gain transimpedance amplifier (Femto DLPCA-200) followed by a 1 MHz low-pass filtering stage (SRS SR560). The amplified voltage is measured on a digital storage oscilloscope (DSO) (Agilent DSOX-2012) with the shield becoming the return path of the current back to the SMU via the routing box.¹¹

The fundamental feature of the combined circuitry is their separability. The a.c. circuit is not required to be low-noise but the d.c. circuitry is used to measure low-level tunnelling currents. For the d.c. circuit to operate correctly it must be isolated from all other electronics. The a.c. circuit remains completely disconnected and held at ground when the d.c. circuit is engaged, and vice-versa. To achieve measurements of small, sensitive currents, reducing the noise level to a minimum is imperative. The noise floor at low bandwidths, along with the current range of the SMU, sets the minimum current which can be measured. The sub-10 Hz bandwidth of the SMU removes much of the noise during spatial measurements. Correct grounding of all electronic chassis to a single point (the SMU) shields EMI and prevents ground loops from inducing current offsets. Triax cabling is used with guarded connections where possible to prevent leakage currents.

A standard operating voltage between 10–50 mV is used to drive high quality tunnelling currents. Conductances greater than $10^{-8}G_0$ are then clearly measured above noise. Using lower voltages means currents are only observable for larger tunnelling conductances, i.e. smaller gap widths, whilst higher voltages lead to larger overall currents and electrostatic interaction between tips, both of which should be avoided to prevent damage to the tip junc-

¹⁰The optimum resistance value is calculated using $R = V/I_{\text{limit}}$ where $V = 10\text{ V}$ typically and a safe current limit is $I_{\text{limit}} = 250\text{ }\mu\text{A}$. This gives a resistance of $40\text{ k}\Omega$.

¹¹An alternative strategy for converting a current into a voltage is to pass the current through a well-known resistor and differentially amplify the voltage drop across the resistor. This was not used since the transimpedance amplifier was readily available and of a low noise specification.

./3_test_rig_design/./figures/hb_electronics_limits.pdf

Figure 4.11: Characterisation of electronic measurements based on junction conductance. Solid lines show the calculated SMU currents and amplified voltages for given junction conductances under a 50 mV applied voltage with a $241\ \Omega$ current limiting resistor to prevent saturation (high bandwidth circuit). Dashed lines show the calculated oscilloscope voltages for the case without the current limiting resistor (low bandwidth circuit). Circles mark experimentally measured points using resistors in place of the junction in both circuits. Error bars are present but too small to visibly see.

tion. To maintain good scan speeds the current range is restricted to 10 nA with a ± 10 pA error, since more accurate ranges have longer settling times. Limiting the current range is the dominant source of current measurement error as opposed to the noise floor.

Noise on the SMU is measured by varying a series resistance in place of the tip junction and taking the standard deviation of 20 measurements across a range of voltages in 10 mV steps. The open circuit noise measures ± 10 pA. Johnson noise for such a circuit is estimated to be around 1 pA. If current measurements are strictly limited by the current range then the percentage error of each range should be equivalent. This is not the case, with the percentage error increasing from $10^{-3}\%$ to $10^{-2}\%$ as the current decreases to the nA range, signifying the approach of the noise floor. Actual noise levels around ± 100 pA are found at 50 mV with a $1\ \text{M}\Omega$ ($10^{-2}G_0$) junction resistance characteristic of electron tunnelling in the quantum regime of plasmonics. Given the small percentage errors, circuit noise is not a problem for tunnelling current measurements.

Noise predominantly affects high bandwidth measurements, where it limits the conductance resolution and minimum trigger level for single shot measurements. High bandwidth noise typically originates from digital circuitry, e.g. switch-mode power supplies and powered relays. Power supplies are therefore covered in foil to shield EMI and manual toggle switches are used instead of remote-controlled relays. Applying a 1 MHz filter goes some way to reducing high bandwidth noise. Any more filtering smooths measurements too much.

The maximum allowed current is set to 250 μA to prevent damage to contacted AFM

tips. Upon surpassing this limit the SMU attenuates the voltage to reduce the current. A current limiting resistor is also included in the circuit to ensure a hardwired maximum and to prevent overloading of the DSO and transimpedance amplifier. The value of this resistor is calculated using, where V is the operating voltage, A is the amplifier gain and V_{overload} is the minimum overload voltage for the circuit at a given voltage V (determined by whichever overload voltage is surpassed first, either the maximum transimpedance input current of 5 mA pre-amplification or the maximum output voltage of 5 V). The pre-factor of 0.95 is chosen to prevent the current getting close to overloading. For a 50 mV bias and 10^4 gain the ideal resistance is $175\ \Omega$ but for a 10 mV bias with 10^5 gain it increases to $350\ \Omega$. To accommodate a range of voltages and both gain settings, a middle resistance of $241\ \Omega$ is used, which provides some headroom for increasing the voltage at the lower gain. The calculated current and DSO voltage as a function of junction conductance for the low and high bandwidth circuits is shown in Figure 4.11. Excellent agreement with experimental current and voltage measurements taken with a set of resistors demonstrates the circuit behaves exactly as predicted.

The presence of the current limiting resistor means that measured circuit conductances, G_{measured} , contain a series resistance that needs to be taken into account. Junction conductances are calculated using, The maximum conductance value that can be measured is found by inverting the limiting resistance using $G_{\text{max}} = 1/R$. For a 50 mV bias the conductance limit is $53G_0$. Conductances greater than this value are small compared to the series resistance and are therefore much harder to measure reliably. For this reason the range of interesting conductances ($G < 20G_0$) is ideally kept to the linear part of the current curve by limiting the voltage and gain.

4.4 AFM Design: Measurements of Force

An AFM module measures cantilever deflections as they flex under an applied force. The linear displacement of the cantilever, Δz , from its equilibrium position under an applied force, F , is simply given by, where k is the stiffness or spring constant of the cantilever. Contact and tapping mode cantilevers are mostly used in experiments, for which $k = 0.2\ \text{N m}^{-1}$ and $40\ \text{N m}^{-1}$, respectively. The change in angle caused by a linear displacement at the tip can be measured optically as a change in deflection angle of a laser focussed on the back of a reflective cantilever (Figure 4.12). The sensitivity of this technique has led to it being named atomic force microscopy since atomic-scale forces cause measurable deflections, enabling topological imaging with nanoscale resolution. For tip-tip dimers, nano-scale force measurements become important as they dictate how tips come together and move through interfacial layers prior to electrical contact. To this extent, a compact AFM module was constructed to monitor the tip-tip interaction forces during tip dimer measurements.

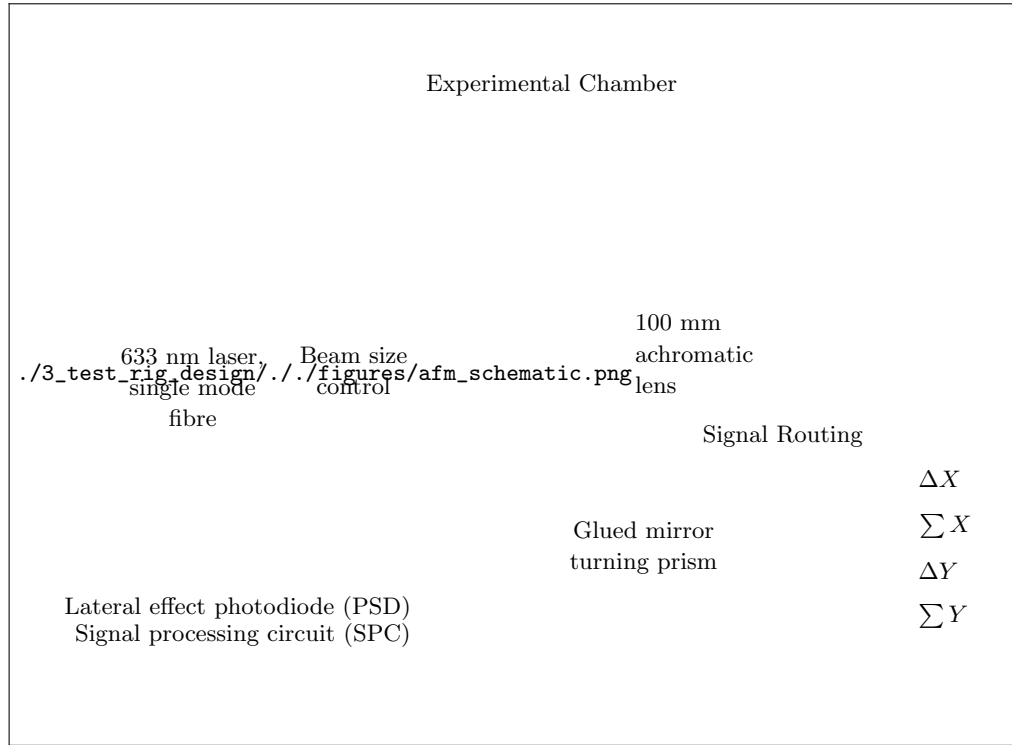


Figure 4.13: Schematic diagram of the AFM module attached to the side of the microscope platform. Incident light from a single mode fibre is focussed at an angle onto an AFM cantilever. Angled reflections from the cantilever are re-collimated into a laterally displaced beam whose position is detected on the PSD.

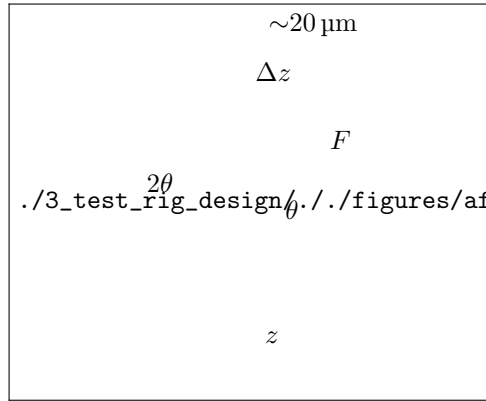


Figure 4.12: Concept of contact mode AFM. An applied force \mathbf{F} bends the cantilever proportional to a linear displacement x . Light incident on the bent cantilever deflects at an angle 2θ .

The AFM module consists of a compact optomechanical **array**, mechanically bolted onto the top plate of the microscope platform, and a separate 633 nm laser diode coupled together using a strain-relieved single mode fibre, as shown in Figure 4.13. Single mode fibre is used to produce a stabilised laser output.¹² Light is focussed through an entry window in the experimental chamber onto the cantilever of the soft AFM probe during an experiment. The beam position is laterally offset on the focussing lens using a silver turning prism to focus on the cantilever at an angle so that reflections return through the AFM with the opposite lateral offset.¹³ Light reflected back off the cantilever at a different angle in the focal plane is laterally translated in Fourier space. This

¹²Stabilised output results from single mode operation. Multimode stability leads to significant intensity changes that cause issues with the position sensitive detector.

¹³An alternative to this approach allows use of a common beam path but requires two polarisers and a quarter wave plate, leading to simpler alignment but a more costly design.

translation is measured using a fast lateral effect photodiode, also known as a position sensitive detector (PSD). The PSD contains a signal processing circuit with an in-built transimpedance amplifier (10^5 gain) to convert the small currents generated into voltages corresponding to the measurements $\Delta x, y$ and $\sum x, y$. Voltages are recorded using a DAQ card (NI X-series).

The width of the cantilever and the radius of the input beam determines the minimum beam size. Cantilevers have a width of $50\text{ }\mu\text{m}$ therefore the spot size in the focus must be less than this value. Since the input is a single mode Gaussian beam the spot diameter, $2w_0$, is given by $2w_0 = 4\lambda f/\pi D$, where f is the focal length and D is the collimated beam diameter. For $\lambda = 633\text{ nm}$ and a required spot size $2w_0 < 50\text{ }\mu\text{m}$ the fraction $f/D < 62$. The focal length is restricted by the distance from the edge of the top plate, where the AFM module is mounted, to the cantilever through the chamber window. A 100 mm lens is chosen to accommodate the focal length constraint, which restricts the beam diameter to $D > 1.6\text{ mm}$. This beam diameter is set by using a short focal length lens to collimate the single mode fibre output.

Changes in the voltage output of the PSD correlate with the force applied to the tip at the end of the cantilever. The position of the PSD is adjusted with zero force applied to the cantilever to zero the voltage. The lateral displacement of the returning beam is then calculated using, where i is the lateral axis, either x or y , L_i is the length of the detector along that axis and V_i is the voltage output at each end of the detector axis. The displacement can then be transformed into an applied force via a calibrated conversion.

4.4.1 Calibrating the AFM

The displacement of the tip under an applied force can be related to the translation of the beam as a measured voltage. By determining the tip displacement, the force applied to the AFM tip can be measured using Eq. ???. The transformation from tip displacement into a measured lateral displacement can be expressed as, where $k_{x \rightarrow s}$ is the transformation. In the current geometry this transformation is linear and therefore $k_{x \rightarrow s}$ is a fixed constant for a given AFM beam alignment. In general, $k_{x \rightarrow s}$ includes each of the transformations required to convert the cantilever displacement into a measurable signal. These transformations are apparent when following the path of the laser beam through the AFM module. The tip displacement needs to be converted into an angular cantilever deflection, which is further transformed into a lateral beam translation. Each of these is a linear operation, hence the overall effect can be expressed in a single constant $k_{x \rightarrow s}$, which can be experimentally determined.

The simplest method of calibration involves pushing an AFM tip against a hard contact so that the displacement is known ($\Delta z = z$). From there the beam translation is measured as a function of tip displacement and data can be fitted to determine $k_{x \rightarrow s}$. The force can then be estimated using Eq. ???. Whilst this is not ideal as the cantilever spring constant is still

somewhat unknown, the method is simple. Therefore, for force measurements, the value of the cantilever spring constant is assumed from the AFM probe data sheet. The large tolerances on stiffness measurements mean that this approach is only sufficient to estimate the applied force on a nano-gap to within 50%.¹⁴ Other methods of accurately measuring the cantilever spring constant do exist, as do methods to directly map the force to a measured signal, i.e. $F = k_{s \rightarrow F} s$, but add further complexity to experiments [179–187]. Since exact measurements of force are not crucial to current nano-gap studies, the current uncertainty is acceptable.

4.5 Scanning Capacitive AFM Tip Alignment

A significant challenge when attempting to recreate a plasmonic dimer using opposing AFM probes is the alignment of tips with the focussed laser spot in a symmetric tip-to-tip configuration. This capability is necessary to permit the majority of dual tip experiments and forms the first step to measuring the dynamical physical response of plasmonic tip dimer systems. For successful experiments the tolerance on the tip-to-tip alignment is less than $\mathcal{O}(R_{\text{tip}})$. Aligning tips using CCD imaging is limited by diffraction and therefore unsuitable. Initially this problem was solved using a non-linear capacitive alignment technique that required locking into the third harmonic of the driving signal [188]. Whilst functional in simpler systems, the technique was limited in its accuracy by the small pA level currents in the third harmonic mode and the extensive filtering and lock-in techniques required to measure these. A simpler approach is to simply use the AFM module optics to measure the oscillating cantilever deflection. This is more widely known as scanning capacitance mode AFM (SC-AFM) or scanning capacitance microscopy (SCM), and has been used in the past to measure the dopant levels in semiconducting substrates [189–193]. By utilising optical detection over direct electronic measurements tip alignment becomes segregated from the microscope electronic d.c. measurement circuitry and issues are no longer caused by noise leaking into the a.c. electronics.

4.5.1 Mechanism for Alignment of Two Opposing Tips

To a first approximation the metallic tips can be ignored and only the capacitive interaction between planar cantilevers is considered. Cantilevers are separated by a distance $d(t) = z_1(t) - z_2(t)$ and coupled via the z -components of the long range, attractive, electrostatic driving force F_{EL}^z and short range Van der Waals and repulsive tip-tip interaction forces F_{TT}^z . Each cantilever has an associated spring constant k_{0i}^z , mass m_i and resonant frequency of oscillation $\omega_{0i} = \sqrt{k_{0i}^z/m_i}$. When vibrated, cantilevers oscillate around an equilibrium position z_{0i} . The equilibrium separation between tips is then denoted by $d_0 = z_{01} - z_{02}$.

¹⁴The fractional uncertainty is given by $\delta F/F = \sqrt{(\delta k/k)^2 + (\delta z/z)^2}$ for which $\delta z/z$ is negligible compared with $\delta k/k \approx 0.5$.

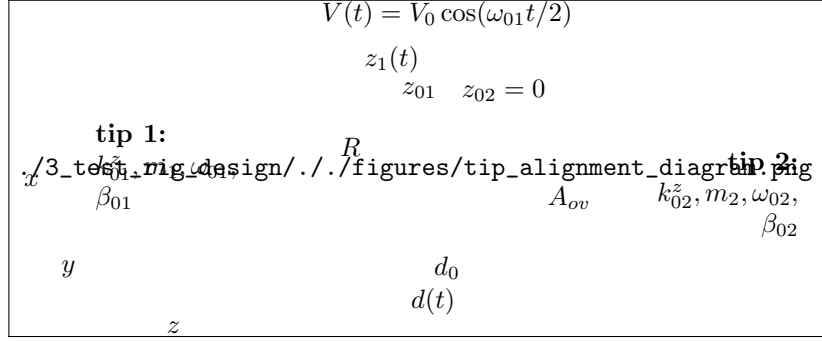


Figure 4.14: Diagram of tip alignment parameters. The position of one tip relative to the other is detected using a resonant scanning capacitance AFM technique. The gap is biased with an oscillating voltage to induce a resonant vibration of one of the AFM cantilevers. The amplitude of oscillation is sensitive to the gap size d and the area of overlap A_{ov} between tip features of characteristic size R . For sharp tips R is the apex radius whereas for nanostructured tips R is considered to be the feature size.

The equation describing motion in the z -axis of the two parallel cantilevers, denoted by $i = 1, 2$, of spring constant $k_i^z = k_{0i}^z + k_{TT}^z$, coefficient of damping $\beta_i^z = \beta_{0i}^z + \beta_{TT}^z$ and mass m_i , is given by, where the sign of the force depends on the tip - positive for one tip and negative for the other. Assuming that alignment takes place at long range, tip-tip interactions can be ignored, therefore $F_{TT}^z = 0$ and $\beta_{TT}^z = k_{TT}^z = 0$. The system is further simplified by assuming that one cantilever remains stationary by being stiff (tapping mode $k \approx 40 \text{ N m}^{-1}$)¹⁵ and always being off resonance ($\omega_{01} \neq \omega_{02}$). This is usually satisfied in experiments where a stiff cantilever is required such that the optical probe is incident on the same sample area whilst under force. The apex separation is then restricted to $d = z_1$ with an equilibrium separation $d_0 = z_{01}$. Under these conditions the motion reduces to that of a single tip, This equation now describes the whole system rather than each individual tip with the main reference point between tips being the equilibrium separation d_0 .

The remaining capacitive driving force exerted between tips is purely electrostatic and of the form, where $\omega_p = 2\omega_s$ is the cantilever pump frequency. Substituting Eq. ?? into Eq. ?? gives the simplified equation of motion for the dual-tip system, Driving at a pump frequency close to the cantilever resonance ($\omega_p \approx \omega_{01}$) leads to a resonant oscillation between tips. For small oscillations around d_0 , Eq. ?? can be Taylor expanded to first order into the form of the damped Mathieu equation¹⁶ with an approximate solution¹⁷ where in which $\langle k_{e1}^z \rangle$ is the effective spring constant of the system, $\langle k_{e1}^z \rangle = k_{01}^z - \epsilon_0 A_{ov} V_0^2 / 2d_0^3$, taking into account the time-averaged electrostatic interaction. From Eq. ?? and Eq. ?? it can be seen that both the oscillation amplitude and phase relative to the driving signal vary with the equilibrium separation d_0 .

¹⁵This is based on data sheet values of almost all tapping mode tips.

¹⁶Damped Mathieu equation: $\ddot{z} + 2\kappa\dot{z} + [a - 2q \cos(2t)]z = 0$

¹⁷Full derivation available in the appendix.

Although the model is for two parallel plates, it becomes applicable to tips in a dimer configuration once the separation is sufficiently low that the tip-to-tip capacitance dominates over all other capacitive contributions (such as the cantilever or tip facet interactions). In this regime, if the tips stray out of alignment the tip-to-tip distance increases and the capacitance decreases, reducing the tip oscillation amplitude and the phase, hence tips are aligned when both the amplitude and phase are maximised. Both these properties are readily measurable using optical cantilever deflection in the AFM module.

Whilst optical detection gives a better signal-to-noise and measures at higher bandwidths, it should be noted that the capacitive model was originally developed to show that a $3\omega_s$ current signal can be used to align tips [188]. By driving the system with $\omega_p \approx \omega_{01}$, a mechanical parametric resonance is excited at $2\omega_{01}$ (otherwise only the fundamental is excited with resonant driving) and the current through the tip junction is given by, where $C_0 = \varepsilon_0 A^{ov}/d_0$ and z_{off} is an additional offset due to $F_{EL}^z \propto V^2$. Non-linear oscillations in the tip capacitance result in parametric frequency mixing in the electronics with resulting signals at the sum and difference frequencies, $\omega_p + \omega_s = 3\omega_s$ and $\omega_p - \omega_s = \omega_s$ respectively. The signal at $3\omega_s$ is background-free, as shown in Eq. ??, and once again depends only on z_{m1} and d_0 . However, currents are $\mathcal{O}(\text{pA})$ for acceptable driving voltages, therefore alignment only works over shorter ranges, and requires larger voltages to further boost the oscillation amplitude and low-noise detection electronics. Optical detection is advantageous as small oscillations at lower voltages are easily detectable, which protects the samples from damage caused by tapping between tips once the gap is small.

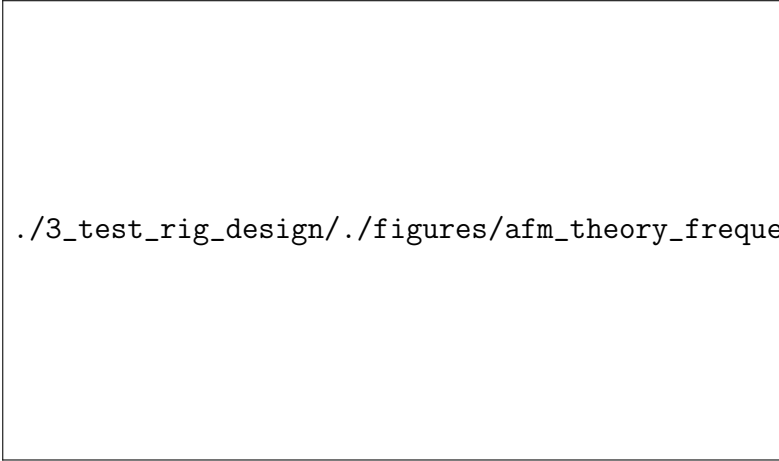
4.5.2 Numerical Solutions for Tip Alignment

Theoretical curves for the system response based on Eq. ?? for a typically used contact/tapping mode AFM probe dimer are solved numerically using an ordinary differential equation (ODE) solver.¹⁸ Results are intended to *qualitatively* demonstrate the alignment technique. The following table summarises the parameters of the model for each tip:

	Tip 1	Tip 2
k_0 (N/m)	0.2	40
ω_0 (kHz)	$2\pi.13$	$2\pi.300$
$\Delta\omega$ (Hz)	$2\pi.200$	$2\pi.200$
r (nm)	20	20

Table 4.1: Tip parameters used in numerical calculations. The dimer is assumed to comprise of a dynamic contact mode AFM cantilever (tip 1) and a fixed tapping mode cantilever (tip 2).

¹⁸ODE in Numpy/Python



./3_test_rig_design/./figures/afm_theory_frequency_response.pdf

Figure 4.15: Theoretical frequency response showing the amplitude and phase of a 13 kHz/300 kHz opposing AFM tip system. The tip junction is held at 10 V with a 100 nm intertip separation.

The plate area is assumed to be πr^2 where r is the radius of the tip. This is estimated to be $r = 20$ nm based upon standard tip apex dimensions. Changing this value does not change the overall qualitative shape of the data. The mass of each tip is calculated from the resonance using $m_i = k_{0i}/\omega_{0i}^2$. The damping coefficient of each tip is given by $\beta_{0i} = 2m\delta_i$ where $\delta_i = \omega_{0i}/2Q_i$ and $Q_i = \omega_{0i}/\Delta\omega$ (a quantity which is verifiable by experiment). Only the damping coefficient of the vibrating tip matters at any given time due to the large difference in resonant frequencies. To maximise the detected response the system is studied around the resonance of the soft cantilever. The system spring constant is given by, and the system mass is given similarly by,

The forces acting on the tip are described by a capacitive driving force, described by Eq. ??, and an interaction force. The interaction force is described by, where z_c is the equilibrium position, a is the amplitude of the oscillation, a_0 is the equilibrium separation and H is the Hamaker constant [194–197]. The capacitive driving force depends only on the time-averaged tip separation whilst the interaction force depends on the oscillation amplitude of the tip around its equilibrium position compared with the gap separation since this eventually leads to tapping on the opposite tip.

The ODE solving algorithm computes the change in the cantilever position and velocity in time using their respective differentials, where $F_{EL}^z(t)$ is the capacitive driving force described in Eq. ??, $F_i^z(z)$ is the interaction described in Eq. ?. The tip motion in time is solved, subject to stationary initial conditions, for 100 AFM oscillation periods. The steady state harmonic properties of the waveform are extracted using a sinusoidal fit to the last 50 periods, when behaviour has stabilised.

Figure 4.15 shows the calculated frequency response for a dimer comprised of a stiff, tapping mode cantilever and a softer contact mode cantilever. The modelled frequency response is

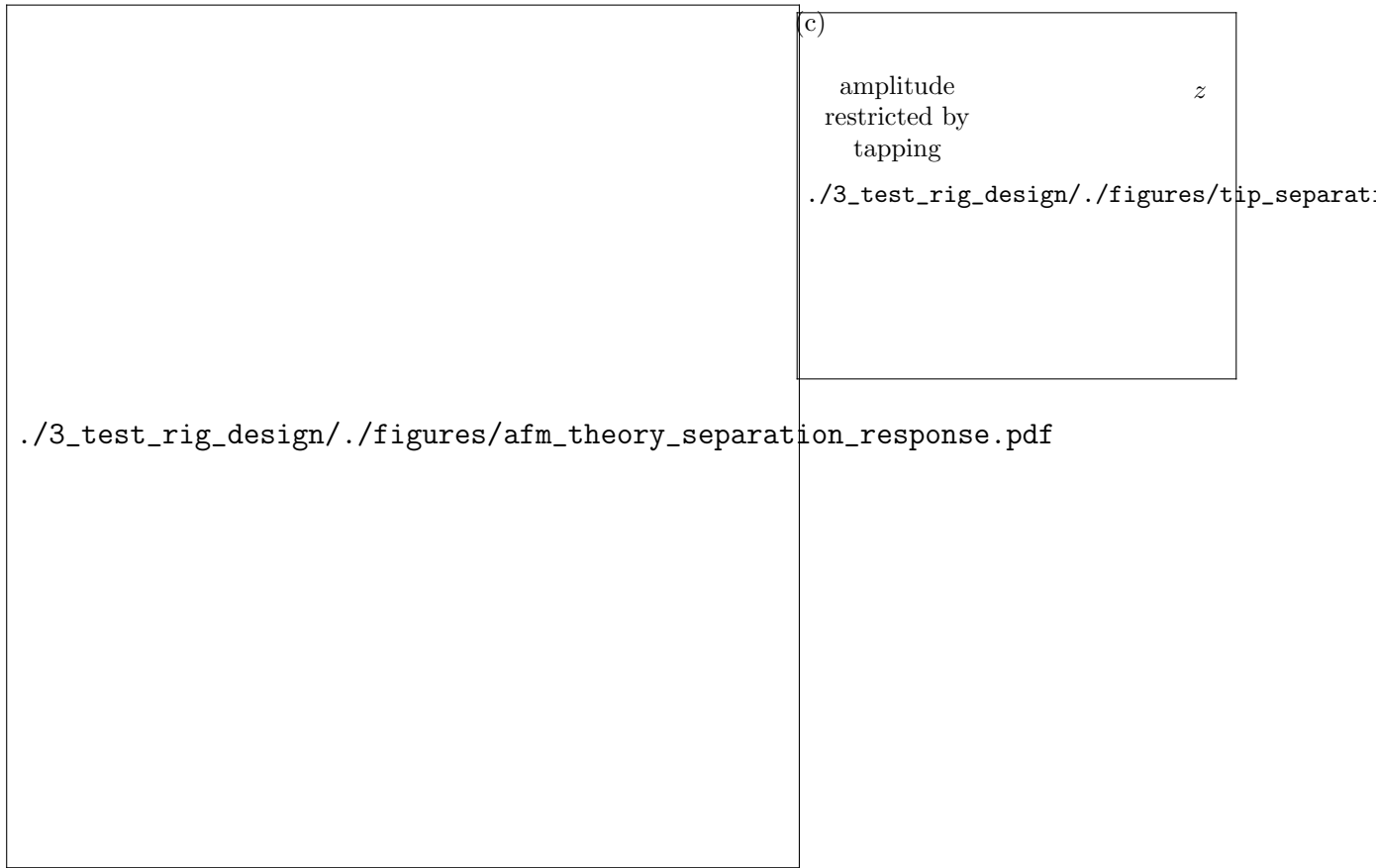


Figure 4.16: Theoretical separation response showing the amplitude (a) and phase (b) of a 13 kHz/300 kHz opposing AFM tip system. The voltage across the tip junction is varied while on resonance ($\omega_s = 2\pi \cdot 6.5$ kHz). The amplitude increases as the intertip separation is reduced. The dashed line shows the point at which the oscillation amplitude is equal to the separation. For separations below this limit, the hard surface restricts the amplitude to the gap between tips. A diagram of this is shown in (c).

determined by driving a spatially fixed tip dimer, separated by 100 nm, with a 10 V driving signal across a range of frequencies around $\omega_s = \omega_{01}/2 = 2\pi \cdot 13$ kHz/2. From this the cantilever resonance can be clearly seen. The amplitude line shape matches the expected Lorentzian response of a damped resonator and oscillations transition between in-phase oscillation when driving at lower frequencies and anti-phase oscillation at higher frequencies. This is standard resonator behaviour and is to be expected.

The intertip separation is then reduced while driving on resonance to find the separation response. The calculated separation response for the same contact/tapping-mode tip dimer is shown in Figure 4.16. As the separation decreases the capacitance between tips increases and resonant oscillation is amplified. This amplification occurs until the amplitude is equal to the separation, at which point the system transitions into the tapping mode of AFM imaging. This is shown by the linear relationship of unity gradient between amplitude and separation, regardless of voltage. In this regime the oscillation is restricted by the gap width between

tips, which limits the maximum possible amplitude. Calculations indicate that phase contrast only occurs once the oscillating tip comes into close proximity with the other tip. This onset of phase contrast occurs close to the point of maximum amplitude just before tapping. The phase is therefore a good indicator of alignment between tips. Tips can be considered to be aligned once the amplitude and phase centres agree. The accuracy of these solutions becomes limited when the separation is reduced well into the tapping mode regime as the oscillation is difficult to sustain and surface (interfacial) forces begin to dominate, leading to the snap-in effect.¹⁹ This instability is seen by the deviation of the amplitude from its linear decrease in the tapping regime followed by its rapid decay.

4.5.3 Experimental Measurements using Scanning Capacitance Microscopy

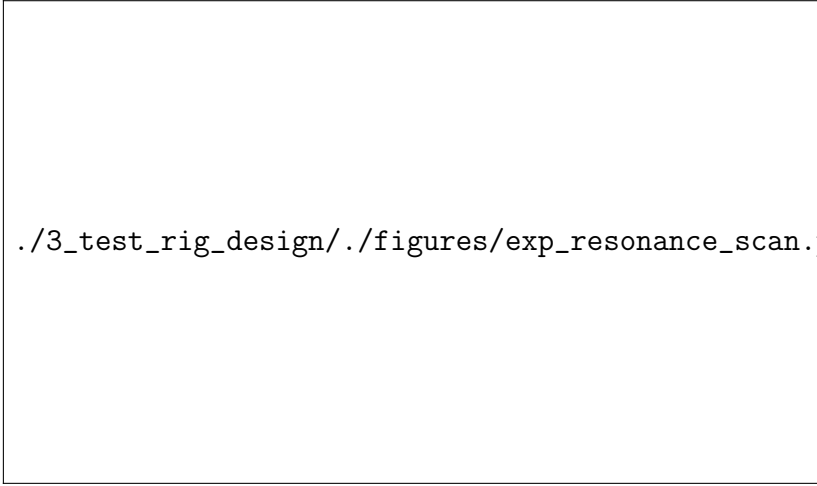
Experimental measurements of capacitive tapping mode tip interaction use the AFM optics on the microscope. The backside of the softer cantilever of the pair is illuminated by the 633 nm laser beam. By resonantly driving an AFM tip electronically its oscillation generates a signal $A \cos(\omega_p t + \phi)$ along one of the axes on the PSD. Lock-in detection is used to remove noise and add phase sensitivity to signal measurements by referencing the oscillation to the driving signal. The large oscillation signal permits the use of software lock-in detection rather than hardware, increasing the experiment simplicity and reducing the overall cost of the microscope. The NIDAQ device simultaneously acquires both PSD signals in each direction along with the driving signal from the function generator output. The second harmonic of the driving frequency, ω_p is locked-in using the reference periodicity. The phase difference ϕ is then measured relative to the reference phase.²⁰

The resonance frequency of the softer cantilever is determined prior to tip alignment at long range by scanning the driving signal frequency and measuring the cantilever response. The measured frequency response of a capacitively-driven contact mode AFM cantilever (Figure 4.17) agrees well with the modelled response (Figure 4.15). The resonance frequency is higher than expected due to the tolerance range of real AFM cantilevers. One noticeable difference is the linear gradient superimposed onto the phase response. This stems from time lags during acquisition which give a linear phase offset with increasing frequency.

The separation response is probed by aligning a soft (13 kHz, 0.2 N m^{-1}) tip to the position of maximum amplitude by laterally scanning the xy plane opposite a stiff (190 kHz, 48 N m^{-1}) tip. The soft tip is approached towards the stationary tip along the z axis and the cantilever response is measured. The rate of approach varies between 0.5–2 nm per step depending on

¹⁹Snap-in, also known as snap-to-contact, is an AFM phenomenon described in a later chapter as a result of capillary forces from a water meniscus in the gap.

²⁰The software lock-in procedure is detailed in depth in the appendices.



./3_test_rig_design/./figures/exp_resonance_scan.pdf

Figure 4.17: Resonance scan of a standard Au contact mode AFM tip opposite a standard Au tapping mode AFM tip. The soft tip (BudgetSensors ContGB) has a 13 kHz resonant frequency and the stationary tip is resonant at 190 kHz (BudgetSensors TapGB). Cantilevers are separated by $\sim 1 \mu\text{m}$ and driven at 15 V.

how far apart tips are separated. The amplitude is monitored in real time and the tip is retracted once the signatures of tapping are detected. Quick retraction is necessary as tapping with a soft cantilever is unstable to effects such as snap-in and short-range attractive forces. There is also a high chance of damaging the metallic tip coating during contact. Judgement of the retraction point is subjective but preserves the tip for multiple cycles. This approach-reaction cycle is repeated many times with a continuously reducing voltage until tapping is difficult to achieve without the oscillation immediately becoming unstable. This occurs once driving with less than 5–6 V.

Figure 4.18 shows the corresponding experimental curve to the numerically calculated separation response (Figure 4.16). The expected capacitive increase in amplitude followed by a linear tapping mode regime is qualitatively found in the experimental data. A significant difference from the model is that the baseline capacitive amplitude increase is not as drastic. This is likely due to the large extended shape of the tip and cantilever. This was not taken into account in numerical calculations which use only a simple parallel plate model. The linear decrease is also less steep suggesting that only the upper region of the modelled curve is visible. The amplitude instabilities found in the calculations at small separations are also found in the experimental data. Repeat approaches after such an instability show different peak amplitudes with the differences attributed to misalignment after contact, changes in tip morphology or surface modification. Interestingly, the discontinuous reduction in the phase is not experimentally observed. This means that either the separation was not reduced enough for this to occur before retraction or the model is not completely correct. Both statements are equally likely due to the simplicity of the model used. Overall the cantilever behaviour qualitatively matches many of the trends predicted using a simple mathematical model solved




Figure 4.18: Experimental separation response showing the amplitude (a) and phase (b) for a standard Au contact mode AFM tip approaching a standard Au tapping mode AFM tip. The same vibrating tip is approached and retracted with the voltage reduced between each approach cycle. The amplitude increases as the intertip separation is reduced until oscillation becomes restricted by the gap width.

using an ODE solver. As expected, the separation sensitivity of this technique makes it highly suited for tip alignment.

Another application for capacitive driving, demonstrated by Figure 4.18, is to use the long range interaction to lock the positions of the tips relative to each other, using the separation-dependent amplitude response as a feedback mechanism in a *pid* loop.²¹ Dynamic positioning and alignment between two tips can then be locked and maintained throughout an experiment to account for fluctuations due to either mechanical or thermal drift. Smaller separations can be locked by decreasing the voltage to reduce the amplitude up until the point at which the second harmonic signal becomes difficult to detect. The onset of tapping also limits the minimum achievable separation as the tip must remain oscillating. This technique could potentially become more useful if a stable plasmonic gap size is required for a long time whilst

²¹Proportional-integral-differential *pid* control loops are a form of feedback mechanism for stabilising a value at a preset target.



./3_test_rig_design/./figures/alignment_scan.pdf

Figure 4.19: Alignment scan of a soft Au AFM tip scanned laterally over a hard Au AFM tip. The soft tip is oscillating at 13 kHz (BudgetSensors ContGB) while the 190 kHz Au tip (BudgetSensors TapGB) remains static. Tips are separated by ~ 50 nm and driven at 8 V. Strong peaks are seen in both the amplitude and the phase of the soft cantilever oscillation. The tips are aligned in a tip-to-tip configuration when both signals are maximised.

the contents or properties of the gap are modified.

4.5.4 Experimental Alignment of Tips using Scanning Capacitance AFM

By mapping the lateral amplitude and phase variations of the cantilever deflection on resonance, two opposing tips can be experimentally aligned. Alignment is carried out on resonance by laterally scanning the oscillating, soft cantilever tip over the stationary tip whilst reducing the separation. The location of the opposite tip is then determined by the position of maximum amplitude and phase. To prevent tip collisions due to entering the tapping regime, the voltage is reduced along with the separation. This allows only the minimum required signal for positional analysis. Unlike the phase, the amplitude signal varies smoothly over a longer range. As the intertip separation decreases, the amplitude centroid converges on the position of the opposing tip apex and the phase begins to increase and form a sharp peak. By iteratively following the lateral position of maximum amplitude the tips can be brought into alignment. This procedure is advantageous as it operates at long range in the non-contact regime, prior to the tapping mode regime.

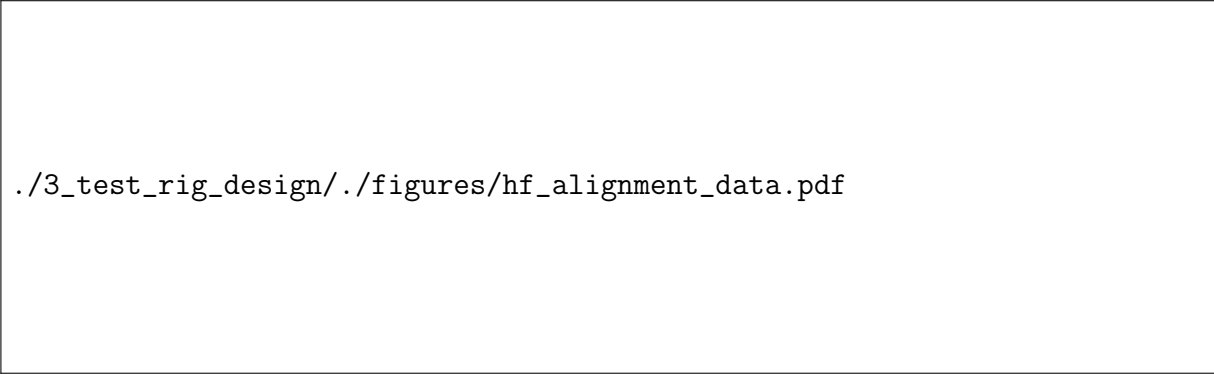
Figure 4.19 shows a typical alignment scan at close range with peaks in both the amplitude and phase. At this point during the procedure the tips are considered to be well aligned. Tips are then brought into alignment by identifying the position of the peaks. Since the tips are only symmetric along one axis, long range capacitive coupling is inhomogeneous and skewed until the distance between tips is small enough that the tip-to-tip capacitance



Figure 4.20: Centroid tracking during approach and alignment of two sharp Au tips. Amplitude (circles) and phase (squares) centroid positions relative to final alignment are shown in both the x (a) and y (b) directions. The centroid FWHM for the x and y amplitude and phase centroids are shown in (c) and (d), respectively. The final separation is an order of magnitude estimate based on the tapping mode linearity.

dominates interactions. Gaussian fitting is therefore potentially inaccurate in determining the peak location. Calculating the centroid from discrete image moments, given by Eq. ?? and Eq. ??, provides a more accurate, and faster, way of centring the scanned tip on the opposing tip. The centroid position after each scan is tracked as the intertip separation decreases from larger distances ($\sim 1 \mu\text{m}$) to around 50–150 nm as tips are brought into alignment. The centroids as a function of separation for a representative scan are shown in Figure 4.20.

Alignment is classified as the point at which the amplitude centroid is in agreement with the phase centroid. This criterion is chosen since the phase centroid does not deviate significantly from its initial position after emergence (Figure 4.20b). Its emergence also signifies that the separation is small enough that the response is dominated by the capacitance between tip apices. The amplitude centroid, on the other hand, follows the point of maximum capacitive coupling which depends on the separation regime and driving voltage (Figure 4.20a). The accuracy of the alignment can be quantified from the FWHM of both the amplitude and phase peaks. The FWHM of both centroids shortly after passing the alignment threshold constrict to a similar length. This is dictated by the feature size of the tip apex, such as the radius of a sharp or spherical tip apex. This limiting level of localisation is directly visible in the data (Figure 4.20c,d) where alignment using sharp Au tips results in a final FWHM between 10–30 nm. When studying spherical tips with 150 nm radii the FWHM remains much larger since the surfaces in close proximity are much flatter in comparison.



./3_test_rig_design/./figures/hf_alignment_data.pdf

Figure 4.21: High frequency alignment data for a tip dimer composed of two 48 N m^{-1} Au AFM tips. Tips are separated by $\sim 50 \text{ nm}$ and driven at 120 V . (a) Frequency response of the system. (b) Amplitude and phase alignment scans.

Alignment using this technique is limited to conductive tips for best results. Tips necessarily have to be conductive to generate a strong capacitive signal at the tip junction. Most tips used with this technique have therefore been from Au or Pt AFM probes, though alignment of Si tips has been demonstrated at higher voltages since they are doped to dissipate static charge. Due to the improved signal quality when using optical detection compared to electronics smaller oscillations are able to be used to align tips. For a standard sharp Au tip dimer (one contact, one tapping mode cantilever) alignment has been carried out at voltages as low as 2 V for small tip separations. The PSD also offers at 400 kHz bandwidth compared with the 100 kHz bandwidth of available electronic lock-in amplifiers, allowing stiffer tips to be aligned on the occasion where a stiff dimer is needed. A demonstration of this high frequency alignment is shown in Figure 4.21 where a large voltage of 100 V was used to induce a sufficiently large oscillation for signal detection.

To summarise, the capacitive alignment technique developed by Savage *et al.* [188] has been successfully adapted to use optical cantilever detection, as in AFM, instead of direct electronic measurements of the tip junction. The technique is greatly improved, is less sensitive to other electronic systems integrated into the microscope, and has demonstrated the capability to align two tips to within 10 nm of the target - less than the feature size of the tips. Both the frequency and spatial response have been studied, showing the tip separation dependence and the resulting alignment mechanism.

4.6 Conclusions

A custom-built ultra-stable microscope platform, utilising supercontinuum dark-field spectroscopy, low-noise electronics and AFM, is built to accommodate spectral studies of both individual tips and tip dimers. The platform is stable to both temperature and vibration and able to take two tips and align them into a dimer configuration using a modified form of scan-

ning capacitance microscopy. Performance characterisation shows spectral validity between 500–1100 nm, more broadband than standard optical microscopes, with confocal localisation enabling the study of more complex structures than point scatterers. The addition of fA level current and AFM force measurements results in a system capable of characterising a sub-nm plasmonic dimer system in far more detail than ever before possible.

As discussed in the theoretical background (chapter 2.3) only a small amount of work has been done to characterise and understand tips prior to applying them as optical nanoantennae. Understanding this interaction between tips and far-field light has been one of the main motivations of this project. A hyperspectral imaging technique is applied to laterally map light scattering from a tip with confocally localised spectra to infer a local optical response and better study tips. Understanding this response at the apex of single tips is of importance in determining their effectiveness as near-field enhancers and in understanding their coupling behaviour in the presence of another tip. In this chapter the spectra of single tips is discussed, studying both sharp and spherical-tipped Au AFM probes, along with the application of spherical Au tips to Raman spectroscopy.

5.1 Optical Characterisation of Nanostructures using Hyperspectral Imaging

Hyperspectral imaging encompasses a range of optical techniques in which images with each pixel comprising of a spectrum rather than a RGB colour value. This is advantageous over regular imaging as more quantitative information can be extracted from an image to the extent that hyperspectral imaging techniques have become commonplace in many widely spread fields, including microscopy [198, 199], astrophysics [200], remote sensing and geology [201, 202], food standards [203, 204], and medical imaging [205–207]. Within each of these fields, the features in an image are more clearly identified by their spectral signatures. In this instance, scanning confocal hyperspectral imaging is applied to optically characterise both sharp and nanostructured metallic tips and identify SPRs originating from LSP excitation.¹

Scanning confocal hyperspectral imaging falls under the category of spatially scanned imag-

¹This technique has also been applied to other periodic, extended nanostructures that are not discussed within the context of this thesis.

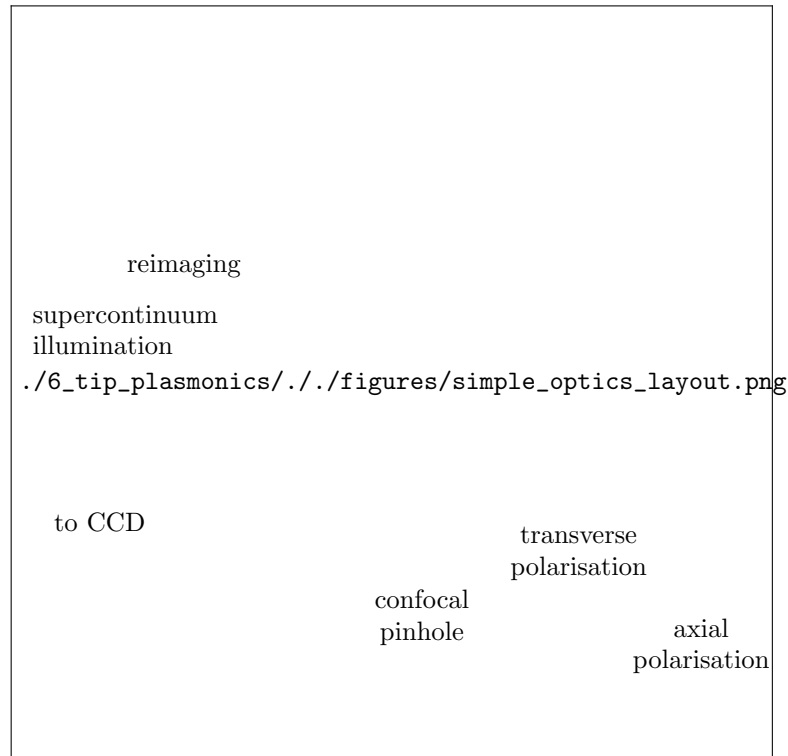


Figure 5.1: Experiment configuration for hyperspectral imaging. The laser is centered on the tip apex for imaging. The tip is scanned across the beam in a grid with spectra acquired at each position. The resulting image then contains 1044 colours at each pixel instead of the usual 3 (RGB).

ing. Tips are scanned in a grid under the laser spot and the spectral content of the confocal sampling volume is measured at each point using a spectrometer instead of a photodiode or CCD. Images are then formed at a given wavelength or across a wavelength band. In this instance, using a bench-top spectrometer, each image pixel is equally digitised into 1044 bins between 400–1200 nm rather than the conventional 3 RGB colour bands. The 0.8 nm wavelength resolution of spectra classifies this procedure as hyperspectral, as opposed to multi-spectral imaging in which images are formed using fewer, much broader, wavelength bands. This approach to hyperspectral imaging has previously been used to identify distributed plasmon modes in aggregated AuNP colloids [49] and to image SPPs [208]. By using this technique in the current microscope configuration, as shown in Figure 5.1, LSPs can be spatially identified with sub-diffraction-limited resolutions around 250–300 nm. Combining it with 80 nm AuNPs also enabled measurement of the microscope PSF and chromatic aberrations, as discussed in chapter 4.2.

Fast image acquisition is made possible by utilising the ultra-high brightness supercontinuum laser source and sensitive, TE-cooled, bench-top spectrometers with 10–20 ms integration times. Image acquisition is limited only by the integration time at each pixel and the ~ 30 ms movement time between pixels. The focal intensity is, on average, $\sim 10^8 \text{ mW cm}^{-2}$, which is below the damage threshold for 50 nm metallic tip coatings. The illumination and collection

configuration is fixed using a preset reference intensity between different samples in order to more quantitatively compare images. Measured spectra of metallic nanostructures are normalised to a spectrum of the same flat metal to show structural effects only, such as plasmons.

While not the fastest or most advanced method of acquiring hyperspectral images, spatial scanning is made efficient when used with a supercontinuum white-light source. Other imaging techniques, categorised under “spectral scanning”, “non-scanning” and “spatio-spectral scanning”, have been developed to more efficiently produce hyperspectral images under specific conditions. Spectral scanning involves wide-field imaging through either a range of bandpass filters [209], a tuneable liquid crystal filter [210, 211] or an etalon [212], which is appropriate if studying large areas or if confocal localisation is not required. Similarly, if the benefits of optical sectioning are not necessary, a single direction line scan over a sample can be performed with an imaging spectrograph (monochromator with CCD) to form a hyperspectral image rather than use a two-dimensional grid scan with single pixel acquisition [198].

Non-scanning or snapshot hyperspectral imaging techniques are more complex than scanning techniques as both spatial and spectral information are acquired in a single measurement without any scanning or dynamic filtering. The main method of achieving this is by using a computed tomography imaging spectrometer (CTIS) [213–216], in which a 2D dispersive grating placed in the Fourier plane splits an image into many separate spectral images projected onto a CCD. Advantages of this approach are much shorter acquisition times but necessitates a higher computational requirement to disentangle the 2D image into a cube with dimensions (x, y, λ) . Spatio-spectro scanning is the most recent technique, developed in 2014, and involves diagonally scanning through the sample data cube where each point along an axis in the spatial image has a different wavelength [217].

Despite the potential improvements gained by using more advanced hyperspectral imaging techniques, spatial point scanning is deemed the most appropriate solution for tip characterisation, if only for simplicity and compatibility with dual-tip gap spectroscopy. Image acquisition is not time-constrained since the microscope platform is stable, resulting in minimal artefacts due to sample motion, and the use of confocal imaging benefits image quality. Portable benchtop spectrometers are already incorporated into the microscope for use in other experiments and are readily accessible, therefore adapting the microscope to enable use of an imaging spectrograph and line scanning would be inconvenient. Spectral scanning is not beneficial at the current magnification due to the relatively small area occupied by the sample in the wide-field image and due to the far superior spectral resolution of spectrometers when compared to imaging through bandpass filters. For these reasons, spatial point scanning is used for characterisation.

./6_tip_plasmonics/./figures/tip_sems.pdf

Figure 5.2: SEM images of sharp and spherical metal tips studied using hyperspectral imaging. Tips are (a) a sharp Au AFM tip, (b) a sharp Pt AFM tip, (c) a NT Au-coated spherical AFM tip and (d) an electrochemically deposited AuNP-on-Pt AFM tip.

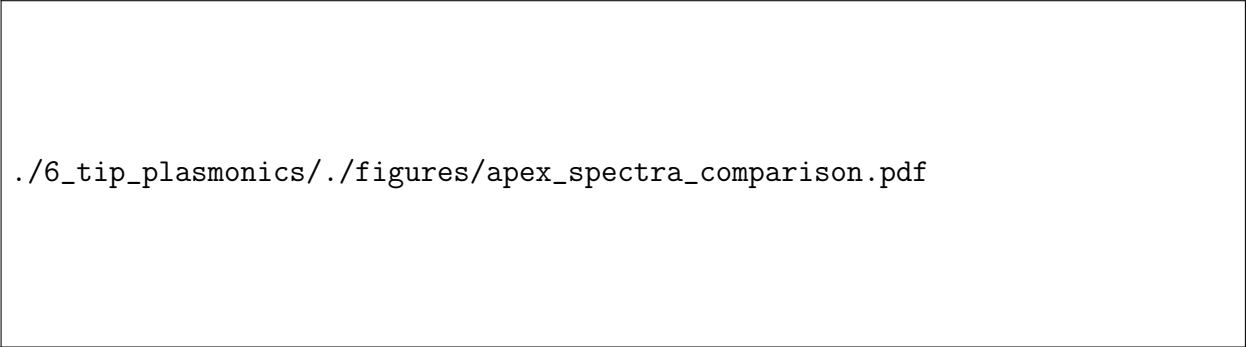
./6_tip_plasmonics/./figures/hyperspectral_tip_comparison.pdf

Figure 5.3: Hyperspectral images of sharp and spherical metal tips at wavelengths of interest. Images are of (a) a sharp Au tip, (b) a sharp Pt tip, (c) a NanoTools Au-coated spherical tip and (d) an electrochemically deposited AuNP-on-Pt tip. Collection polarisation is along the tip axis. Colour maps between slices all have the same normalisation. Scattering from the spherical apex is clearly seen in the hyperspectral images of between 600-700 nm.

5.2 Understanding Plasmons in Spherical Nanoparticle Tips

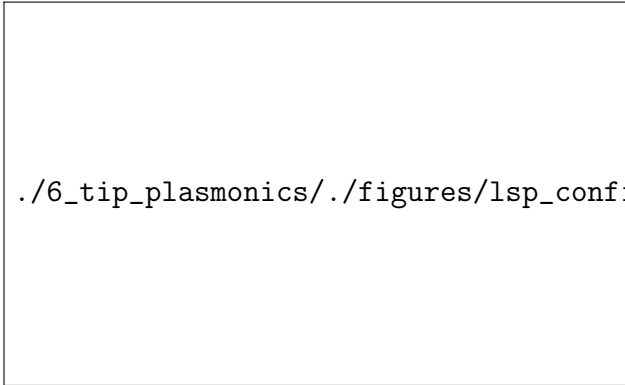
Hyperspectral images are taken of four different types of AFM probes to investigate the plasmonics of nanostructured tips. AFM tips studied are Au- and Pt-coated standard AFM probes (BudgetSensors Au-coated AFM probes), spherical Au tips (300 nm Au-coated NanoTools B150 AFM probes) [14] and AuNP-on-Pt AFM probes, fabricated in-house using electrochemical deposition [218]. SEM images of a selection of these tips are shown in Figure 5.2. Fabricated tips are pre-treated where possible prior to use with piranha solution to remove organic surface residue and, in some cases, smooth surface roughness.

Comparisons between spherical- and sharp-tipped metallic probes using hyperspectral image slices (Figure 5.3) show that spherical Au tips exhibit a characteristic red (600–700 nm) scatter, delocalised from the bulk tip. No similar localised scattering is seen for sharp Au or Pt tips in the visible spectrum, which have an overall weaker optical response. This delocalised



./6_tip_plasmonics/./figures/apex_spectra_comparison.pdf

Figure 5.4: Apex spectra of sharp and spherical metal tips. Spectra are extracted from the hyperspectral images in Fig. 5.3 by integrating pixels around the apex region. A clear resonance at 630 nm is observed with spherical tips in both polarisations. The axial/longitudinal tip resonance is blueshifted 20 nm from the longer transverse resonance. Sharp metallic tips show comparatively flat spectra.



./6_tip_plasmonics/./figures/lsp_confirmation.pdf

Figure 5.5: Integrated inelastic electron fluorescence measurements of both a sharp and spherical Au tip. Fluorescence spectra are acquired using tuneable, single wavelength spectroscopy with integrated spectra plotted as a function of excitation wavelength. The background spectrum is the supercontinuum dark-field scattering spectrum of the spherical Au tip apex, as measured using hyperspectral imaging. Agreement between the fluorescence (near-field) and dark-field scattering (far-field) spectra confirms resonant near-field enhancement as a LSP excitation. Sharp Au tips show no such resonance in either the near-field or far-field.

apex scatter can also be clearly seen in wide-field DF imaging. SEM images confirm that this scatter correlates only with spherical Au tip shapes, or when a AuNP is securely attached at the tip apex with a sufficiently small neck joint.

Spectra of tip apices clearly show a structural resonance excited in spherical Au tips, with no obvious resonances present in sharp tips (Figure 5.4). Scattering resonances around 630 nm are reliably present in all spherical-tipped AFM probes, both vacuum-processed and electrochemically deposited AuNP-on-Pt, and are attributed to direct LSP excitation. The response of sharp Au tips shows no similar plasmonic features while the slow rise in scattering towards the NIR is consistent with lightning rod scattering [116].

Broadband tuneable SERS [219] on each of the tips is used to confirm that the resonance is

indeed a LSP by showing that the internal near-field is resonantly enhanced.² During plasmon excitation both internal and external fields are enhanced. The external field leads to the strong enhancement of Raman spectra whereas inelastic electron scatter inside the surface of the metal is enhanced by the internal field, forming the SERS background [220]. Broadband tuneable SERS is a technique capable of showing both these components [219]. Hence, by integrating the inelastic scattering background at each wavelength the near-field resonance can be calculated.³ SERS background spectra are taken in 10 nm increments of the excitation wavelength.⁴ Integration of the scattering counts for each excitation wavelength shows a distinct peak (Figure 5.5) around the scattering resonance from Figure 5.4, confirming it as a LSP resonance. Further, confirmation stems from direct observation of plasmon coupling between spherical tips, as has been previously reported [14], with results of the latest tip coupling experiments discussed in detail in the next chapter.

Surprisingly, the overall disorder and parasitic edge AuNP nucleation on AuNP-on-Pt only minimally effects the overall optical response from the apex growth. This is likely because the spherical apex already interacts with the base tip structure, regardless of any further deposits. Moreover, the AuNP-on-Pt structure behaves very similar to the Au-coated diamond-like-carbon spherical tip, likely because the 50 nm coating thickness is greater than the skin depth [125, 221]. Plasmons therefore see both as solid Au spheres. Differences arise due to the differences in neck material with Au-Pt and Au-Au neck boundaries.

5.2.1 Interpreting the Spectral Response of Metallic Tips

The plasmon modes of a spherical Au tip are not so different from those of a spherical AuNP and can be explained accordingly. Like AuNP plasmons, spherical tip LSPs are specifically *radiative* antenna-like modes, those that can efficiently couple far-field light into strong collective free electron oscillations without the need for momentum matching due to SPP dispersion. As with AuNPs, the signature of these plasmons is a distinct SPR indicating their large dipole moment. Radiative antenna-like LSPs form only when two close dielectric surfaces surround a metallic particle, allowing the formation of confined multipolar charge oscillations where the geometry modifies the oscillation restoring forces and determines the resonant wavelength [29, 30]. Spherical metal tips retain some of the back hemisphere around the connection to the base tip apex (the neck), allowing the spherical apex surfaces to sustain similar antenna-like plasmons. Sharp tips do not have this back surface, hence cannot support such resonances. Their metal-dielectric surface still, however, supports the launching of SPPs in the near-field if the correct launching conditions are satisfied. This requirement means that while a sharp

²Acquisition of broadband tuneable SERS measurements carried out by A. Lombardi.

³Model of this behaviour is derived in the appendix.

⁴Each acquired background spectrum is shown in the appendix

./6_tip_plasmonics/./figures/spherical_tip_simulations.pdf

Figure 5.6: Numerical simulations of the field enhancement around a spherical Au tip.


(a) Near-field spectra of spherical Au and AuNP-on-Pt tips, extracted from around the apex of the tip. (b) Near-field enhancement distributions of the two resonances highlighted by circles in (a). Simulated tips have a 300 nm spherical radii, 120 nm neck widths, 20° opening angles and 1.88 μm lengths.

tip can in some ways be considered an optical antenna its supported modes are considered as *evanescent* or *near-field* modes rather than *radiative*, limiting its usability.

Numerical simulations of the near-field around spherical tips, computed using BEMAX, are used to show aspects of antenna-like behaviour and can be used to qualitatively describe tips.⁵ Simulated spectra of the near-field around the apices of 300 nm spherical Au and AuNP-on-Pt tips with 120 nm neck diameters and 20° opening angles are shown in Figure 5.6a. Tips are simulated with a length of 1.88 μm to avoid significant truncation artefacts. A neck width of $d_{\text{neck}} = 0.4d_{\text{sphere}}$ (120 nm in this case) is used to match typical experimental structures. Strong modes appear for both tips between 550–700 nm similar to experiments. The peak positions of the strongest resonance in each tip approximately agree with the experimental spectra shown in Figure 5.4a. Near-field maps corresponding to the main resonance in each tip are shown in Figure 5.6b. The near-field at the dominant resonance in the spherical Au tip appears more quadrupole-like with a weaker dipole-like resonance occurring above 700 nm. These are similar to the modes in the AuNP-on-Pt tip except redshifted with different intensities. The 700 nm resonance in the AuNP-on-Pt tip has a more dipole-like structure with a more quadrupole-like resonance at 550 nm.

Spectra can be explained by realising that quadrupolar visible modes are more favourable in larger AuNPs, as found in Mie scattering theory, once dipolar resonances shift out into the NIR. A similarly structured mode to the AuNP quadrupole plasmon would be expected in 300 nm spherical Au tips between 500–600 nm. The neck geometry can potentially short the pole of dipolar plasmons, reducing their confinement, whereas quadrupolar plasmons are much less affected, leading to a more favourable charge distribution and larger SPR. Restoring forces are very different in spherical tips than nanospheres, however, since the neck removes a portion of the back sphere surface and introduces conductive losses, and the tip exiting close

⁵BEMAX simulations carried out by D. O. Sigle.



./6_tip_plasmonics/./figures/neck_size_dependence.pdf

Figure 5.7: Resonant wavelength and field enhancement dependence on the neck width. The resonant wavelength (a) and field enhancement (b) for each of the resonances in spherical Au tips of 250 nm sphere diameter, 1.88 μm length, and 10° opening angle of varying neck widths.

to the rear surface provides a secondary surface for self-interaction. This makes them difficult to analytically describe.

Electromagnetic coupling between Au and Pt surfaces is weaker than the interaction between two Au surfaces [135], hence plasmons in the Au sphere are less redshifted when attached to a Pt tip apex. The non-plasmonic Pt neck region also forms an additional boundary interface to better confine plasmons to the AuNP. Hence, the redshift of AuNP-on-Pt tips is much less pronounced. The dipole-like mode exists nearer to the visible and therefore becomes more favourable than the quadrupole-like mode. Failure to experimentally observe the predicted quadrupole-like mode suggests that either the dipolar mode is a far more energetically favourable charge configuration or that the simulated geometry remains too dissimilar to realistic spherical tips. Nevertheless, simulations provide some insight and qualitative descriptions from which to understand plasmons in spherical metallic tips.

In order to directly compare the *plasmonic* behaviour of spherical Au tips with sharp Au tips independent of the lightning rod contribution the neck width is increased in simulations with spectra extracted as before. In this manner, the structure transitions from a AuNP balanced on the apex of a sharp tip into a typical spherical tip followed by a transition into a rounded tip geometry, similar in shape to a sharp Au tip, without the radius of the tip apex ever changing. **A smaller radius of curvature and opening angle are used to fall between the expected behaviour of both sharp and spherical tips.** The field enhancement and peak positions extracted from the results of this morphology transition are shown in Figure 5.7. Resonances do not appear to be particularly sensitive to neck width until it becomes greater than $0.8d_{\text{sphere}}$ and tips transition into a geometry more similar to sharp tips. This explains the robustness of observed spherical tip plasmons regardless of tip morphology. A steady decrease in the field enhancement, however, is observed once $d_{\text{neck}} > 0.4d_{\text{sphere}}$, decreasing faster once $d_{\text{neck}} > 0.8d_{\text{sphere}}$. This supports the claim that sharp tips lack a back surface on which to

sustain antenna-like LSPs.

5.2.2 Implications of Spherical Metallic Tip Plasmonics

The previously presented results demonstrate that it is important to consider what plasmons might exist in a particular nanostructure geometry under certain illumination and collection conditions, and that it is beneficial to characterise nanostructures before applying them in any further techniques. Without prior knowledge as to where in the visible spectrum specific plasmons are excited it is difficult to properly interpret any further results, such as TERS spectra. Improved tip characterisation is crucial to understanding why such varied TERS enhancements are reported. Additional thought must also be given to the optical method of characterisation. Confocal hyperspectral imaging is capable of mapping the local scattering response due to use of a pinhole for localisation. Broadband tuneable SERS also offers a unique way of characterising the near-field. Basic microscopy alone is a not particularly effective method for measuring the apex response of a tip and thus techniques similar to those described in this chapter should be used and developed where and when possible.

Utilising spherical tips not only exploits visible LSPs but also permits the use of a wider range of illumination configurations as the restriction to evanescent coupling is lifted. Regardless of plasmonics, the lightning rod effect will always play a role in the near-field enhancement process, giving sharp tips an initial advantage, but with careful optimisation of the spherical tip geometry, tips can be brought into resonance with one of the plasmons to maximise enhancement. Spherical Au tips in their current form are already quite well optimised for TERS due to being on resonance with the readily available HeNe wavelength.

Plasmons in spherical tips have also been shown to readily couple with plasmons in other spherical tips [14] and would be expected to couple with image charges in a planar mirror, thus significantly increasing their near-field enhancement. In this situation, their resonances can be tracked as the tip approaches the surface and stopped on resonance with the incident TERS laser for maximum enhancement, for example at the common 785 nm excitation wavelength. For small gaps on the nanometre level, the plasmon mode will become strongly confined to the gap and its contribution to the near-field should outweigh the lightning rod effect. Exploiting the radiative plasmons in nanostructured tips in this manner bridges the gap between the plasmonics involved in SERS and TERS. Some of the largest enhancement factors recently measured in plasmonic systems originate from radiative plasmons in AuNPs coupled with the charge distribution of their image in a mirror [42, 43]. These systems repeatedly produce Raman enhancements of up to 10^7 , much like tips, with nanometric mode volumes of coupled plasmons. This demonstrates that plasmonic gaps can exhibit large field enhancement without requiring a significant contribution from the lightning rod effect. However, the static nature of the NPoM geometry lacks the ability to chemically map a surface. By coupling plasmons

in spherical tips with their mirror charge, surfaces could be dynamically mapped with a potentially very large field enhancement.

This discussion on single tip plasmonics is concluded by performing one measurement specifically relevant to TENOM. To demonstrate the advantages of having prior knowledge of excited plasmons in tips, along with the advantages of using AuNP-on-Pt tips, a TERS measurement is performed directly after characterisation on resonance with a plasmon.

5.3 Improved Field Enhancement of Spherical Au Nanoparticle Tips

A result of spherical Au tips sustaining SPRs which couple with the far-field is that their plasmonic contribution to the field enhancement can outperform the lightning rod contribution in sharp tips (assuming no near-field plasmonic excitation in sharp tips). The field enhancements for both sharp and spherical Au tips, more specifically the fabricated AuNP-on-Pt tips, are determined in a side illumination configuration by using Raman scattering.

SDF spectroscopy is used in conjunction with Raman spectroscopy in a modified version of the microscope platform, enabling both techniques (though not simultaneously). Fabricated AuNP AFM tips are mounted opposite a benzenethiol-coated sharp Au AFM tip in a tip-to-tip configuration, mimicking a plasmonic bow-tie antenna (Figure 5.8). This configuration is used to obtain good optical access to the intertip gap for spectroscopically probing its plasmonic properties. Benzenethiol (BTh) is used as a Raman marker for measuring the relative field enhancement of AuNP tips due to its strong Raman response and well-known spectra [172,

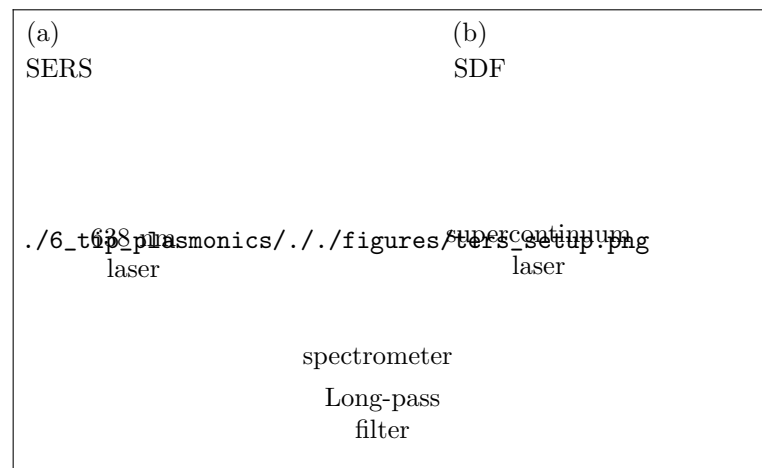


Figure 5.8: Experimental geometry for dark-field spectroscopy and SERS measurements. A 125 nm radius spherical AuNP grown onto a Pt-coated AFM tip is spectroscopically studied using a supercontinuum laser in a dark-field configuration. The tip is then brought within 1 nm of a benzenethiol-coated sharp Au tip under 638 nm illumination to measure SERS spectra.

222]. BTh (VWR International Thiophenol for synthesis) is diluted to 5 mM solutions in ethanol (Sigma-Aldrich). A standard Au-coated AFM tip, for use as a SERS substrate, is prepared by coating a monolayer of BTh onto the surface. This is achieved by submerging it in 100 mM ethanolic BTh solution for 1 min followed by rinsing with ethanol and drying in nitrogen. This is repeated 5 times to ensure complete monolayer coverage. Tips used as plasmonic probes are not coated in BTh.

With the BTh tip retracted, a SDF apex scattering spectrum of the enhancing tip is acquired. After characterisation the microscope optics are modified into a TERS configuration and the enhancing tip is aligned to the BTh tip using the capacitive alignment technique described in chapter 4.5.⁶ Once aligned, the gap size is reduced to ~ 1 nm, limited by the thickness of the assembled BTh molecular layer, and illuminated through a 100×0.9 NA visible objective with 3 mW (1.9 MW cm^{-2}) of 638 nm laser light incident on the gap, polarised along the tip axis. Scattered light is collected through the same objective and confocally localised. Raman spectra are filtered using a 650 nm long-pass filter (Chroma) prior to dispersion in a spectrometer. Contact dynamics, measured using AFM, confirm that tips come into physical contact while separated by a BTh layer.

Near-field calculations for the spherical Au tip are computed for comparison with experimental results and to understand the enhancement mechanism. The near-field distribution at 633 nm and the spectrum 1 nm from the apex are calculated using the full electrodynamic boundary-element method [223, 224].⁷ The spherical tip is modelled as a Pt cone with half-angle 20° with a 250 nm diameter AuNP attached to its end. The neck diameter between sphere and tip is 100 nm. The tip is illuminated with a plane wave polarised along the tip axis.

A 250 nm diameter spherical AuNP-on-Pt tip, grown as described in chapter 3.2 (-8 V, 150 ms exposure), is used to demonstrate the augmented plasmonic properties of spherically nanostructured tips. Raman spectra of BTh molecules in the tip dimer gap are greatly enhanced when using a AuNP tip in place of a sharp Au tip (Figure 5.9a). As the same spectrometer is used for both broadband scattering spectra and SERS spectra, its restricted spectral resolution (300–1100 nm bandwidth), combined with the broadness of the diode laser line illumination, blurs the characteristic multiple Raman peaks of BTh between $1000\text{--}1600 \text{ cm}^{-1}$. However the resulting observation of two broad peaks in this region affirms the presence of BTh in the gap between tips. The background signal is also enhanced across a broad bandwidth, as is typical for SERS [222].

SDF scattering spectra (Figure 5.9b), taken of individual tips prior to SERS measurements, show that the increased Raman enhancement when using a AuNP tip is due to excitation of a LSP around 630 nm, not present in sharp Au tips. This is in good agreement with boundary

⁶The optics are modified in the sense that the laser input is switched and the dark-field iris is opened.

⁷Near-field calculations carried out by Lars O. Herrmann.

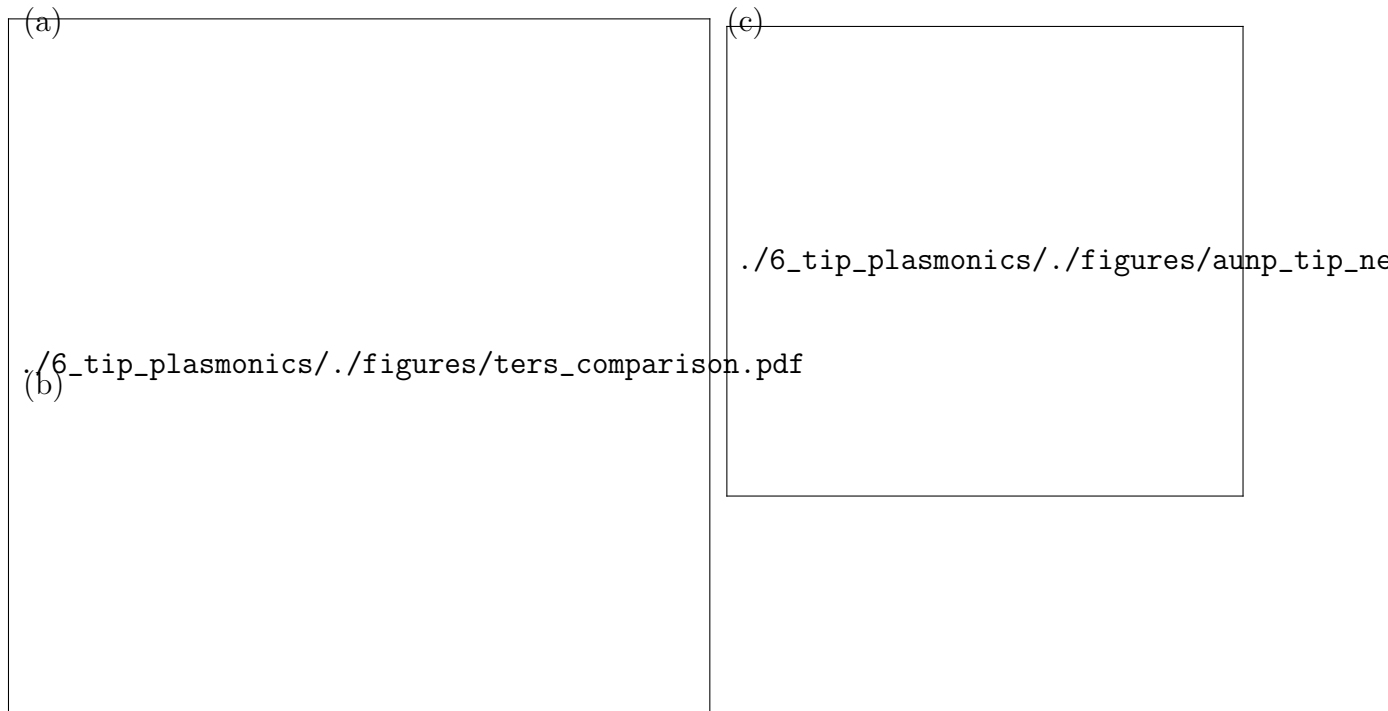


Figure 5.9: Application of sharp Au and AuNP-on-Pt tips to enhancing Raman scattering. (a,b) Comparative TERS and dark-field spectroscopy of sharp Au and AuNP tips. (a) Tip-enhanced Raman spectra of a benzenethiol-coated Au AFM probe brought close to the AuNP tip (red), compared to a sharp Au AFM tip (blue). (b) Dark-field optical scattering of AuNP (red) and sharp Au (blue) AFM tips, with calculated relative intensity enhancement 0.5 nm from the AuNP tip apex (dashed). The inset shows an SEM image of the 250 nm AuNP tip. (c) Calculated field enhancement profile for a 250 nm diameter AuNP at the end of a 1500 nm long Pt tip. The neck join is 50 nm wide and the tip is under longitudinally polarised plane wave illumination at 633 nm.

element calculations of the near-field enhancement at the AuNP tip apex with a visible plasmon resonance observed across the AuNP (Figure 5.9b,c). Coupling between this LSP in the AuNP tip with a BTh-coated sharp Au tip forms a confined gap plasmon mode. Since coupling is between higher order modes in the sharp Au tip, shifting of this resonance as a function of gap size is weak [134, 225]. Illuminating on resonance with the AuNP tip plasmon therefore greatly increases the Raman response by $30\times$ when compared with the sharp Au tip Raman response. This corresponds to a relative SERS enhancement of 12 after taking into account the confinement and mode volume of a LSP to the gap in each case [55].

LSP mode volumes are estimated using a cylindrical gap mode model. The lateral width of a gap plasmon mode is calculated using $w = \sqrt{R_{\text{eff}}d}$, where R_{eff} is the effective radius of the particles, $\sqrt{R_1R_2}$, comprising the plasmonic dimer and d is the width of the gap separating particles [55].⁸ This results in lateral mode widths of 4.5 nm for the sharp Au tip of 20 nm radius and 7.1 nm for the 125 nm radius AuNP tip.⁹ Assuming a cylindrical gap mode yields

⁸The use of $R_{\text{eff}} = \sqrt{R_1R_2}$ is justified by...

⁹Note that these widths are below the quantum limit for such large AuNPs, presented in [14], only because

mode volumes of 15.7 nm^3 and 39.3 nm^3 , respectively. These define the near-field contribution to Raman scattering and a relative field enhancement is obtained using, where N is the Raman signal counts and V is the mode volume. This evaluates to 12. Since the LSP is laterally confined to only 7 nm within this gap the enhanced Raman signal is the result of scattering contributions from only a very small number of molecules. Lower limit absolute Raman enhancements are estimated using, where N_{ff} , the number of counts obtained using only far-field laser light, is assumed to be 0.1 counts/s/mW from the noise levels since signals are below the signal to noise level and V_{ff} is assumed to be $25\,000 \text{ nm}^3$ based upon the surface of a conical tip exposed to the focal volume of a diffraction limited spot ($d = 412 \text{ nm}$ at $\lambda = 638 \text{ nm}$). This expression yields absolute, lower-bound field enhancements of 1.9×10^5 for a 250 nm AuNP tip and 1.6×10^4 for a sharp Au tip. Though absolute estimates are not as high as expected, the relative SERS enhancement observed with the AuNP tip is indeed comparable to previously reported results [153].

These optical measurements confirm that AuNP tips provide increased field enhancement compared to sharp Au tips due to a strong LSP excitation. Lack of any strong peaks around 600 nm in dark-field spectra of sharp Au tips suggests that any plasmons present are weakly coupled and do not scatter strongly in this illumination geometry. Such plasmons may still couple with the opposing tip to form a gap mode but reduced scattering efficiency results in a lower observed field enhancement. On the other hand, AuNP tips are well suited to high enhancements when illuminated at the appropriate plasmonic resonances. Whilst a number of plasmonic probes have been developed recently, several useful features are obtained here. By using standard AFM probes as a basis, these AuNP tips maintain their functionality as AFM probes for force microscopy. The metallic coating of these tips also allows for simultaneous electrical measurements whilst performing optical and AFM force measurements. These tips therefore function as standard electrical AFM probes with added plasmonic functionality. Furthermore, such tips also show excellent resistance to damage at the tip apex after multiple surface contacts, though surfaces do become deformed after heavy use. Their robust nature is attributed to the direct growth of the AuNP root across the pyramidal tip end. This is a significant improvement over currently-available commercial spherical AFM tips, in which the spheres break from the tip and adhere to the contact surface after only one or a small number of contact cycles. Further applications of spherical metallic tips can be envisaged, for instance in plasmonic optical trapping [44] because the tips in the present geometry can conveniently act as a heat sink reducing the problematic optical heating observed, and resulting thermal damage.

the opposing tip has such a small radius to increase localisation.

5.4 Conclusions

Within this chapter it has been shown that spherical AuNP-tipped AFM probes are capable of supporting radiative LSPs in the red part of the visible spectrum that are not supported by the more conventional, sharp Au tips. These plasmons are clearly observed to exist at the apex of extended tip microstructures using scanning confocal hyperspectral imaging in the SDF microscope platform to locally probe the optical response. Broadband tuneable SERS is used to further confirm plasmonic behaviour in spherical Au tips. These techniques are ones that enables plasmon-dependent applications, such as TERS, to pre-screen nanostructured tips to better improve their reliability and reproducibility. The development of antenna-like plasmons in tips through nanostructuring, which readily couple to light without the need for momentum matching, is a step forward for TENOM. Furthermore, these modes determine what plasmonic phenomena are able to be experimentally observed, hence spherical tips can be used to dynamically investigate plasmonics.

The final set of experiments discussed in this thesis are the product of each of the developments from the previous chapters, utilising pairs of tips in the microscope platform to investigate the limits of plasmon coupling. Coupling between different tip morphologies is dynamically investigated to both confirm plasmonic behaviour in tips and increase understanding of the characteristic regimes of plasmon coupling. Through this work an improved interpretation of future results in sub-nm plasmonic gaps can be attained, along with insight into the mechanisms by which TENOM operates.

6.1 Non-Optical Experimental Measurements of Dynamic Tip Dimers

Dynamic interactions and separation-dependent phenomena between two tips are spectroscopically studied using an axial scanning approach. Tips are coupled with another tip in order to maximise optical accessibility to the gap. Although not representing the typical geometry used in TENOM it presents a more optimum geometry to explore plasmonic coupling on a more fundamental level. Tips are first aligned into the dimer configuration under the supercontinuum laser beam using the capacitive technique described in chapter 4.5. Alignment takes place with the laser illumination on to prevent spatial changes of the tip apices, caused by thermal expansion, from occurring post-alignment when spectroscopy is performed.¹ The tip of the harder cantilever of the pair is partially positioned in the laser spot and the tip of the softer cantilever is resonantly driven and used as the alignment probe, beginning at distances outside of the laser focus. Sufficient space is ideally left after placement of the stationary tip to accommodate both tip apices equally under the laser spot once brought together. This level of positioning is subjective, with scattering intensity used to estimate an acceptable position

¹This behaviour was briefly looked at, with laser-induced cantilever deflection being measured in tips. This suggested that the heat of the focus was causing mechanical deforming or bending of the AFM probe, moving the lateral position of the tip apex and misaligning the tip dimer prior to gap coupling experiments. As such, it could be a source of error in experiments that was necessary to consider.

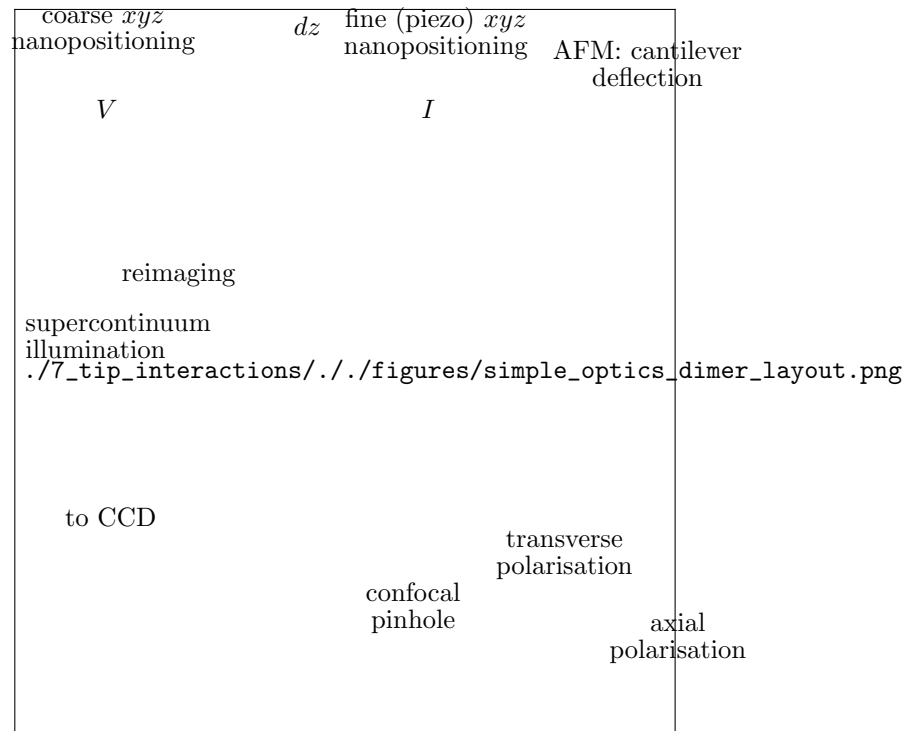


Figure 6.1: Experiment configuration for axial tip scanning. The laser is centred on the aligned tip dimer for gap spectroscopy. The soft cantilever approaches the stationary, stiff cantilever at a rate $dz \text{ nm s}^{-1}$. A bias is applied across the tip junction and the current through the gap is measured. The soft cantilever faces the AFM module for force measurement via cantilever deflection.

for the stationary tip within the collection spot. Once alignment is complete the separation between tips is reduced from around $\sim 300\text{--}500 \text{ nm}$ to geometrical contact whilst undergoing measurement.

The tips used in experiments, whether commercial or fabricated in-house, are required to have clean metallic surfaces when studying gap plasmon interactions. Layers of insulating chemicals only prevent the gap from narrowing sufficiently to enter the tunnelling regime. Any layers deposited as either a byproduct of a chemical reaction or carbon deposition in SEM need to be removed. This is done through either plasma cleaning or piranha treatment. To maintain cleanliness some experiments are performed in a nitrogen flow environment.

During scanning measurements on tip dimers, the stationary tip acts as the optical probe, staying fixed in the collection spot throughout the scan, whilst the other tip approaches at a rate of $0.1\text{--}1 \text{ nm s}^{-1}$. Approach speeds are continually adjusted and optimised during scanning to reduce the time interval between completion of alignment and achieving geometrical contact and minimise any potential lateral drift. Use of a stiffer cantilever ensures that the AFM tip remains fixed in its current position under the laser spot, even when under pressure from the opposite tip. Measurements of the optical scattering, electronic conductance and applied force are taken at each point in the scan. The geometry of this experiment is shown in Figure 6.1.

The approaching tip perturbs the near-field and interacts with the probe tip. Separation-dependent optical scattering is then collected through the objective collection aperture. Strong scattering of the intense supercontinuum source means 10–20 ms integration times are sufficient for a high quality signal to noise, therefore spectra acquisition does not affect the scan speed. Only light polarised along the tip dimer axis is studied in the context of this work in order to focus on the influence of charge transfer on bonding hybridised plasmons.

Simultaneous measurement of gap conductance and applied force supplement optical scattering measurements, enabling correlations to be made between characteristic gap properties.² This is done to better support hypotheses regarding the relationship between charge transfer and plasmonic coupling. Electronic properties are probed by driving with a d.c. voltage and measuring the current through the tip junction to determine its conductivity. A bias of 50 mV is almost always used to achieve good signal quality in both the low-bandwidth and high-bandwidth conductance measurements and to prevent spikes in the noise from setting off the high-bandwidth trigger. Larger voltages increase the electrostatic pull between tips, visible in force measurements, and the resulting high current upon contact would damage tips if not for the current limited resistor, instead limiting the maximum measurable conductance. The current range is limited to above 10 nA, with a sensitivity of 10 fA, as lesser ranges require longer settling times, slowing the scan rate. At 50 mV the smallest measurable conductance is $\mathcal{O}(10^{-7}G_0)$.

The applied force is measured using optical detection of cantilever deflection by the AFM module. At each step in the scan the position of the returning laser beam is averaged for 100 ms to determine the mean cantilever deflection, and therefore the mean applied force, over the duration of electronics and optics measurements. Using this combination of measurements allows for a more informed interpretation of nanoscale gap behaviour than by measuring only the optical scattering, as was done originally [14].

6.1.1 General Properties of a Nano-Tip Dimer Gap

Before studying the optical properties of nano-gaps it is beneficial to understand the range of physical phenomena that exist on each characteristic length scale present during scans that traverse from ~ 100 nm to 0.1 nm. With tips well separated, both the separation and the optical scattering are the only meaningful physical quantities. The optical scattering, if plasmonic in origin, is subject to a separation-dependent capacitive interaction. There is no current and no applied force until the separation reduces to below $\mathcal{O}(10$ nm). Below this point both the current and the force become instrumental in understanding the optical response. Due to the

²Each measurement is ran in parallel using multiprocessing in the experiment control method, with each taking a fixed amount of acquisition time. Multiprocessing not only allows data to be acquired around the same time but also decreases the overall measurement time.

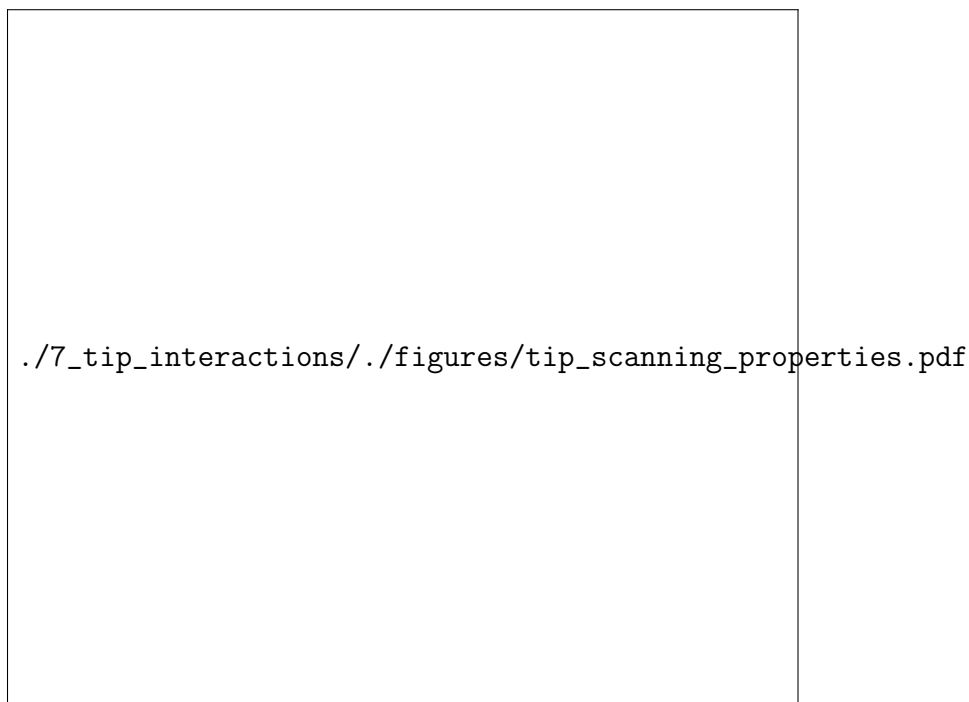


Figure 6.2: Axial force and conductance measurements of a sharp Au tip dimer approaching into contact. The characteristic AFM snap-in effect is seen in the axial force (a) as a discontinuous jump before the linear application of force in a soft contact regime. The tip apices snap together, reducing the separation to on the order of 1 nm, leading to the onset of quantum tunnelling, and finally conductive contact, upon further decreasing the gap separation (b). Dashed and dotted lines are added as guides to the eye showing different features in the scan, such as snap-in and conductance behaviour.

maturity of AFM, STM and molecular electronics there is already a wealth of information explaining both electronic effects and the forces expected on these lengths.

Figure 6.2 shows the conductance and axial force measurements from a typical scan once separation has passed below 10 nm. The force shows no features until there is a fast negative (attractive) jump in the applied force, showing that the tip has been pulled towards the opposing tip (Figure 6.2a). The lack of a tunnelling current at this point shows that the tip has not yet closely approached the opposite tip and must still be separated by more than 1 nm. This is the signature of water in gap. The actual extent of these snaps varies between scans depending on a number of factors, including the humidity, with some scans snapping in closer than 1 nm as inferred from rising tunnelling currents.

Since experiments are carried out in ambient conditions the surfaces of tips will always be coated in a thin film of water or nanobubbles. Even in a nitrogen environment, its presence is only reduced and not completely removed.. When two surfaces come into close proximity a water meniscus forms between them, leading to strong capillary forces [226]. Hence, when the separation between the two tips reduces past the point of meniscus formation they are quickly pulled together [227]. This is known in AFM literature as the “snap-in” or “snap-into-contact”

and occurs on separations $\sim 5\text{--}30\text{ nm}$ [227, 228]. In the above scan the snap distance can be inferred from the force as 6 nm since this is the amount of approach required to remove the applied force.

To prevent snap-in either a stiffer cantilever must be used (normally in tapping mode) [229] or the water meniscus has to be removed, which is usually achieved through liquid immersion AFM [228, 230, 231]. Removal of the meniscus can also be realised by using plasma treatment to remove hydrophobic contamination [228]. In this instance, however, the water layer is advantageous. The presence of the meniscus prevents immediate electrical and geometrical contact and holds tips around 1 nm apart until further force is applied. Approach of the tips then occurs in much finer increments due to resistance from the water. This effectively splits a scan into three regimes - one in which the piezo displacement corresponds directly to the separation decrease between tips, one after snap-in in which increased displacement neutralises the capillary force and pushes the tip through the water meniscus (soft interaction), and finally one in which force is applied directly to the opposite tip in geometrical contact (hard-wall contact).

The existence of the soft interaction regime enables sub-nm gaps to be studied with some degree of control since only a fraction of the applied cantilever displacement corresponds to a displacement of the apex. Instead, the meniscus is loaded with the applied force leading to the linear reverse deflection observed in AFM force measurements. This can be seen in Figure 6.2 where 15 nm of cantilever displacement moves the apex $\sim 0.8\text{--}0.9\text{ nm}$ (deduced from electron tunnelling measurements). The remaining 14.2 nm loads the gap with an applied force of 8 nN , proportional to the cantilever's spring constant.

Use of soft AFM probes (contact mode cantilevers) means a greater spatial resolution in the sub-nm regime since the force required to push through the meniscus is applied more gently for the same size step in cantilever displacement.³ Softer cantilevers are also advantageous during tip alignment as they have larger oscillation amplitudes, and therefore lower voltages needed to reach acceptable signal quality, and also lower bandwidth requirements (13 kHz as opposed to $190\text{--}300\text{ kHz}$). For these reasons, along with those directly related to tip alignment capabilities (outlined in chapter 4.5), one tip in the dimer is usually a contact mode probe while the other tip, which must remain stationary under an applied force, is a stiffer tapping mode probe. Early experiments exclusively used contact mode cantilevers until determining that spectral changes could not be guaranteed to originate from the gap under the application of a large force.

Despite their usefulness in showing the relative motion of the tip, force measurements are somewhat limited in their information on the absolute separation. An estimate of the absolute separation is made possible by studying charge transfer in the gap. Electron tunnelling is the

³Smaller k means larger x required for $F = kx$ to meet the same target value.

dominant charge transfer mechanism, occurring prior to geometrical (classically conductive) contact. Multiple mathematical descriptions of this phenomena exist[75, 76], especially after the invention of STM, that predict the conductance and resulting current density as electrons tunnel through an arbitrary potential landscape. In most models, tunnelling current densities are approximated using [84], where d is the barrier width, J_0 is the saturation current density at $d = 0$ and β is a decay constant based on the barrier potentials and electrode work functions. In this form, the current due to tunnelling follows an approximately exponential decay with increasing separation. The current in STM is often stated to drop by a factor 10 for every 1 Å (0.1 nm) away from geometrical contact. This relation permits deduction of the gap separation to a certain degree using the order of magnitude of the gap conductance.

Upon reducing the gap to below 1 nm electron tunnelling becomes detectable. Though the absolute value of the conductance for a given separation depends on the gap morphology the relative exponential conductance drop from geometrical contact still approximately holds for $d > 2$ Å [74]. This makes electron tunnelling a useful method for estimating the gap size to within ~ 0.1 nm, as is done in STM, though the technique is limited to sub-nm separations. Once the separation is greater than 1 nm the conductance drops to below around $10^{-9}G_0$ and the corresponding current becomes difficult to measure without significantly raising the d.c. bias. For example, use of a large bias of 50 mV still means a current on the order of 1 fA, which remains below the currently achievable noise level.

Figure 6.2b shows a typical conductance trace on approach. Once the separation decreases below 1 nm the conductance steadily increases with force from 10^{-7} to around $10^{-4}G_0$ as the tips transition through the soft interaction regime. At $10^{-4}G_0$ (0.4–0.5 nm), the rate of conductance increase slows, signifying a second more resistance gap layer and requiring a greater force to break through. At $10^{-2}G_0$ (~ 0.3 –0.4 nm) the final layer is displaced and tips quickly transition into geometrical contact, saturating with a contact conductance around $100G_0$. The displacement of layer and consequent relief of force on the tip is shown by the decrease in gradient during the transition into contact.

Each of the electronic and force measurements described in this section are instrumental in discerning the underlying phenomena occurring in sub-nm gaps. These measurements can then be correlated with optical spectra and used to interpret changes to plasmon coupling, especially changes that depend sensitively on gap morphology or dielectric medium. Using this information, more accurate physical models can be developed to further understand the quantum regime of plasmon coupling than what currently exist.

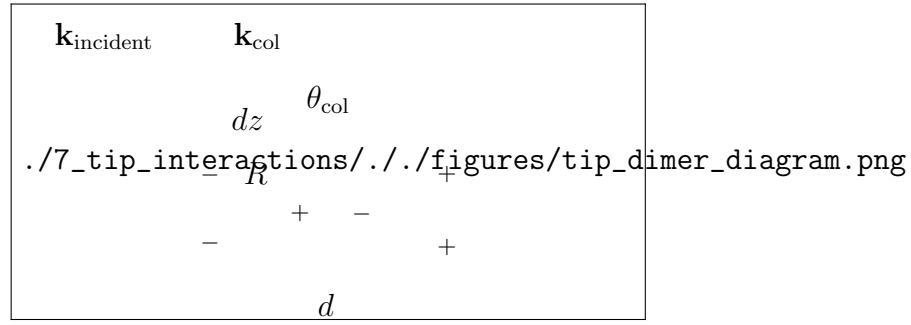


Figure 6.3: Diagram of tip dimer characteristics. The diagram specifically shows the case for a spherical Au tip dimer, showing the antenna plasmon modes which couple together. Plasmonic coupling depends on both the gap size, d , and the particle radius, R , where the mobile tip particle approaches a stationary spherical tip at a rate dz . The illumination and collection angles, defining $\mathbf{k}_{\text{incident}}$ and \mathbf{k}_{col} , are $\theta_{\text{incident}} = \sin^{-1}(0.6 - 0.8NA)$ and $\theta_{\text{col}} < \sin^{-1}(0.6NA)$.

6.2 Plasmonic Coupling Between Tips

Plasmonic interactions between tips are studied using the dimer approach. Two AFM tips are dynamically brought together to form a single gap structure, mimicking a plasmonic MIM dimer cavity, whilst the optical scattering, conductance and force are simultaneously measured. The resulting experiment geometry is shown in Figure 6.3. Both sharp and spherical Au tips are studied in a range of dimer permutations, in order to understand how plasmons in each tip couple. This is also compared with results from hyperspectral characterisation, indicating whether plasmons initially exist in such structures.

6.2.1 Sharp Tip Dimer Interactions

The first combination of AFM tips studied is a sharp Au tip interacting with another sharp Au tip. Hyperspectral characterisation indicates that sharp Au tips lack any observable SPRs and have no antenna-like modes. Similarly for dimer experiments, no coupling is expected to be observed, despite the possibility that gap modes may exist. Reducing the separation between two sharp Au tips indeed shows no resonances or coupled modes (Figure 6.4). Scattering increases are often observed, however these do not shift with decreased separation or change with conductance. They are instead attributed to more of the reflective tip facet entering the confocal collection aperture as the tip is approached to the stationary tip. The superimposed spectral scattering increase also bears resemblance to the spectral density of the illumination, further supporting this claim. Correlations between the scattering intensity and the torsional force also support this explanation.

Tunnelling currents are observed to have no effect on scattering from the gap, despite reports suggesting that tunnelling electrons excite plasmons [102, 232–236]. The reason for this is the low bias of 50 mV. The excitation requirement of $\hbar\omega < eV$ is not satisfied and

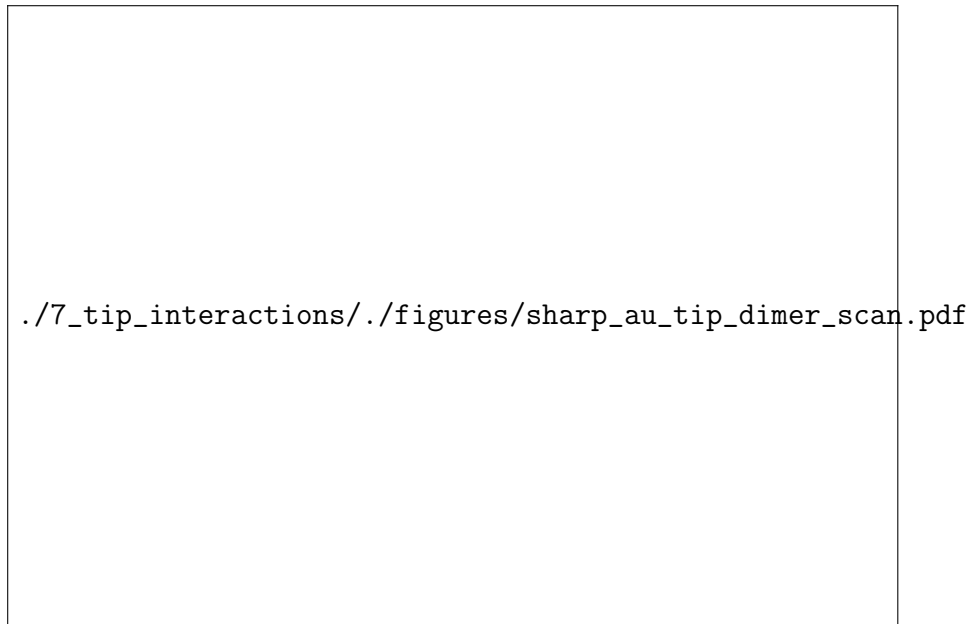


Figure 6.4: Spectra of a sharp Au tip approaching a stationary sharp Au tip. Sharp Au tips are BudgetSensors GB series AFM probes. There are no identifiable plasmon resonances initially in the system and no new modes appear with decreasing gap size. The lack of any shifting suggests that plasmons are not present in the system. The increase in intensity and its spectral shape are an artefact of adding more of the reflective tip facet into the confocal collection aperture.

hence only low energy SPPs in the IR have a possibility for excitation.⁴ Using higher voltages around 2 V would give a finite probability that an electron would excite a SPP, with intensity depending on the current through the junction and the collection geometry.⁵ In the current geometry only localised gap modes could be observed since the system lacks a planar Au surface with an underlying glass medium from which to collect SPP leakage radiation using an $NA > 1$ collection geometry. For tips there is no guarantee that apex localisation should occur and momentum conservation would suggest that SPPs excited at the apex would propagate away. Furthermore, reports detecting radiation from localised gap modes have used sensitive CCDs with 60 s integrations. Hence, within this system, using 10 ms integration times and without a method for SPPs to localise, it is unlikely that tunnelling-induced radiation will be detected.

The conclusions drawn from these experiments agree with those of individual sharp Au tip spectroscopy. Sharp Au tips do not show any evidence of supporting plasmons which readily couple with light and there have been no detected signatures of plasmon coupling between similar tips. However, both the gap geometry and previous spectroscopic (spectroscopy, TERS and electrical excitation) measurements on tips suggest that plasmons and gap modes exist in tip systems. It can only be stated that, based on observations made on the measurements

⁴For a 50 mV voltage the limiting frequency is 7.6×10^{13} rads, or $\lambda = 24.8 \mu\text{m}$ deep in the IR.

⁵For a 2 V voltage the limiting frequency is 3.0×10^{15} rads, or $\lambda = 630 \text{ nm}$. Hence plasmons can be excited in the red region of the visible spectrum and on into the NIR.

shown here, that only antenna-like plasmons can be seen in the far-field and that tips are not capable of supporting these. Sharp tips may, however, support near-field-coupled modes, such as SPPs, which form part of the underlying mechanism of TENOM. Further tests outside the scope of the work discussed in this thesis would be required to test this hypothesis.

In order to optically probe plasmon coupling in a sub-nm cavity between two tips, a tip geometry is required that strongly interacts with far-field light. Sharp Au tips are clearly inadequate for this purpose. For this reason the spherical tip geometry, with its visible wavelength SPRs, facilitates the dynamic study of plasmonic coupling in nanoscopic gaps.

6.2.2 Spherical Tip Dimer Interactions

By using spherical Au tips the tip-tip system mimics the prototypical spherical AuNP dimer. It is through this arrangement that a dynamically controllable plasmonic dimer is recreated. The presence of far-field-coupled, antenna-like plasmons, discussed in 5, enables the detection of gap modes as tips transition from the non-interacting regime at ~ 300 nm through into the charge transfer regime at or before conductive contact. By utilising such a controllable plasmonic system, nanoscale plasmon coupling can be better understood on a fundamental level and unravel the remaining questions regarding plasmonics in sub-nm gaps.

Spherical Tip Interactions with a Spherical Tip

The first configuration of spherical tips studied is that of a spherical Au tip approaching another spherical Au tip. In this instance the 600–650 nm SPRs of the individual tips interact and form observable hybridised gap modes. Representative scans of two approaching spherical Au tips are shown in Figure 6.5, in which SPRs are dynamically followed from non-interacting to classically hybridised. It should be noted that in previous microscope designs the short-range tip alignment meant that SPRs were only observed once coupled at 750 nm [14]. Improvements to the range of the tip alignment technique using optical detection have allowed the full range of plasmon coupling to be studied.

Coupling between spherical tips appears very similar to that of a large nanoparticle dimer. Plasmons are initially uncoupled and only the single SPR of the probed tip is observed. Plasmons begin to interact at $d \approx R_{\text{tip}} = 150$ nm as is classically expected, where d is estimated based on the point of snap-in. As the gap width decreases the individual plasmon modes hybridise, redshifting monotonically and scattering increasingly. Increased scattering is due to both increasing coupling and an increased amount of scattering metal entering the confocal sampling volume of the objective. Once the gap has decreased sufficiently ($d \ll R_{\text{tip}}$) the confocal collection argument is negligible as the sampling volume becomes saturated, hence all further changes are due to plasmon coupling in the gap.

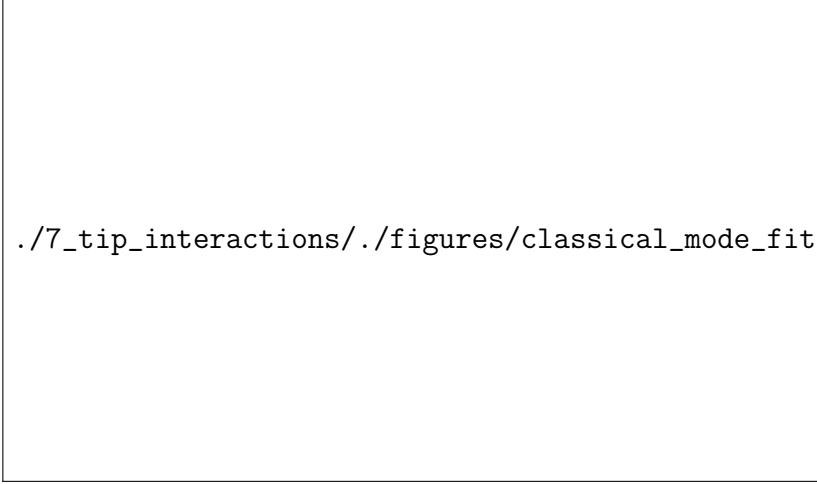


Figure 6.5: Spectra of a spherical Au tip approaching a stationary spherical Au tip. Spherical Au tips are Au-coated NanoTools B150 AFM probes. Two scans are presented in the classical interaction regime, showing similar phenomena. In both cases, but moreso in (b) with tips having similar initial SPRs, bonding hybridised modes form, which redshift with decreasing intertip separation (increasing coupling). With slightly dissimilar initial SPRs anti-bonding hybridisation can be seen as a blueshifting mode with decreasing intertip separation.

For large distances the rate of redshift is dominated by the increase in capacitive coupling as the separation decreases. In each scan a large abrupt redshift of the coupled mode correlates with the snap-in effect measured via the AFM. The large redshift on snap-in is due in part to two effects: the decrease in separation as the tip is pulled in by capillary forces and the increase in refractive index as the gap constitution transitions from air to water (and any organic contaminants pulled into the water meniscus). The intensity of the lowest order mode begins to decrease once the gap width decreases below 1 nm. This effect is attributed to the mode becoming confined to such a degree that it's becoming non-radiative. Similar changes in mode intensity are often seen in classical simulations and occur well before the onset of any significant quantum effects [14, 74]. From theory it has been seen that the field enhancement in the gap continues to increase despite the intensity decrease, confirming that the gap mode still exists but with lower radiative emission, caused by increased charge localisation [69].⁶

Slightly different classical coupling physics is observed when the dimer symmetry is broken. In some cases where initial tip SPRs differ by ~ 50 nm plasmon coupling is better described by a heterodimer model rather than a homodimer. Under the asymmetrical condition, anti-bonding modes are no longer dark since dipoles do not exactly cancel. Depending on which

⁶Increased charge localisation reduces the effective dipole moment of the plasmon mode and therefore the scattering cross section.



./7_tip_interactions/./figures/classical_mode_fits.pdf

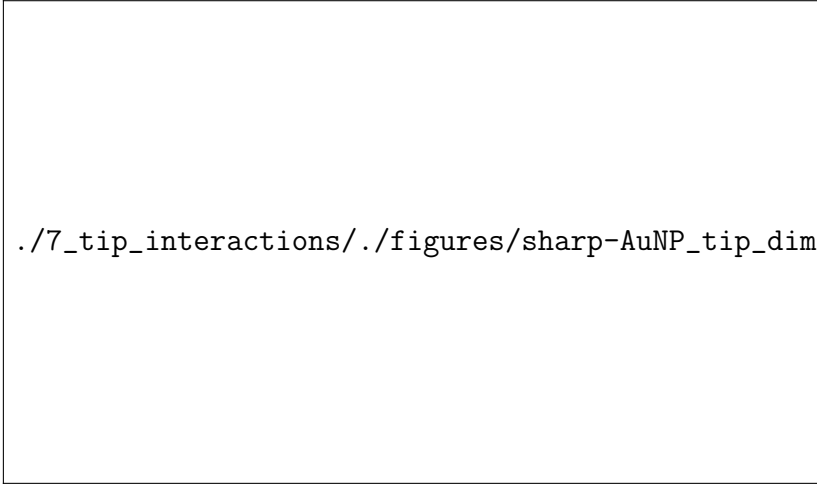
Figure 6.6: LSP resonance wavelengths and amplitudes over multiple scans of spherical tip dimers. The antisymmetric nature of the system mimics a heterodimer leading to the observation of both bonding (red) and anti-bonding (blue) hybridised modes.

particle is probed, either the one supporting the lower or higher energy initial resonance, either a redshifting bonding mode or a blueshifting anti-bonding mode is observed to be the dominant gap resonance (see Figure 2.9 and [64]). The tip dimer probed in Figure 6.5a clearly exhibits both mode configurations. These two types of hybridised modes are additionally seen together across many different scans, for which a subset of resonances traced through measurements prior to snap-in are shown in Figure 6.6. The amount of shift visible in the figure depends on the initial resonance position and the separation at which snap-in occurred.

This effect has been documented previously [64] but never directly observed dynamically. The anti-bonding configuration is typically non-physical in most plasmonic systems since both particles are driven with the same phase of light. However, with larger particles, such as these 150 nm radius spherical tips, the phase symmetry is broken allowing anti-bonding hybridised plasmons to be excited. Both the blueshift and the redshift at small separations are found in spherical tip scans, indicating the interaction and anti-crossing between the lower order anti-bonding mode and the higher order, adjacent bonding mode. The higher order bonding modes responsible for this are then seen after snap-in.

Spherical Tip Interactions with a Sharp Tip

The interaction between the same spherical Au tip and a sharp Au tip is investigated. The results are shown in Figure 6.7. Despite the sharp tip perturbing the field around the spherical tip, acting as the optical antenna, no changes are observed in the spherical tip plasmon, suggesting that there is no interaction between sharp tips and spherical tip plasmons. This is in agreement with predictions that a sharp tip should not deviate the resonance of a planar surface [134, 225], for which the much larger tip could be considered. The tip acts as a



./7_tip_interactions/./figures/sharp-AuNP_tip_dimer.pdf

Figure 6.7: Spectra of a spherical Au tip approaching a stationary sharp Au tip. No coupling phenomena are observed due to the mismatch between localised surface plasmon modes.

point perturbation not strong enough to significantly modify the more distributed antenna-like response. This observation also supports the measurements shown in chapter 5.3, where the laser was assumed to stay on resonance with the AuNP tip as it approached the BTh-coated sharp Au tip.

6.3 Quantum Effects in Sub-nm Gaps between Spherical-Tipped AFM Probes

Should the surfaces of two approaching spherical surfaces be sufficiently clean that the formation of a sub-nm gap becomes possible, the influence of quantum effects on plasmonic coupling becomes readily observable. By monitoring the electrical conductivity simultaneously with the optical scattering the effects of quantum charge transfer on plasmon coupling can be directly inferred under the assumption that the d.c. conductance is similar to the conductance at optical frequencies. Using this approach, the quantum limitations to plasmonics can be observed in fullness for the first time. This section concludes the experiments presented in this thesis and discusses the now readily attainable regime of plasmonics in sub-nm gaps. The investigation into the effects of quantum charge transport on plasmon coupling is the culmination of all previous developments to date, yielding some of the most interesting results of this project.

To briefly reiterate theory, according to [77], between separations of 0.5 nm and 1 nm gaps are expected to be in the crossover regime, where classical theory breaks down due to the onset of quantum tunnelling. Gaps are characterised by a thin barrier between particles with a growing probability for electrons incident on the barrier to tunnel through it. The non-locality of surface electrons smears gap surfaces on the quantum level, rounding the potential barrier in

the gap once wavefunctions begin to overlap. Long-range interactions between image charges also function to round the barrier. Tunnelling-induced charge transfer neutralises charge on the gap surfaces and reduces electromagnetic coupling. This decreases, and eventually halts, the rate of redshift and is otherwise known as the screening effect. Beyond 0.5 nm the increasingly overlapping wavefunctions cause the potential barrier to drop below the Fermi level, creating a conductive constriction. Ballistic conduction, as described by Landauer, now applies and gaps enter a quantised conductive regime. The increased currents cause hybridised modes to further decouple, blueshifting their resonances as they transform into CTPs.

These regime boundaries described by recent theory are often only a guideline as to what can be expected, with reported threshold separations for entering a conductive regime varying between 0.2 nm [77] and 0.3 nm [14, 69, 74, 81] (and in some predictions even larger separations [85]) depending on the specific dimer geometry and materials. Suggestions have also been made to indicate that the current contributions from two cooperative conductive channels can sum to an effective conductance, meaning larger particles should enter the quantum regime at larger separations when compared with smaller particles of the same material. In previous measurements this critical gap size has been determined by either comparing to theory [14], or by TEM measurement [81]. However, despite the frequent observation of a 0.3 nm threshold, this quantity is by no means fundamental and is therefore not the most appropriate standard by which to compare experiments. The critical separation is the point at which conductive charge transfer overpowers capacitive interaction, hence a set of critical conductances should exist for entry into each respective regime of quantum interaction, irrespective of gap size, that more fundamentally describe the effects of quantum transport on plasmon coupling.

As theory has previously suggested, critical conductances at optical frequencies are a more appropriate way of describing the regimes of quantum charge transfer behaviour [72, 86]. Experimentally this proves incredibly difficult. In a sense, plasmonics is the only way of measuring an optical conductance. Electronic equipment cannot respond fast enough to measure currents at optical frequencies. One reason as to why charge transfer effects should be understood is therefore to enable the application of plasmonics as a method of measuring conductance at frequencies where standard electronic technologies fail. At this time however, as an alternative to directly measuring the optical frequency conduction, the d.c. current through the gap is measured as an approximation of the electronic behaviour at optical frequencies. Using this, the current set of experiments explores the concept of critical conductances as the definitive way of interpreting charge transfer in plasmonic systems.

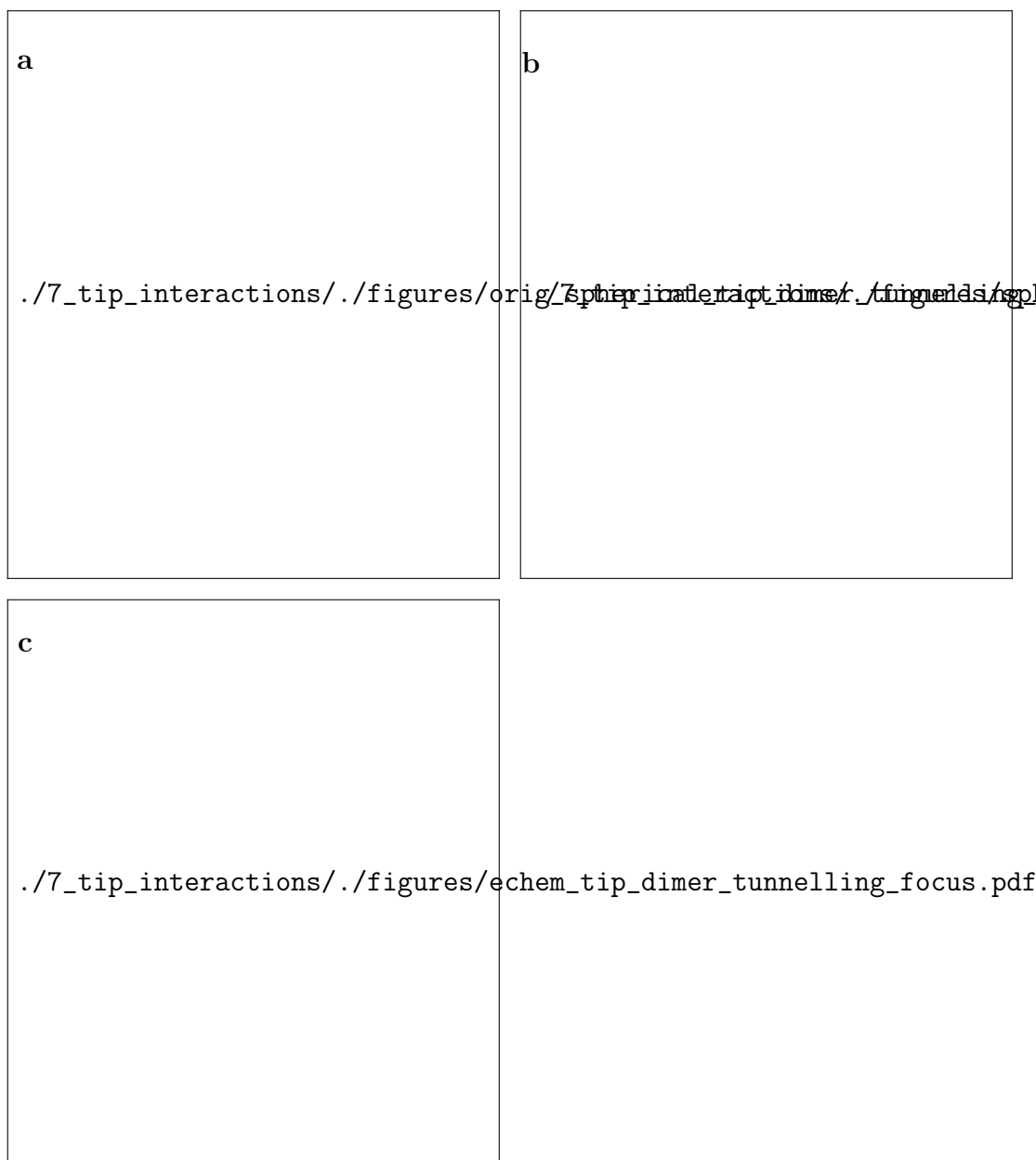


Figure 6.8: Scans of multiple spherical tip dimers pushing towards geometrical contact and showing varying phenomena. Scans show the supercontinuum dark-field scattering spectra as a function of the applied force on the gap with the simultaneously measured conductance superimposed over the axis. The circles highlight the position an evenly distributed selection of the peak position. The size of the circle indicates the amplitude of the mode in the fitted model. Scans a,c and d use Au-coated NanoTools B150 spherical AFM probes to form a dimer while scan b uses electrochemically-fabricated AuNP-on-Pt AFM tips.

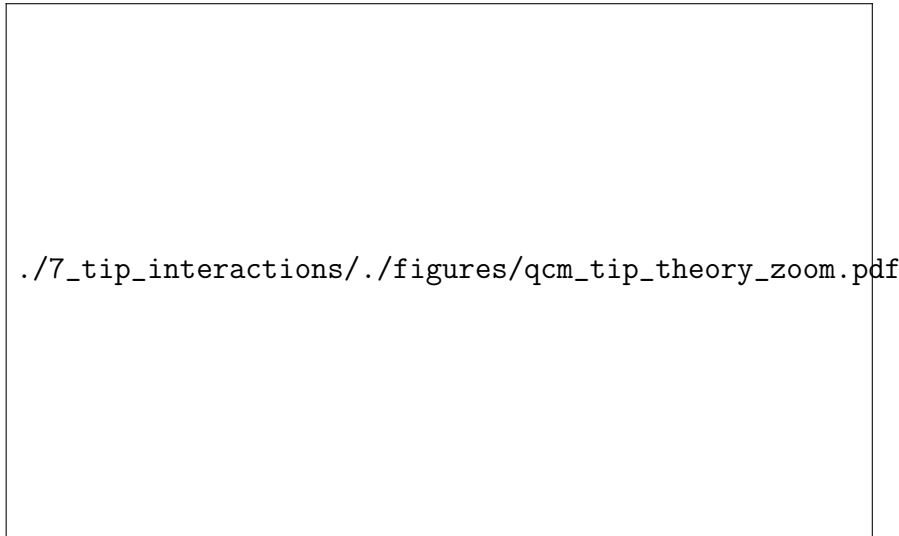


Figure 6.9: Select view of calculated QCM spectra of a spherical tip dimer as a function of separation [14]. Simulated spectra show that the higher order mode disappears and a CTP mode rises prior to geometrical contact at $d_{QR} = 0.3$ nm, prior to geometrical contact (g.c.). This occurs since coherent electron tunnelling transfers enough charge within half an optical cycle to screen hybridised plasmons and eventually excite a CTP. Based on DFT calculations the CTP is excited when the conductance density is $0.4 G_0 \text{ nm}^{-2}$.

6.3.1 Observations of Quantum Charge Transport in Plasmonic Cavities

Figure 6.8 shows a selection of spherical Au tip dimer measurements showing both optical and electronic behaviour once in the sub-nm regime. Simultaneous quantum tunnelling and SDF scattering measurements are presented as a function of the applied force on the gap. Each of the measurements exhibits the signatures of a transition between hybridised and charge transfer plasmons. Interestingly, each scan in the sub-nm regime manages to appear somewhat different in terms of mode behaviour, regardless of any similar agreement between scans in previous coupling regimes. These differences are thought to originate from surface roughness of even smaller differences in sub-nm scale morphology that affect the way optics and electronics couple. Correctly interpreting and understanding these results is of general importance within the current plasmonics community as smaller gaps begin to become experimentally attainable and the blending of plasmonics and molecular electronics becomes commonplace. To begin the discussion, each set of measurements is initially considered individually.

Both Figure 6.8a and b bear the closest resemblance to the original simulated QCM spectra of sub-nm gaps between spherical Au tips (replotted in Figure 6.9 with the DFT-calculated conductance density overlaid) [14], showing the screening of hybridised plasmons and the emergence of CTPs. Screening is indicated by a reduction in the rate of redshift and a decrease in intensity, followed by a blueshift and the formation of new CTP modes to signify the rise

of stronger interparticle currents. In theory, these critical currents occur at a conductance density of $0.4 G_0 \text{ nm}^{-2}$, at which point two CTPs emerge and hybridised modes disappear. Blueshifts in experimental data appear in similar spectral positions and are therefore similarly attributed to the excitation of CTPs. The fundamental CTP is not measurable using the current microscope as it exists outside the wavelength range of the spectrometers. The neck of the tip may also act as a short for this mode, preventing it from appearing at all. The behaviour of hybridised modes and higher order CTPs is thus used to interpret the behaviour in the gap.

In both experimental cases, the redshift of each hybridised modes becomes stunted once the conductance rises above $\sim 10^{-3} G_0$, indicating the onset of screening. This is the first critical conductance, revealing the point at which electron tunnelling has risen enough to effectively begin screening gap coupling. The point of blueshift is less clear in Figure 6.8a due to the fast transition into geometrical contact. This jump is experienced in almost all scans once the electrostatic pull of the tips is large enough to overcome the meniscus forces holding surfaces apart. Figure 6.8b provides a much clearer insight into the origins of the blueshift, and is likely the single most informative scan in terms of demonstrating both screening and blueshifting of plasmons and showing good agreement with the principles underpinning current theoretical models [14, 77]. Its tip approach is much more carefully controlled into geometrical contact, with many measurements in the tunnelling regime and clear observation of discretely quantised conductance channels. It is at this transition between tunnelling and one-dimensional conduction, at around $2G_0$, that the blueshift begins to occur and tips enter the quantum conductive regime.

A better view of this transition is shown in Figure 6.10a where the scan shown in Figure 6.8b is replotted with a linear conductance scale in order to closer inspect charge transfer behaviour. The turning point in the redshift of both hybridised plasmons visually appears to be at $2G_0$ in spectra. Fitting the spectra and extracting the behaviour of each individual mode provides a more quantitative analysis. The results of the fit are superimposed onto spectra in Figure 6.10a with relative peak shifts and mode amplitudes shown separately in Figure 6.10b. Mode positions follow an exponential model as expected. At $2 \times 10^{-3} G_0$ the redshift deviates from this model and becomes less pronounced. Prior to this point the amplitude of the lower order mode is decreasing, likely due to increasing charge localisation. Upon passing through the first critical conductance at $2 \times 10^{-3} G_0$ the amplitude is further screened and decreases faster. The higher order mode seemingly gains some intensity at this point, potentially from redistributed charge of the lowest order mode.

The second critical conductance can be defined as $2G_0$, a surprisingly appropriate quantity given that it occurs just above the transition from tunnelling into a quantum conductive regime. Upon surpassing $2G_0$ the resonance position of both hybridised plasmons begins to

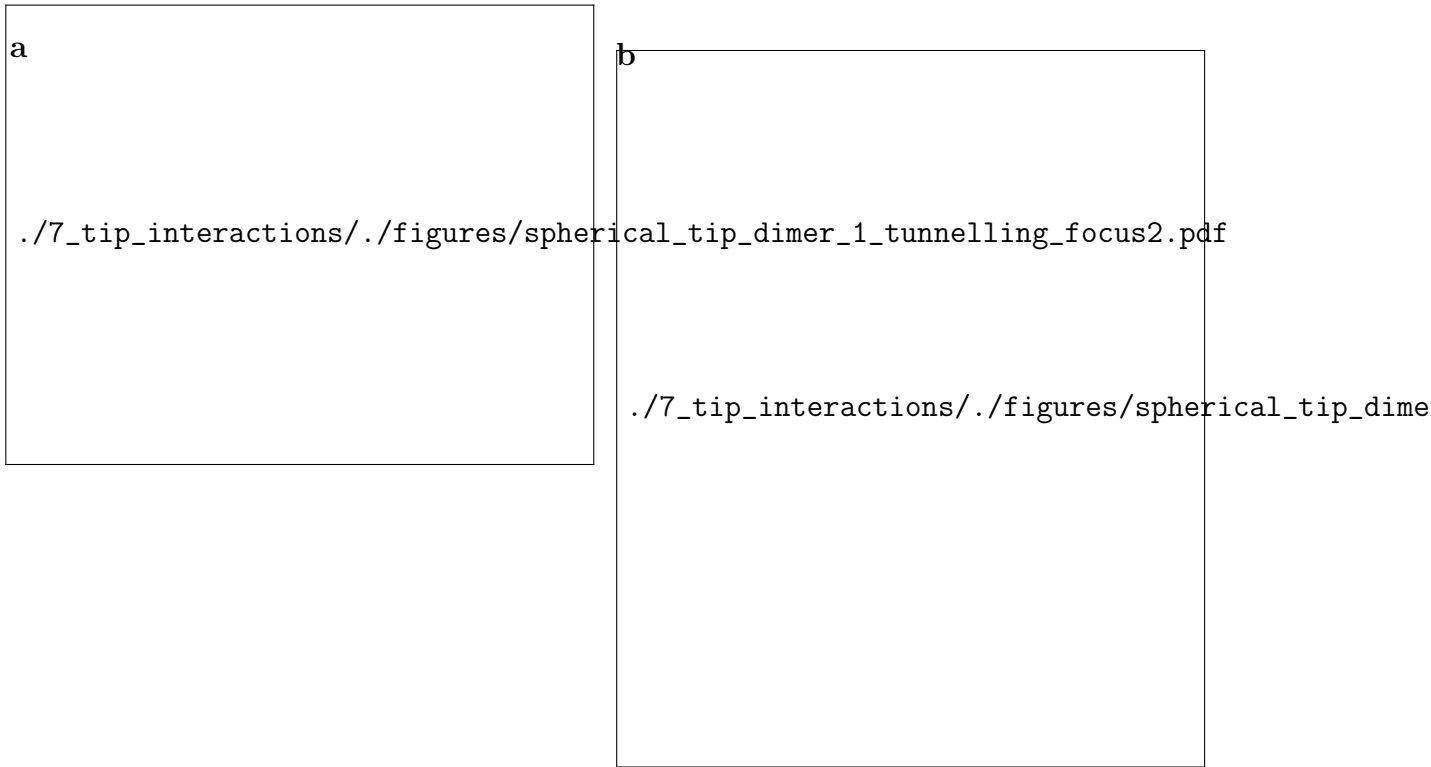


Figure 6.10: Detailed analysis of a spherical Au tip dimer scan in the quantum charge transfer regime. The scan shown in Figure 6.8b is replotted in (a) with a linear conductance scale to show quantised conductance stepping and its relationship with scattering spectra. Dashed lines indicate the point of blueshift at $G = 2G_0$. Peak positions in the fitted model are denoted by circles superimposed onto spectra with their size corresponding to the peak amplitude. The relative shift of each mode from fitted parameters, along with a normalised amplitude, is plotted in (b). Vertical dashed lines highlight the transitions into the tunnelling (crossover) regime at $2 \times 10^{-3}G_0$ and the conductive regime at $2G_0$. Exponential curves are fitted to the wavelength shift for $G < 10^{-3}G_0$ (dashed) and $G > 10^{-3}G_0$ (solid) to highlight the reduction in redshift caused by passing through the screening (tunnelling) threshold. Similar lines are plotting to show the increased amplitude screening upon passing through $2 \times 10^{-3}G_0$.

strongly blueshift as current passes through the junction, quickly returning to their initial resonance position prior to entering the tunnelling regime. During this transition into CTPs the intensity of the lowest energy plasmon begins to increase, while the higher order plasmon attenuates into only a weak, blueshifted resonance. This CTP becomes fully developed during the final pull into geometrical contact. A third critical conductance for CTP development can then be estimated to be around $10G_0$ with full development between $30\text{--}40G_0$.

Despite integer quantised conductance steps being observed in this conductive regime, there is no obvious step-wise behaviour in the optics. Given that it is the charge transfer that leads to the blueshift of hybridised modes it would be intuitive to expect quantised current changes to discretise incremental blueshifts. This is not obviously the case, with the blueshift appearing smooth throughout. More experimental data would be needed to properly

understand this observation.

Both sets of measurements at the focus of this discussion are not without their issues, however, when comparing with both theory and previous experimental results. Figure 6.8a shows variations in both the position and intensity of the 600 nm mode, which are attributed to changes in the torsional force on the gap, corresponding to a rotational motion of the tip. The intensities of the final two modes when in contact are also reversed compared with QCM predictions. Figure 6.8b looks remarkably closer to theory. Changes in CTP position and intensity are said to originate from the touching profile of the dimer, indicating that the surface roughness may play a role with such large dimer surfaces [77, 85].

Figure 6.8c shows a somewhat different phenomena to previous scans, though still in line with quantum transport expectations. Tips in Figure 6.8c are highly asymmetric AuNP-on-Pt tips, smoothed using piranha solution. Both have 40 N m^{-1} cantilever spring constants, hence the force resolution during approach is limited. Prior to tunnelling a higher order mode begins to emerge. The transition into contact is quick, with few to no point at any given conductance, ending initially with a stable $0.75\text{--}1.5G_0$ contact. Once the conductance has risen the initial SPR quickly diminishes without blueshifting and the higher order SPR gains intensity. The screening here is another example of entering into a tunnelling regime but without sufficient current below $2G_0$ to progress into the conductive regime and blueshift existing SPRs.

After the initial conductance increase, the tip is then retracted to test for reproducibility, as shown in the extended scan plot in Figure 6.11a. This is made possible by robustness of electrochemically fabricated tips, with their solid AuNP apices. Attempting this with commercial, spherical Au tips often results in the spherical tip separating from the neck due to adhesion forces. A second approach of the tip immediately after retracting out of contact demonstrates the same phenomenon until the conductance rises above $2G_0$ when both modes blueshift. Changes in the redshift and amplitude gradient show the effects of surface roughness as retraction introduces a small degree of misalignment between tips such that the point of closest contact in the second approach is different from the first.

A detailed mode analysis of the SPR positions and amplitudes is shown in Figure 6.11b, in which the trends described for previous measurements still apply. The peak position behaves as expected. Upon increasing the conductance up to the $1G_0$ level there is a visible kink in the redshift as its rate reduces as a result of screening. Once the conductance rises above $2G_0$ in the second approach there is a clear blueshift in the lowest order mode. This is a similar, although more abrupt, measurement of the critical conductance than in previous scans. The amplitude behaviour extracted from peak fits is interesting in this case since the amplitude of the initial mode linearly decreases during approach at exactly the same rate of increase as the emerging mode. This equality in the gradients is shown by the dotted red line in the figure indicating the constant sum of the two amplitudes. In a sense, charge is conserved and

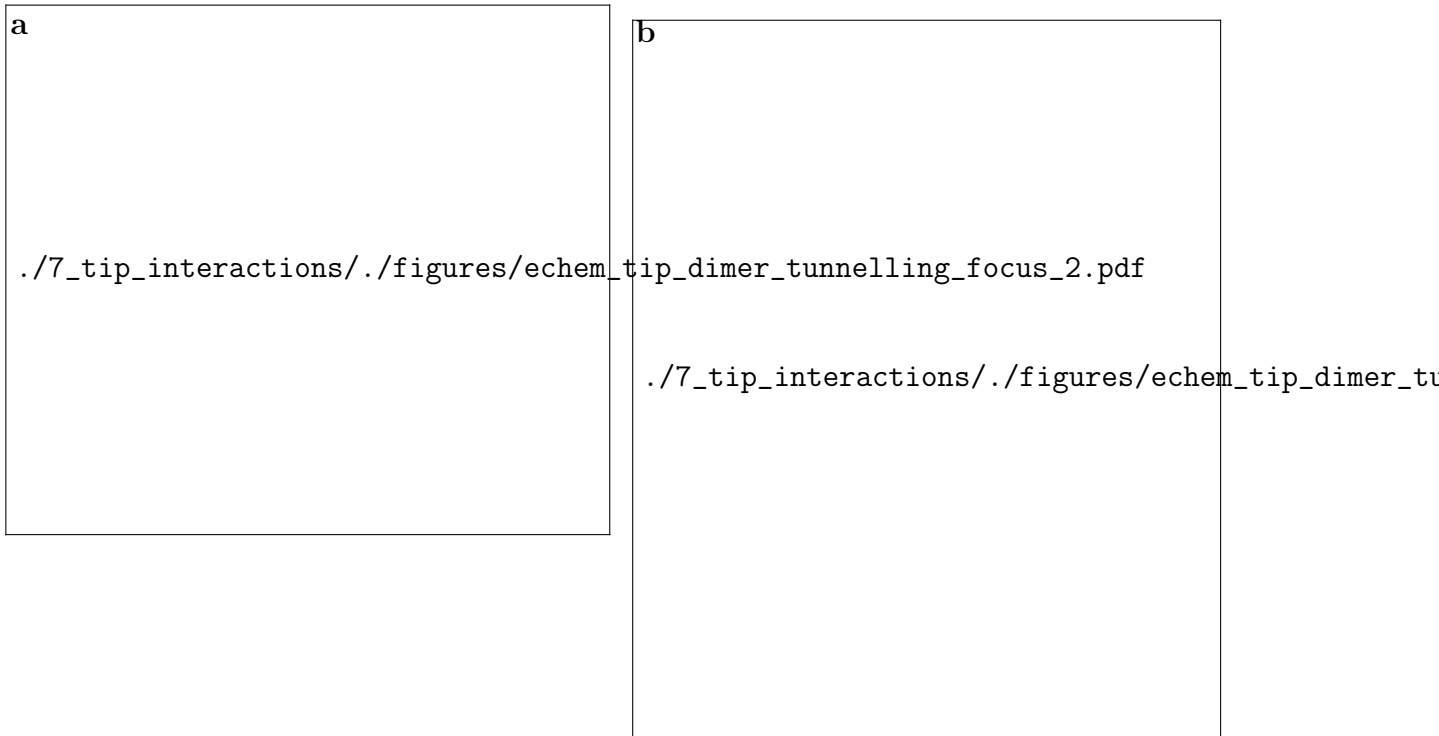


Figure 6.11: Detailed analysis of the extended electrochemically-fabricated spherical AuNP-on-Pt tip dimer scan. An extended plot of the scan shown in Figure 6.8c is plotted in (a), demonstrating reproducibility in approaches. The applied force trace represents the separation changes between tips, with tips approached, retracted and then finally approached into geometrical contact. Peak positions in the fitted model are denoted by circles superimposed onto spectra with their size corresponding to the peak amplitude. The relative shift of each mode from fitted parameters, along with a normalised amplitude, is plotted in (b). Linear rates of amplitude variation are revealed from peak fits, removing the width contribution from the peak intensity. Reduced rates of redshift are found in the $G \sim 1G_0$ regions with a discontinuous blueshift seen after the $G > 2G_0$ transition.

simply switches to a more favourable mode as the gap width decreases. Conceptually, this could suggest that tunnelling begins to reduce coupling between the lowest order modes first, making higher order coupled modes energetically more favourable.

Each of the presented three scans show agreement with recent theoretical concepts that define the influence of quantum transport on plasmon coupling. Critical conductances for entering the tunnelling regime and the quantum conductive regime are observed in each case in the vicinity of $1-2 \times 10^{-3}G_0$ and $2G_0$, respectively. No observation of CTP excitation has been made leaving the final critical conductance yet to be experimentally measured. This is the first time conductance values have been correlated dynamically with optical spectra. Comparison with previously explored systems shows excellent agreement, supporting the idea of a set of fixed critical conductances. Blueshifts of the BDP, forming the SBDP, begin to be seen in small conductive contacts at conductances of $2G_0$ in both theoretical models [71, 72]

and experimentally in the NPoM geometry when AuNPs are separated from a Au mirror by a blended SAM of variable conductance [86]. Observation of the same threshold conductance in two very different systems provides strong evidence for the fundamental nature of critical conductances. Variations in measured quantum transport phenomena between tip dimers are highly likely to be the result of surface roughness changing the charge distribution on gap surfaces. In each situation plasmon coupling would behave differently depending on the localisation of field in the gap and the location and summation of all points of optical tunnelling [85].

Further, more controlled, confirmation of similar quantum effects could be possible using 2D electron gases (2DEGs), the materials initially used to discover quantised conductivity, and those currently being explored for plasmonics. In the original concept a 2DEG is biased at two ends, gated in the centre and electrically depleted to form a 1D constriction through which ballistic transport occurs [237, 238]. Modern 2DEG systems have been shown to support plasmons in the THz regime [239–241]. Thus by gating a plasmonic 2DEG it could be controllably depleted to pass through both the capacitively coupled and conductive regimes.

To summarise, charge transfer in systems of coupled plasmons exhibit three distinct regimes of interactions. For small conductances characteristic of electron tunnelling ($1\text{--}2 \times 10^{-3}G_0$) coupling begins to be screened by the tunnelling field and the rate of redshift is steadily reduced. Upon passing through the second critical conductance at $2G_0$, also known as G_{SBDP} in the literature [71, 72], the hybridised modes blueshift and transform into higher order CTPs due to increased screening from conductive charge flow in the gap. At this point the gap behaves as a 1D constriction subject to Landauer ballistic quantised conduction. The final conductance threshold, that for CTP excitation, has not yet been determined but instead roughly estimated to be around $30\text{--}40G_0$ from final conductance values of geometrically contacted gap surfaces. To restate the significance of this work, this is the first time these critical conductance thresholds have been measured in a dynamic dimer system through correlations between simultaneously measured optics and electronics. Using this information, the performance of a sub-nm plasmon system can begin to be characterised and quantified based upon which regime it falls under.

6.4 Conclusions

Multiple different combinations of tips in a dimer configuration are used to probe plasmon coupling. Sharp Au tips exhibit no obvious plasmon resonances under far-field illumination and no gap mode coupling is observed with other sharp or spherical Au tips. This is caused by the lack of an antenna-like geometry in sharp tips. Plasmons excited at the apex of spherical Au tips, on the other hand, interact and hybridise. The behaviour of these modes is as

expected, with similarity to plasmons in AuNP dimers. The inherent asymmetry between the large spherical tip structures leads to more complex scattering spectra wherein anti-bonding modes are no longer dark. Their evolution into gap modes is something not previously seen before in a single dynamic system.

To conclude experimental work, tip dimers are used to determine the influence of quantum effects, specifically forms of quantum charge transport, on plasmon coupling in sub-nm gaps. Using this approach, the development of a charge transfer plasmonic regime is dynamically observed as classical plasmon hybridisation is heavily screened. Critical conductances are estimated for each domain change using direct correlations between optical spectra and current measurements, showing agreement with theoretical principles. Though no quantitative measurements, such as temperature, voltage or power dependences, are made to guarantee that charge transfer is via quantum tunnelling and ballistic transport, these are the most likely mechanisms. Further investigation could quantify this, although sub-nm gap phenomena are not expected to depend on the conduction mechanism. Comparison with tip dimers coated in different molecular layers of varying conductivities would also further understanding into the effects of charge transfer in plasmonic systems and forms the basis of future experiments on this topic.

In summary, the existence of two distinct regimes of quantum charge transport have been detected in sub-nm plasmonic cavities. These are:

- The crossover regime (also known as the tunnelling regime), wherein electrons tunnelling through the barrier screen the capacitive interaction between opposite gap surfaces, reducing plasmon coupling strength and slowing coupling to a halt.
- The conductive regime, where strong currents at G_0 -level conductances heavily attenuate hybridised plasmons leading to the previously observed blueshift transition into charge transfer plasmons.

Though numerous theoretically predictions have been in recent years, this is the first time that correlated experimental measurements between plasmon resonances and conductance have been performed.

This project has focussed on the understanding and application of tips for plasmonics, with the aim to use tips to further understand the recently revealed sub-nm regime of plasmonic coupling. Though the initial motivation was to investigate the quantum regime of plasmon coupling, the project diversified into studying the optical differences between sharp and spherical tips, using techniques such as hyperspectral imaging and plasmon coupling, the development of an electrochemical method as an alternative approach to producing spherical tips and the application of plasmonic tips for TERS. Finally, spherical tips were applied to investigating quantum effects in the sub-nm plasmonic coupling regime. Work was therefore split between three core areas: development of plasmonic tips, design and construction of a custom microscope for tip experiments, and ultimately performing experiments on the combined tip systems.

Failure to observe any plasmonic behaviour in the far-field optical spectra of sharp Au AFM tips, despite their prominence in many near-field enhancing techniques, led to the investigation into nanostructured tip geometries. By nanostructuring an AFM tip, some of the well-known antenna-like properties of isolated plasmonic nanoparticles are transferred into the AFM probe form factor. Knowing that the particular tip nanostructure and optical geometry set which plasmons are radiative, and can therefore be experimentally observed, the spherical geometry was chosen for its simplicity. Both commercial, spherical Au tips, used in previous tip plasmonics experiments, and AuNP-on-Pt tips, fabricated in-house using a newly developed pulsed electrodeposition procedure, were studied. Pulsed electrodeposition was chosen for its ability to exploit the sharp apex of AFM tips and quickly produce nanostructured tips. The technique was developed from the conception of the idea through to beginning the optimisation of each of the parameters in order to improve the reliability of the process and gain control of the tip morphology. Due to time constraints and the significant effort required to complete other aspects of this project, the controllable growth of spherically-tipped AFM probes through pulsed electrodeposition was only partially optimised but produced enough samples to facilitate experiments. Further work is still needed to understand the exact mech-

anism by which nanoparticles nucleate and grow at and around the apex and optimise each growth parameter. Achieving this would enable a large number of varied studies into the application of plasmonic tips for TENOM - a direction of research only touched upon during this project.

The optical study of AFM tips and the continued probing of plasmonic coupling through each interaction regime necessitated the design of a custom microscope capable of combining the function and stability of two opposing AFM devices with a platform for broadband dark-field spectroscopy. The novel design and robust performance of the microscope has been discussed at length and quantified where appropriate. The comprehensive design of the dual-tip platform meant experiments could implement optical, electronic and force measurements for a more complete characterisation of a plasmonic system than is capable in many other experimental setups. Specifically, the combination of hyperspectral imaging and scanning capacitance microscopy enabled the alignment of AFM tips to the focus of the incident beam and to each other, resulting in a highly reproducible plasmonic dimer arrangement. Additionally, the modular design of the microscope and its array of possible measurements make it adaptable and extensible for many other (future) experiments. Within the scope of this project its main use has been to perform experiments on spherical Au tips.

Observations of strong resonances in spherical Au tips was attributed to plasmon excitation - a feature not found in sharp metallic tips. The agreement between apex spectra extracted from hyperspectral imaging, broadband tuneable SERS and dynamic plasmon coupling experiments confirm that spherical metallic tips support antenna-like plasmons similar to those in an individual nanoparticle, while sharp metallic tips remain unresponsive to light. The spherical Au tip SPR conveniently exists at the commonly used HeNe wavelength leading to a strongly enhanced Raman response, $30\times$ that of a sharp Au tip. This improvement is a step towards better exploiting controlled nanostructuring of tips for more enhanced and reliable sensing and promoting radiative approaches to TENOM. However, direct comparison with evanescent excitation methods has not been performed and conclusions remain speculative for the time being.

Though the results presented within this project only focusses on large, spherical Au tips, the developed fabrication and characterisation techniques are not limited to a specific metal or geometry. It would be interesting to measure and quantitatively compare the scattering response of spherical tips with carefully controlled sphere and neck sizes to validate theoretical predictions, and other sphere materials such as Ag, Cu or Al, if such material tips electrochemically deposit in a similar manner to Au. TERS carried out on resonance with each type of tip would confirm plasmonic enhancement. A small amount of work was started, with some success, applying pulsed electrodeposition to deposit metal nanostructures other than Au on other conductive AFM tips, such as highly-doped Si. If successful this would facilitate the

production of plasmonic probes resonant across a wide range of visible-NIR frequencies.

The final sets of measurements used pairs of spherical Au tips to target the sub-nm coupling regime. The onset of quantum effects on plasmonic coupling were investigated in ambient conditions, following on from the earlier experiment performed by Savage *et al.* [14]. Though the experiment conceptually appears similar, the addition of tunnelling conduction and gap force measurements greatly increased the amount of information that could be extracted to better understand the physics of sub-nm gaps. The robust design of the microscope platform enabled many successful scans through the quantum regime, observing a range of different coupling behaviour. Measurements showed both the screening of coupled plasmons followed by their transformation into CTPs, correlated with the onset of quantum tunnelling and ballistic transport. Correlations differed between different pairs of tips, however the more controlled scans clearly demonstrated the transition between coupled and charge transfer plasmons correlates with the transition between tunnelling and ballistic conduction. Further deviations from this are attributed to differences in the gap morphology leading to different charge distributions interacting with sites of charge transfer. Observations are in general agreement with the principles underlying the theoretical description of the quantum regime though further theoretical affirmation of these results is still required.

7.1 Outlook and Future Directions

The experiments carried out have both demonstrated the appeal of nanostructured tips and expanded upon the rich regime of tunnelling plasmonics for further exploration. The project leaves at a pivotal point at which sub-nm gaps can reliably be probed using a newly-developed microscope platform. Within the current experimental system there is still a large amount of scope for further projects and many questions regarding the effects of quantum mechanics on plasmonics still require answers. Experimental parameters, such as temperature, humidity (gap water content) and applied bias (non-linear electrical control of coupled plasmons), are currently controllable but investigations into their effects on quantum-scale plasmonic gaps have yet to begin. Other parameters, such as pressure (vacuum), will require some adaptation but investigations remain possible.

Even in its current state the microscope platform could be used to perform a range of new and interesting experiments. Use of an electrical excitation mechanism has yet to be tested but is a realistic aim that could yield interesting results and background-free spectroscopy. Coating tips in both conductive and insulating molecules could probe an effective method of determining critical conductances, with direct comparison to recent NPoM systems involving gap spacers [42, 54, 86]. Coupling a tip with its mirror charge in an opposing cantilever is also a potential route for dynamically testing plasmonic interactions with molecular spacers. Each of these would provide a new insight into plasmonics on a fundamental level.

To conclude, the boundary between the capacitive coupling and charge transfer regimes of plasmonics has only recently become accessible, displaying a wealth of interesting physics in only a short period of time. Dynamically controlling the particle positions of an AFM tip dimer has become a powerful technique for the study of such physics and the results provided by it are expected to be of great interest to the general plasmonic community. From the point of view of fundamental plasmonics, they provide an insight into a largely unknown regime of plasmonics whilst from an applied aspect they indicate the limitations of plasmonics.

References

- [1] M. Fleischmann, P. J. Hendra, and A. McQuillan, “Raman spectra of pyridine adsorbed at a silver electrode”, *Chemical Physics Letters* **26**, 163–166 (1974).
- [2] D. L. Jeanmaire and R. P. Van Duyne, “Surface raman spectroelectrochemistry: part i. heterocyclic, aromatic, and aliphatic amines adsorbed on the anodized silver electrode”, *Journal of Electroanalytical Chemistry and Interfacial Electrochemistry* **84**, 1–20 (1977).
- [3] E. Ash and G Nicholls, “Super-resolution aperture scanning microscope”, *Nature* **237**, 510–512 (1972).
- [4] D. W. Pohl, W Denk, and M Lanz, “Optical stethoscopy: image recording with resolution $\lambda/20$ ”, *Applied physics letters* **44**, 651–653 (1984).
- [5] A. Lewis et al., “Development of a 500 Å spatial resolution light microscope: i. light is efficiently transmitted through $\lambda/16$ diameter apertures”, *Ultramicroscopy* **13**, 227–231 (1984).
- [6] W. D. Pohl, *Optical near-field scanning microscope*, US Patent 4,604,520, 1986.
- [7] A Harootunian et al., “Super-resolution fluorescence near-field scanning optical microscopy”, *Applied Physics Letters* **49**, 674–676 (1986).
- [8] E Betzig et al., “Near-field scanning optical microscopy (nsom)”, in 1988 los angeles symposium–oe/lase’88 (International Society for Optics and Photonics, 1988), pp. 91–99.
- [9] L. Novotny and N. Van Hulst, “Antennas for light”, *Nature Photonics* **5**, 83–90 (2011).
- [10] C. V. Raman, “A new radiation”, *Indian Journal of physics* **2**, 387–398 (1928).
- [11] R Zhang et al., “Chemical mapping of a single molecule by plasmon-enhanced raman scattering”, *Nature* **498**, 82–86 (2013).
- [12] G. Binnig et al., “Surface studies by scanning tunneling microscopy”, *Physical review letters* **49**, 57 (1982).
- [13] G. Binnig, C. F. Quate, and C. Gerber, “Atomic force microscope”, *Physical review letters* **56**, 930 (1986).
- [14] K. J. Savage et al., “Revealing the quantum regime in tunnelling plasmonics”, *Nature* **491**, 574–577 (2012).
- [15] P. Drude, “Zur elektronentheorie der metalle”, *Annalen der Physik* **306**, 566–613 (1900).
- [16] P. B. Johnson and R.-W. Christy, “Optical constants of the noble metals”, *Physical Review B* **6**, 4370 (1972).

- [17] R. Egerton, *Electron energy-loss spectroscopy in the electron microscope* (Springer Science & Business Media, 2011).
- [18] C. Kittel, P. McEuen, and P. McEuen, *Introduction to solid state physics*, Vol. 8 (Wiley New York, 1976).
- [19] A. Otto, “Excitation of nonradiative surface plasma waves in silver by the method of frustrated total reflection”, *Zeitschrift für Physik* **216**, 398–410 (1968).
- [20] E. Kretschmann, “Die bestimmung optischer konstanten von metallen durch anregung von oberflächenplasmaschwingungen”, *Zeitschrift für Physik* **241**, 313–324 (1971).
- [21] R. Wood, “On a remarkable case of uneven distribution of light in a diffraction grating spectrum”, *The London, Edinburgh, and Dublin Philosophical Magazine and Journal of Science* **4**, 396–402 (1902).
- [22] U Fano, “The theory of anomalous diffraction gratings and of quasi-stationary waves on metallic surfaces (sommerfeld’s waves)”, *JOSA* **31**, 213–222 (1941).
- [23] W. A. Murray and W. L. Barnes, “Plasmonic materials”, *Advanced materials* **19**, 3771–3782 (2007).
- [24] S. A. Maier, *Plasmonics: fundamentals and applications* (Springer Science & Business Media, 2007).
- [25] J. D. Jackson, *Classical electrodynamics* (John Wiley & Sons, 1999).
- [26] E Prodan and P. Nordlander, “Plasmon hybridization in spherical nanoparticles”, *The Journal of chemical physics* **120**, 5444–5454 (2004).
- [27] C Sönnichsen et al., “Spectroscopy of single metallic nanoparticles using total internal reflection microscopy”, *Applied Physics Letters* **77**, 2949–2951 (2000).
- [28] J. Krenn et al., “Design of multipolar plasmon excitations in silver nanoparticles”, *Applied Physics Letters* **77**, 3379–3381 (2000).
- [29] J. Mock et al., “Shape effects in plasmon resonance of individual colloidal silver nanoparticles”, *The Journal of Chemical Physics* **116**, 6755–6759 (2002).
- [30] H. Kuwata et al., “Resonant light scattering from metal nanoparticles: practical analysis beyond rayleigh approximation”, *Applied physics letters* **83**, 4625–4627 (2003).
- [31] X. Huang et al., “Cancer cell imaging and photothermal therapy in the near-infrared region by using gold nanorods”, *Journal of the American Chemical Society* **128**, 2115–2120 (2006).
- [32] X. Huang et al., “Plasmonic photothermal therapy (pptt) using gold nanoparticles”, *Lasers in medical science* **23**, 217–228 (2008).
- [33] X. Huang and M. A. El-Sayed, “Gold nanoparticles: optical properties and implementations in cancer diagnosis and photothermal therapy”, *Journal of Advanced Research* **1**, 13–28 (2010).
- [34] C. Noguez, “Surface plasmons on metal nanoparticles: the influence of shape and physical environment”, *The Journal of Physical Chemistry C* **111**, 3806–3819 (2007).
- [35] I. S. Grant and W. R. Phillips, *Electromagnetism* (John Wiley & Sons, 2013).

- [36] C. F. Bohren and D. R. Huffman, *Absorption and scattering of light by small particles* (John Wiley & Sons, 2008).
- [37] S. Berweger et al., “Light on the tip of a needle: plasmonic nanofocusing for spectroscopy on the nanoscale”, *The Journal of Physical Chemistry Letters* **3**, 945–952 (2012).
- [38] P. Bharadwaj, B. Deutsch, and L. Novotny, “Optical antennas”, *Advances in Optics and Photonics* **1**, 438–483 (2009).
- [39] G. Mie, “Beiträge zur optik trüber medien, speziell kolloidaler metallösungen”, *Annalen der physik* **330**, 377–445 (1908).
- [40] F. Huang and J. J. Baumberg, “Actively tuned plasmons on elastomerically driven au nanoparticle dimers”, *Nano letters* **10**, 1787–1792 (2010).
- [41] M. G. Millyard et al., “Stretch-induced plasmonic anisotropy of self-assembled gold nanoparticle mats”, *Applied Physics Letters* **100**, 073101 (2012).
- [42] J. Mertens et al., “Controlling subnanometer gaps in plasmonic dimers using graphene”, *Nano letters* **13**, 5033–5038 (2013).
- [43] R. W. Taylor et al., “Watching individual molecules flex within lipid membranes using sers”, *Scientific reports* **4** (2014).
- [44] N. C. Lindquist et al., “Tip-based plasmonics: squeezing light with metallic nanoprobe”, *Laser & Photonics Reviews* **7**, 453–477 (2013).
- [45] S. A. Maier, P. G. Kik, and H. A. Atwater, “Observation of coupled plasmon-polariton modes in au nanoparticle chain waveguides of different lengths: estimation of waveguide loss”, *Applied Physics Letters* **81**, 1714–1716 (2002).
- [46] T. Atay, J.-H. Song, and A. V. Nurmikko, “Strongly interacting plasmon nanoparticle pairs: from dipole-dipole interaction to conductively coupled regime”, *Nano Letters* **4**, 1627–1631 (2004).
- [47] O. Muskens et al., “Optical scattering resonances of single and coupled dimer plasmonic nanoantennas”, *Optics express* **15**, 17736–17746 (2007).
- [48] R. W. Taylor et al., “Precise subnanometer plasmonic junctions for sers within gold nanoparticle assemblies using cucurbit [n] uril “glue””, *ACS nano* **5**, 3878–3887 (2011).
- [49] L. Herrmann et al., “Self-sifting of chain plasmons: the complex optics of au nanoparticle clusters”, *Optics express* **21**, 32377–32385 (2013).
- [50] T. Okamoto and I. Yamaguchi, “Optical absorption study of the surface plasmon resonance in gold nanoparticles immobilized onto a gold substrate by self-assembly technique”, *The Journal of Physical Chemistry B* **107**, 10321–10324 (2003).
- [51] J. K. Daniels and G. Chumanov, “Nanoparticle-mirror sandwich substrates for surface-enhanced raman scattering”, *The Journal of Physical Chemistry B* **109**, 17936–17942 (2005).
- [52] M. K. Kinnan and G. Chumanov, “Surface enhanced raman scattering from silver nanoparticle arrays on silver mirror films: plasmon-induced electronic coupling as the enhancement mechanism”, *The Journal of Physical Chemistry C* **111**, 18010–18017 (2007).

- [53] S. Mubeen et al., “Plasmonic properties of gold nanoparticles separated from a gold mirror by an ultrathin oxide”, *Nano letters* **12**, 2088–2094 (2012).
- [54] B. de Nijs et al., “Unfolding the contents of sub-nm plasmonic gaps using normalising plasmon resonance spectroscopy”, *Faraday Discussions* (2014).
- [55] I. Romero et al., “Plasmons in nearly touching metallic nanoparticles: singular response in the limit of touching dimers”, *Optics Express* **14**, 9988–9999 (2006).
- [56] E. Hao and G. C. Schatz, “Electromagnetic fields around silver nanoparticles and dimers”, *The Journal of chemical physics* **120**, 357–366 (2004).
- [57] C. E. Talley et al., “Surface-enhanced raman scattering from individual au nanoparticles and nanoparticle dimer substrates”, *Nano Letters* **5**, 1569–1574 (2005).
- [58] U. Kreibig and M. Vollmer, *Optical properties of metal clusters*, Vol. 25 (Springer Berlin, 1995).
- [59] M. Gluodenis and C. A. Foss, “The effect of mutual orientation on the spectra of metal nanoparticle rod-rod and rod-sphere pairs”, *The Journal of Physical Chemistry B* **106**, 9484–9489 (2002).
- [60] W. Rechberger et al., “Optical properties of two interacting gold nanoparticles”, *Optics Communications* **220**, 137–141 (2003).
- [61] N. J. Halas et al., “Plasmons in strongly coupled metallic nanostructures”, *Chemical reviews* **111**, 3913–3961 (2011).
- [62] P. K. Jain, W. Huang, and M. A. El-Sayed, “On the universal scaling behavior of the distance decay of plasmon coupling in metal nanoparticle pairs: a plasmon ruler equation”, *Nano Letters* **7**, 2080–2088 (2007).
- [63] X. Ben and H. S. Park, “Size dependence of the plasmon ruler equation for two-dimensional metal nanosphere arrays”, *The Journal of Physical Chemistry C* **115**, 15915–15926 (2011).
- [64] P. Nordlander et al., “Plasmon hybridization in nanoparticle dimers”, *Nano Letters* **4**, 899–903 (2004).
- [65] E. Prodan et al., “A hybridization model for the plasmon response of complex nanostructures”, *Science* **302**, 419–422 (2003).
- [66] P. Nordlander and E. Prodan, “Plasmon hybridization in nanoparticles near metallic surfaces”, *Nano Letters* **4**, 2209–2213 (2004).
- [67] M.-W. Chu et al., “Probing bright and dark surface-plasmon modes in individual and coupled noble metal nanoparticles using an electron beam”, *Nano letters* **9**, 399–404 (2008).
- [68] A. L. Koh et al., “Electron energy-loss spectroscopy (eels) of surface plasmons in single silver nanoparticles and dimers: influence of beam damage and mapping of dark modes”, *Acs Nano* **3**, 3015–3022 (2009).
- [69] R. Esteban et al., “Bridging quantum and classical plasmonics with a quantum-corrected model”, *Nature Communications* **3**, 825 (2012).
- [70] J. B. Lassiter et al., “Close encounters between two nanoshells”, *Nano letters* **8**, 1212–1218 (2008).

- [71] O Pérez-González et al., “Optical spectroscopy of conductive junctions in plasmonic cavities”, *Nano letters* **10**, 3090–3095 (2010).
- [72] O Pérez-González, N Zabala, and J Aizpurua, “Optical characterization of charge transfer and bonding dimer plasmons in linked interparticle gaps”, *New Journal of Physics* **13**, 083013 (2011).
- [73] C. Tserkezis et al., “Optical response of threaded chain plasmons: from capacitive chains to continuous nanorods”, *Optics express* **22**, 23851–23860 (2014).
- [74] R. Esteban et al., “A classical treatment of optical tunneling in plasmonic gaps: extending the quantum corrected model to practical situations”, *Faraday discussions* **178**, 151–183 (2015).
- [75] J. G. Simmons, “Generalized formula for the electric tunnel effect between similar electrodes separated by a thin insulating film”, *Journal of Applied Physics* **34**, 1793–1803 (1963).
- [76] J. M. Blanco, F. Flores, and R. Pérez, “Stm-theory: image potential, chemistry and surface relaxation”, *Progress in surface science* **81**, 403–443 (2006).
- [77] J. Zuloaga, E. Prodan, and P. Nordlander, “Quantum description of the plasmon resonances of a nanoparticle dimer”, *Nano letters* **9**, 887–891 (2009).
- [78] R. Landauer, “Spatial variation of currents and fields due to localized scatterers in metallic conduction”, *IBM Journal of Research and Development* **1**, 223–231 (1957).
- [79] H. Cha, J. H. Yoon, and S. Yoon, “Probing quantum plasmon coupling using gold nanoparticle dimers with tunable interparticle distances down to the subnanometer range”, *ACS nano* **8**, 8554–8563 (2014).
- [80] W. Zhu and K. B. Crozier, “Quantum mechanical limit to plasmonic enhancement as observed by surface-enhanced raman scattering”, *Nature communications* **5** (2014).
- [81] J. A. Scholl et al., “Observation of quantum tunneling between two plasmonic nanoparticles”, *Nano letters* **13**, 564–569 (2013).
- [82] V. Kravtsov et al., “Control of plasmon emission and dynamics at the transition from classical to quantum coupling”, *Nano letters* **14**, 5270–5275 (2014).
- [83] G. Hajisalem, M. S. Nezami, and R. Gordon, “Probing the quantum tunneling limit of plasmonic enhancement by third harmonic generation”, *Nano letters* **14**, 6651–6654 (2014).
- [84] S. F. Tan et al., “Quantum plasmon resonances controlled by molecular tunnel junctions”, *Science* **343**, 1496–1499 (2014).
- [85] M. Barbry et al., “Atomistic near-field nanoplasmonics: reaching atomic-scale resolution in nanooptics”, *Nano letters* (2015).
- [86] F. Benz et al., “Nano-optics of molecular-shunted plasmonic nanojunctions”, *Nano letters* (2014).
- [87] L. O. Herrmann et al., “Threading plasmonic nanoparticle strings with light”, *Nature communications* **5** (2014).
- [88] R. M. Stöckle et al., “Nanoscale chemical analysis by tip-enhanced raman spectroscopy”, *Chemical Physics Letters* **318**, 131–136 (2000).

- [89] M. S. Anderson, “Locally enhanced raman spectroscopy with an atomic force microscope”, *Applied Physics Letters* **76**, 3130–3132 (2000).
- [90] N. Hayazawa et al., “Metallized tip amplification of near-field raman scattering”, *Optics Communications* **183**, 333–336 (2000).
- [91] B. Pettinger et al., “Surface enhanced raman spectroscopy: towards single molecular spectroscopy”, *Electrochemistry* **68**, 942–949 (2000).
- [92] F. Zenhausern, M. O’boyle, and H. Wickramasinghe, “Apertureless near-field optical microscope”, *Applied Physics Letters* **65**, 1623–1625 (1994).
- [93] F. Zenhausern, Y. Martin, and H. Wickramasinghe, “Scanning interferometric apertureless microscopy: optical imaging at 10 angstrom resolution”, *Science* **269**, 1083–1085 (1995).
- [94] R. Bachelot, P. Gleyzes, and A. Boccarda, “Near-field optical microscope based on local perturbation of a diffraction spot”, *Optics letters* **20**, 1924–1926 (1995).
- [95] B. Knoll et al., “Contrast of microwave near-field microscopy”, *Applied physics letters* **70**, 2667–2669 (1997).
- [96] B. Knoll and F. Keilmann, “Scanning microscopy by mid-infrared near-field scattering”, *Applied Physics A: Materials Science & Processing* **66**, 477–481 (1998).
- [97] F. Keilmann, B. Knoll, and A. Kramer, “Long-wave-infrared near-field microscopy”, *physica status solidi (b)* **215**, 849–854 (1999).
- [98] J. Wessel, “Surface-enhanced optical microscopy”, *JOSA B* **2**, 1538–1541 (1985).
- [99] B. Pettinger et al., “Tip-enhanced raman spectroscopy: near-fields acting on a few molecules”, *Annual review of physical chemistry* **63**, 379–399 (2012).
- [100] C. Neacsu, G. Steudle, and M. Raschke, “Plasmonic light scattering from nanoscopic metal tips”, *Applied Physics B* **80**, 295–300 (2005).
- [101] D. Mehtani et al., “Optical properties and enhancement factors of the tips for apertureless near-field optics”, *Journal of Optics A: Pure and Applied Optics* **8**, S183 (2006).
- [102] T. Wang et al., “Excitation of propagating surface plasmons with a scanning tunnelling microscope”, *Nanotechnology* **22**, 175201 (2011).
- [103] L. Novotny and S. J. Stranick, “Near-field optical microscopy and spectroscopy with pointed probes”, *Annu. Rev. Phys. Chem.* **57**, 303–331 (2006).
- [104] J. Steidtner and B. Pettinger, “High-resolution microscope for tip-enhanced optical processes in ultrahigh vacuum”, *Review of Scientific Instruments* **78**, 103104 (2007).
- [105] H. K. Wickramasinghe et al., “Billion-fold increase in tip-enhanced raman signal”, *ACS nano* **8**, 3421–3426 (2014).
- [106] N. Hayazawa et al., “Near-field raman scattering enhanced by a metallized tip”, *Chemical Physics Letters* **335**, 369–374 (2001).
- [107] B.-S. Yeo et al., “Enhancement of raman signals with silver-coated tips”, *Applied spectroscopy* **60**, 1142–1147 (2006).
- [108] B.-S. Yeo et al., “Towards rapid nanoscale chemical analysis using tip-enhanced raman spectroscopy with ag-coated dielectric tips”, *Analytical and bioanalytical chemistry* **387**, 2655–2662 (2007).

- [109] M. Zhang et al., “Experimental research on the spectral response of tips for tip-enhanced raman spectroscopy”, *Journal of Optics* **15**, 055006 (2013).
- [110] T. Mino, Y. Saito, and P. Verma, “Quantitative analysis of polarization-controlled tip-enhanced raman imaging through the evaluation of the tip dipole”, *ACS nano* **8**, 10187–10195 (2014).
- [111] N. Kumar, A. Rae, and D. Roy, “Accurate measurement of enhancement factor in tip-enhanced raman spectroscopy through elimination of far-field artefacts”, *Applied Physics Letters* **104**, 123106 (2014).
- [112] N. Hayazawa et al., “Focused excitation of surface plasmon polaritons based on gap-mode in tip-enhanced spectroscopy”, *Japanese Journal of Applied Physics* **46**, 7995 (2007).
- [113] A. Taguchi et al., “Controlling the plasmon resonance wavelength in metal-coated probe using refractive index modification”, *Optics express* **17**, 6509–6518 (2009).
- [114] K. Uetsuki et al., “Tunable plasmon resonances in a metallic nanotip–film system”, *Nanoscale* **4**, 5931–5935 (2012).
- [115] R. Esteban, R. Vogelgesang, and K. Kern, “Simulation of optical near and far fields of dielectric apertureless scanning probes”, *Nanotechnology* **17**, 475 (2006).
- [116] W. Zhang, X. Cui, and O. J. Martin, “Local field enhancement of an infinite conical metal tip illuminated by a focused beam”, *Journal of Raman Spectroscopy* **40**, 1338–1342 (2009).
- [117] T. Schmid et al., “Nanoscale chemical imaging using tip-enhanced raman spectroscopy: a critical review”, *Angewandte Chemie International Edition* **52**, 5940–5954 (2013).
- [118] M. Zhang, J. Wang, and Q. Tian, “Tip-enhanced raman spectroscopy mapping with strong longitudinal field excitation”, *Optics Communications* **315**, 164–167 (2014).
- [119] M. I. Stockman, “Nanofocusing of optical energy in tapered plasmonic waveguides”, *Physical review letters* **93**, 137404 (2004).
- [120] D. Pile and D. K. Gramotnev, “Adiabatic and nonadiabatic nanofocusing of plasmons by tapered gap plasmon waveguides”, *Applied Physics Letters* **89**, 041111 (2006).
- [121] S. Berweger et al., “Adiabatic tip-plasmon focusing for nano-raman spectroscopy”, *The Journal of Physical Chemistry Letters* **1**, 3427–3432 (2010).
- [122] J. S. Lee et al., “Superfocusing of electric or magnetic fields using conical metal tips: effect of mode symmetry on the plasmon excitation method”, *Optics express* **19**, 12342–12347 (2011).
- [123] R. M. Roth et al., “Resonant-plasmon field enhancement from asymmetrically illuminated conical metallic-probe tips”, *Optics Express* **14**, 2921–2931 (2006).
- [124] A. Goncharenko et al., “Electric field enhancement by a nanometer-scaled conical metal tip in the context of scattering-type near-field optical microscopy”, *Applied physics letters* **88**, 104101 (2006).
- [125] C. Huber et al., “Optical near-field excitation at commercial scanning probe microscopy tips: a theoretical and experimental investigation”, *Physical Chemistry Chemical Physics* **16**, 2289–2296 (2014).

- [126] C. A. Barrios et al., “Highly stable, protected plasmonic nanostructures for tip enhanced raman spectroscopy”, *The Journal of Physical Chemistry C* **113**, 8158–8161 (2009).
- [127] B. Pettinger et al., “Direct monitoring of plasmon resonances in a tip-surface gap of varying width”, *Physical Review B* **76**, 113409 (2007).
- [128] B. Pettinger et al., “Tip-enhanced raman scattering: influence of the tip-surface geometry on optical resonance and enhancement”, *Surface Science* **603**, 1335–1341 (2009).
- [129] E. Bailo and V. Deckert, “Tip-enhanced raman scattering”, *Chemical Society Reviews* **37**, 921–930 (2008).
- [130] N. Hayazawa, T.-a. Yano, and S. Kawata, “Highly reproducible tip-enhanced raman scattering using an oxidized and metallized silicon cantilever tip as a tool for everyone”, *Journal of Raman Spectroscopy* **43**, 1177–1182 (2012).
- [131] L. Meng et al., “Gold-coated afm tips for tip-enhanced raman spectroscopy: theoretical calculation and experimental demonstration”, *Optics Express* **23**, 13804–13813 (2015).
- [132] C. Schäfer et al., “A single particle plasmon resonance study of 3d conical nanoantennas”, *Nanoscale* **5**, 7861–7866 (2013).
- [133] S. Cherukulappurath et al., “Template-stripped asymmetric metallic pyramids for tunable plasmonic nanofocusing”, *Nano letters* **13**, 5635–5641 (2013).
- [134] A. Downes, D. Salter, and A. Elfick, “Finite element simulations of tip-enhanced raman and fluorescence spectroscopy”, *The Journal of Physical Chemistry B* **110**, 6692–6698 (2006).
- [135] B. Ren, G. Picardi, and B. Pettinger, “Preparation of gold tips suitable for tip-enhanced raman spectroscopy and light emission by electrochemical etching”, *Review of Scientific Instruments* **75**, 837–841 (2004).
- [136] C. C. Neacsu et al., “Scanning-probe raman spectroscopy with single-molecule sensitivity”, *Physical Review B* **73**, 193406 (2006).
- [137] T.-a. Yano et al., “Confinement of enhanced field investigated by tip-sample gap regulation in tapping-mode tip-enhanced raman microscopy”, *Applied Physics Letters* **91**, 121101 (2007).
- [138] C. Blum et al., “Tip-enhanced raman spectroscopy—an interlaboratory reproducibility and comparison study”, *Journal of Raman Spectroscopy* **45**, 22–31 (2014).
- [139] M. B. Raschke and C. Lienau, “Apertureless near-field optical microscopy: tip-sample coupling in elastic light scattering”, *Applied Physics Letters* **83**, 5089–5091 (2003).
- [140] G. Picardi et al., “Comparative study of atomic force mode and tunneling mode tip-enhanced raman spectroscopy”, *The European Physical Journal Applied Physics* **40**, 197–201 (2007).
- [141] A. Wiener et al., “Nonlocal effects in the nanofocusing performance of plasmonic tips”, *Nano letters* **12**, 3308–3314 (2012).
- [142] X. Cui et al., “Tuning the resonance frequency of ag-coated dielectric tips”, *Optics express* **15**, 8309–8316 (2007).
- [143] N. Mauser and A. Hartschuh, “Tip-enhanced near-field optical microscopy”, *Chemical Society reviews* **43**, 1248–1262 (2014).

- [144] C. C. Neacsu et al., “Near-field localization in plasmonic superfocusing: a nanoemitter on a tip”, *Nano letters* **10**, 592–596 (2010).
- [145] P. Uebel et al., “A gold-nanotip optical fiber for plasmon-enhanced near-field detection”, *Applied Physics Letters* **103**, 021101 (2013).
- [146] S. Kharintsev et al., “Plasmonic optical antenna design for performing tip-enhanced raman spectroscopy and microscopy”, *Journal of Physics D: Applied Physics* **46**, 145501 (2013).
- [147] A Weber-Bargioni et al., “Functional plasmonic antenna scanning probes fabricated by induced-deposition mask lithography”, *Nanotechnology* **21**, 065306 (2010).
- [148] M. Fleischer et al., “Gold nanocone near-field scanning optical microscopy probes”, *ACS nano* **5**, 2570–2579 (2011).
- [149] I. Maouli et al., “Optical antennas for tunable enhancement in tip-enhanced raman spectroscopy imaging”, *Applied Physics Express* **8**, 032401 (2015).
- [150] Y. Zou et al., “Surface plasmon resonances of optical antenna atomic force microscope tips”, *Applied Physics Letters* **94**, 171107 (2009).
- [151] A. I. Denisyuk et al., “Tunable optical antennas based on metallic nanoshells with nanoknobs”, *Journal of nanoscience and nanotechnology* **12**, 8651–8655 (2012).
- [152] F. Huth et al., “Resonant antenna probes for tip-enhanced infrared near-field microscopy”, *Nano letters* **13**, 1065–1072 (2013).
- [153] T. Umakoshi et al., “Fabrication of near-field plasmonic tip by photoreduction for strong enhancement in tip-enhanced raman spectroscopy”, *Applied Physics Express* **5**, 052001 (2012).
- [154] Y. Gan, “Invited review article: a review of techniques for attaching micro-and nanoparticles to a probe’s tip for surface force and near-field optical measurements”, *Review of scientific instruments* **78**, 081101 (2007).
- [155] T. Kalkbrenner et al., “A single gold particle as a probe for apertureless scanning near-field optical microscopy”, *Journal of Microscopy* **202**, 72–76 (2001).
- [156] I. Barsegova et al., “Controlled fabrication of silver or gold nanoparticle near-field optical atomic force probes: enhancement of second-harmonic generation”, *Applied Physics Letters* **81**, 3461–3463 (2002).
- [157] O Sqalli et al., “Gold elliptical nanoantennas as probes for near field optical microscopy”, *Journal of applied physics* **92**, 1078–1083 (2002).
- [158] Y. Kawata et al., “The use of capillary force for fabricating probe tips for scattering-type near-field scanning optical microscopes”, *Applied physics letters* **82**, 1598–1600 (2003).
- [159] C.-G. Park et al., “Tip-enhanced raman scattering with a nanoparticle-functionalized probe”, *B. Korean Chem. Soc* **33**, 1748–1752 (2012).
- [160] T Okamoto and I Yamaguchi, “Photocatalytic deposition of a gold nanoparticle onto the top of a sin cantilever tip”, *Journal of microscopy* **202**, 100–103 (2001).
- [161] I. U. Vakarelski and K. Higashitani, “Single-nanoparticle-terminated tips for scanning probe microscopy”, *Langmuir* **22**, 2931–2934 (2006).

- [162] H.-W. Cheng et al., “Characterization of single 1.8-nm au nanoparticle attachments on afm tips for single sub-4-nm object pickup”, *Nanoscale research letters* **8**, 1–10 (2013).
- [163] Y. Tian et al., “Shape-controlled electrodeposition of gold nanostructures”, *The Journal of Physical Chemistry B* **110**, 23478–23481 (2006).
- [164] Y.-C. Yang et al., “Electrochemical growth of gold nanostructures for surface-enhanced raman scattering”, *The Journal of Physical Chemistry C* **115**, 1932–1939 (2011).
- [165] M. Paunovic and M. Schlesinger, *Fundamentals of electrochemical deposition*, 2nd ed., Vol. 45 (John Wiley & Sons, 2006).
- [166] “Crc handbook of chemistry and physics”, in, edited by W. M. Haynes (CRC press, 2013).
- [167] Z. Li et al., “Surface properties of platinum thin films as a function of plasma treatment conditions”, *Surface science* **529**, 410–418 (2003).
- [168] P. Fuchs, “Low-pressure plasma cleaning of au and ptir noble metal surfaces”, *Applied Surface Science* **256**, 1382–1390 (2009).
- [169] B. Scharifker and G. Hills, “Theoretical and experimental studies of multiple nucleation”, *Electrochimica Acta* **28**, 879–889 (1983).
- [170] L. Komsijska and G. Staikov, “Electrocrystallization of au nanoparticles on glassy carbon from hclo 4 solution containing [aucl 4]-”, *Electrochimica Acta* **54**, 168–172 (2008).
- [171] M. E. Hyde and R. G. Compton, “A review of the analysis of multiple nucleation with diffusion controlled growth”, *Journal of Electroanalytical Chemistry* **549**, 1–12 (2003).
- [172] P. V. Dudin, P. R. Unwin, and J. V. Macpherson, “Electrochemical nucleation and growth of gold nanoparticles on single-walled carbon nanotubes: new mechanistic insights”, *The Journal of Physical Chemistry C* **114**, 13241–13248 (2010).
- [173] R. H. Webb, “Confocal optical microscopy”, *Reports on Progress in Physics* **59**, 427 (1996).
- [174] D. B. Murphy, *Fundamentals of light microscopy and electronic imaging* (John Wiley & Sons, 2002).
- [175] G. Cox and C. J. Sheppard, “Practical limits of resolution in confocal and non-linear microscopy”, *Microscopy research and technique* **63**, 18–22 (2004).
- [176] O. Hollricher and W. Ibach, “High-resolution optical and confocal microscopy”, in *Confocal raman microscopy* (Springer, 2011), pp. 1–20.
- [177] M. Born and E. Wolf, *Principles of optics: electromagnetic theory of propagation, interference and diffraction of light* (Cambridge university press, 1999).
- [178] T. Wilson and A. Carlini, “Size of the detector in confocal imaging systems”, *Optics letters* **12**, 227–229 (1987).
- [179] J. L. Hutter and J. Bechhoefer, “Calibration of atomic-force microscope tips”, *Review of Scientific Instruments* **64**, 1868–1873 (1993).
- [180] T. Senden and W. Ducker, “Experimental determination of spring constants in atomic force microscopy”, *Langmuir* **10**, 1003–1004 (1994).

- [181] A. Torii et al., “A method for determining the spring constant of cantilevers for atomic force microscopy”, *Measurement Science and Technology* **7**, 179 (1996).
- [182] J. E. Sader, J. W. Chon, and P. Mulvaney, “Calibration of rectangular atomic force microscope cantilevers”, *Review of Scientific Instruments* **70**, 3967–3969 (1999).
- [183] R. Levy and M. Maaloum, “Measuring the spring constant of atomic force microscope cantilevers: thermal fluctuations and other methods”, *Nanotechnology* **13**, 33 (2002).
- [184] P. J. Cumpson, C. A. Clifford, and J. Hedley, “Quantitative analytical atomic force microscopy: a cantilever reference device for easy and accurate afm spring-constant calibration”, *Measurement Science and Technology* **15**, 1337 (2004).
- [185] R. S. Gates and M. G. Reitsma, “Precise atomic force microscope cantilever spring constant calibration using a reference cantilever array”, *Review of Scientific Instruments* **78**, 086101 (2007).
- [186] E. Langlois et al., “Spring constant calibration of atomic force microscopy cantilevers with a piezosensor transfer standard”, *Review of Scientific Instruments* **78**, 093705 (2007).
- [187] B. Ohler, “Cantilever spring constant calibration using laser doppler vibrometry”, *Review of Scientific Instruments* **78**, 063701 (2007).
- [188] K. J. Savage et al., “From microns to kissing contact: dynamic positioning of two nano-systems”, *Applied Physics Letters* **99**, 053110 (2011).
- [189] J. Matey and J. Blanc, “Scanning capacitance microscopy”, *Journal of Applied Physics* **57**, 1437–1444 (1985).
- [190] C. Bugg and P. King, “Scanning capacitance microscopy”, *Journal of Physics E: Scientific Instruments* **21**, 147 (1988).
- [191] Y. Huang, C. Williams, and J. Slinkman, “Quantitative two-dimensional dopant profile measurement and inverse modeling by scanning capacitance microscopy”, *Applied physics letters* **66**, 344–346 (1995).
- [192] J. Kopanski, J. Marchiando, and J. Lowney, “Scanning capacitance microscopy measurements and modeling: progress towards dopant profiling of silicon”, *Journal of Vacuum Science & Technology B* **14**, 242–247 (1996).
- [193] P. Girard, “Electrostatic force microscopy: principles and some applications to semiconductors”, *Nanotechnology* **12**, 485 (2001).
- [194] J. Tamayo and R. Garcia, “Deformation, contact time, and phase contrast in tapping mode scanning force microscopy”, *Langmuir* **12**, 4430–4435 (1996).
- [195] R. Garcia and A. San Paulo, “Attractive and repulsive tip-sample interaction regimes in tapping-mode atomic force microscopy”, *Physical Review B* **60**, 4961 (1999).
- [196] A. San Paulo and R. Garcia, “Unifying theory of tapping-mode atomic-force microscopy”, *Physical Review B* **66**, 041406 (2002).
- [197] S. Lee et al., “Nonlinear dynamics of microcantilevers in tapping mode atomic force microscopy: a comparison between theory and experiment”, *Physical Review B* **66**, 115409 (2002).

- [198] R. A. Schultz et al., “Hyperspectral imaging: a novel approach for microscopic analysis”, *Cytometry* **43**, 239–247 (2001).
- [199] S. J. Leavesley et al., “Hyperspectral imaging microscopy for identification and quantitative analysis of fluorescently-labeled cells in highly autofluorescent tissue”, *Journal of biophotonics* **5**, 67–84 (2012).
- [200] E. K. Hege et al., “Hyperspectral imaging for astronomy and space surveillance”, in *Optical science and technology, spie’s 48th annual meeting (International Society for Optics and Photonics, 2004)*, pp. 380–391.
- [201] J. A. Hackwell et al., “Lwir/mwir imaging hyperspectral sensor for airborne and ground-based remote sensing”, in *Spie’s 1996 international symposium on optical science, engineering, and instrumentation (International Society for Optics and Photonics, 1996)*, pp. 102–107.
- [202] G. A. Shaw and H.-h. K. Burke, “Spectral imaging for remote sensing”, *Lincoln Laboratory Journal* **14**, 3–28 (2003).
- [203] M. Kim, Y. Chen, P. Mehl, et al., “Hyperspectral reflectance and fluorescence imaging system for food quality and safety”, *Transactions-American Society of Agricultural Engineers* **44**, 721–730 (2001).
- [204] A. Gowen et al., “Hyperspectral imaging—an emerging process analytical tool for food quality and safety control”, *Trends in Food Science & Technology* **18**, 590–598 (2007).
- [205] T. Vo-Dinh, “A hyperspectral imaging system for in vivo optical diagnostics”, *Engineering in Medicine and Biology Magazine, IEEE* **23**, 40–49 (2004).
- [206] M. E. Martin et al., “Development of an advanced hyperspectral imaging (hsi) system with applications for cancer detection”, *Annals of biomedical engineering* **34**, 1061–1068 (2006).
- [207] G. Lu and B. Fei, “Medical hyperspectral imaging: a review”, *Journal of biomedical optics* **19**, 010901–010901 (2014).
- [208] M. Bashevov et al., “Hyperspectral imaging of plasmonic nanostructures with nanoscale resolution”, *Optics express* **15**, 11313–11320 (2007).
- [209] M. Iga et al., “Development of thin-film tunable band-pass filters based hyperspectral imaging system applied for both surface enhanced raman scattering and plasmon resonance rayleigh scattering”, *Review of Scientific Instruments* **83**, 103707 (2012).
- [210] R. W. Slawson, Z. Ninkov, and E. P. Horch, “Hyperspectral imaging: wide-area spectrophotometry using a liquid-crystal tunable filter”, *Publications of the Astronomical Society of the Pacific* **111**, 621–626 (1999).
- [211] N. Gat, “Imaging spectroscopy using tunable filters: a review”, in *Aerosense 2000 (International Society for Optics and Photonics, 2000)*, pp. 50–64.
- [212] J. T. Daly et al., “Tunable narrow-band filter for lwir hyperspectral imaging”, in *Symposium on integrated optoelectronics (International Society for Optics and Photonics, 2000)*, pp. 104–115.
- [213] T. Okamoto and I. Yamaguchi, “Simultaneous acquisition of spectral image information”, *Optics letters* **16**, 1277–1279 (1991).

- [214] T. V. Bulygin and G. N. Vishnyakov, “Spectrotomography: a new method of obtaining spectrograms of two-dimensional objects”, in *Analytical methods for optical tomography* (International Society for Optics and Photonics, 1992), pp. 315–322.
- [215] T. Okamoto, A. Takahashi, and I. Yamaguchi, “Simultaneous acquisition of spectral and spatial intensity distribution”, *Applied Spectroscopy* **47**, 1198–1202 (1993).
- [216] M. Descour and E. Dereniak, “Computed-tomography imaging spectrometer: experimental calibration and reconstruction results”, *Applied Optics* **34**, 4817–4826 (1995).
- [217] S. Grusche, “Basic slit spectroscope reveals three-dimensional scenes through diagonal slices of hyperspectral cubes”, *Applied optics* **53**, 4594–4603 (2014).
- [218] A. Sanders et al., “Facile fabrication of spherical nanoparticle-tipped afm probes for plasmonic applications”, *Particle & Particle Systems Characterization* **32**, 182–187 (2015).
- [219] A. Lombardi and L. Weller, “Revealing the near-field plasmonic resonances in single nanostructures using tuneable sers”, in preparation (2015).
- [220] J. T. Hugall and J. J. Baumberg, *Physical Review Letters* (2015).
- [221] M. I. Stockman, “Nanoplasmonics: past, present, and glimpse into future”, *Optics express* **19**, 22029–22106 (2011).
- [222] S. Mahajan et al., “Understanding the surface-enhanced raman spectroscopy “background””, *The Journal of Physical Chemistry C* **114**, 7242–7250 (2009).
- [223] F. G. De Abajo and J. Aizpurua, “Numerical simulation of electron energy loss near inhomogeneous dielectrics”, *Physical Review B* **56**, 15873 (1997).
- [224] F. G. de Abajo and A. Howie, “Retarded field calculation of electron energy loss in inhomogeneous dielectrics”, *Physical Review B* **65**, 115418 (2002).
- [225] J. T. Hugall, J. J. Baumberg, and S. Mahajan, “Disentangling the peak and background signals in surface-enhanced raman scattering”, *The Journal of Physical Chemistry C* **116**, 6184–6190 (2012).
- [226] Y. Gan, “Atomic and subnanometer resolution in ambient conditions by atomic force microscopy”, *Surface Science Reports* **64**, 99–121 (2009).
- [227] M. Holmberg et al., “Nanobubble trouble on gold surfaces”, *Langmuir* **19**, 10510–10513 (2003).
- [228] Y. Song et al., “The origin of the “snap-in” in the force curve between afm probe and the water/gas interface of nanobubbles”, *ChemPhysChem* **15**, 492–499 (2014).
- [229] Q. Zhong et al., “Fractured polymer/silica fiber surface studied by tapping mode atomic force microscopy”, *Surface Science Letters* **290**, L688–L692 (1993).
- [230] P. Hansma et al., “Tapping mode atomic force microscopy in liquids”, *Applied Physics Letters* **64**, 1738–1740 (1994).
- [231] C. A. Putman et al., “Tapping mode atomic force microscopy in liquid”, *Applied physics letters* **64**, 2454–2456 (1994).
- [232] J. Lambe and S. McCarthy, “Light emission from inelastic electron tunneling”, *Physical Review Letters* **37**, 923 (1976).

- [233] R. Berndt, J. K. Gimzewski, and P. Johansson, “Inelastic tunneling excitation of tip-induced plasmon modes on noble-metal surfaces”, *Physical review letters* **67**, 3796 (1991).
- [234] P. Bharadwaj, A. Bouhelier, and L. Novotny, “Electrical excitation of surface plasmons”, *Physical review letters* **106**, 226802 (2011).
- [235] S. Divitt, P. Bharadwaj, and L. Novotny, “The role of gap plasmons in light emission from tunnel junctions”, *Optics express* **21**, 27452–27459 (2013).
- [236] F. Ye et al., “Optical and electrical mappings of surface plasmon cavity modes”, *Nanophotonics* **3**, 33–49 (2014).
- [237] B. Van Wees et al., “Quantized conductance of point contacts in a two-dimensional electron gas”, *Physical Review Letters* **60**, 848 (1988).
- [238] D. Wharam et al., “One-dimensional transport and the quantisation of the ballistic resistance”, *Journal of Physics C: solid state physics* **21**, L209 (1988).
- [239] F. H. Koppens, D. E. Chang, and F. J. Garcia de Abajo, “Graphene plasmonics: a platform for strong light–matter interactions”, *Nano letters* **11**, 3370–3377 (2011).
- [240] J. Christensen et al., “Graphene plasmon waveguiding and hybridization in individual and paired nanoribbons”, *ACS nano* **6**, 431–440 (2011).
- [241] J. Chen et al., “Optical nano-imaging of gate-tunable graphene plasmons”, *Nature* **487**, 77–81 (2012).

List of Symbols

a	radius of a spherical particle [m]
α	polarisability [$\text{C m}^2 \text{ V}^{-1}$]
α_T	coefficient of thermal expansion [K^{-1}]
\mathbf{B}	magnetic field strength/magnetic flux density [T]
β	propagation constant
β	coefficient of damping inclusive of mass [kg s^{-1}]
c	speed of light, $2.99 \times 10^8 \text{ m s}^{-1}$
\mathbf{D}	electric displacement field
D	coefficient of diffusion []
d	dimer gap separation [m]
d_p	confocal pinhole diameter [m]
δ_m	electromagnetic skin depth [m]
E	magnitude of the electric field [V m^{-1}]
\mathbf{E}	electric field [V m^{-1}]
e	fundamental unit of charge, $1.6 \times 10^{-19} \text{ C}$
\mathbf{E}_0	incident electric field [V m^{-1}]
E^o	standard electrochemical potential [V]
E_{ox}^o	standard potential of oxidation [V]
E_{red}^o	standard potential of reduction [V]
ε	complex relative permittivity, $\varepsilon = \varepsilon_1 + i\varepsilon_2$, also known as a dielectric function of a material
ε_0	permittivity of free space, $8.854\,187\,82 \times 10^{-12} \text{ m}^{-3} \text{ kg}^{-1} \text{ s}^4 \text{ A}^2$
$\varepsilon_{z,d}$	complex relative permittivity of a dielectric - assumed constant
$\varepsilon_{z,m}$	complex relative permittivity of a metal (see also $\varepsilon(\omega)$)
$\varepsilon(\omega)$	dielectric function of a metal
\mathbf{F}	force [N]
F	magnitude of force [N]
f	frequency [Hz]
G	conductance [Ω^{-1}]
G_0	quantum of conductance, $7 \times 10^{-5} \Omega^{-1}$
γ	coefficient of damping [s^{-1}]
\mathbf{H}	magnetic field
I	current [A]

J	current density [A m^{-2}]
J_{ext}	external current density [A m^{-2}]
J_{int}	internal current density [A m^{-2}]
J_{tot}	total current density [A m^{-2}]
<i>k</i>	cantilever spring constant [N m^{-1}]
<i>k</i>	magnitude of the wavevector [m^{-1}]
k	wavevector [m^{-1}]
<i>k₀</i>	magnitude of the photonic wavevector, ω/c [m^{-1}]
<i>k₀</i>	initial cantilever spring constant [N m^{-1}]
<i>k_d</i>	magnitude of the wavevector inside a dielectric [m^{-1}]
<i>k_m</i>	magnitude of the wavevector inside a metal [m^{-1}]
<i>l</i>	orbital angular momentum quantum number used to describe the mode of spherical harmonics in the plasmon charge distribution
λ	wavelength [m]
M	magnetisation/magnetic dipole moment per unit volume [m^{-3}]
<i>M</i>	magnification
<i>m</i>	mass [kg]
<i>m_l</i>	projection of the orbital angular momentum quantum number <i>l</i>
μ_i	charge mobility []
μ	relative permeability
μ_0	permeability of free space, $1.256\,637\,06 \times 10^6 \text{ m kg s}^{-2} \text{ A}^{-2}$
<i>n</i>	number density of electrons [m^{-3}]
\tilde{n}	complex refractive index, $\tilde{n} = n + i\kappa$
<i>NA</i>	numerical aperture
ω	angular frequency, $2\pi f$ [rad^{-1}]
ω_l	frequency of the localised surface plasmon mode of angular momentum <i>l</i> [rad]
ω_p	plasma frequency [rad]
ω_{sp}	surface plasmon frequency [rad]
ω_{spp}	surface plasmon polariton frequency [rad]
P	polarisation/electric dipole moment per unit volume [m^{-3}]
ϕ	phase of the wave
ϕ	displacement [m]
φ	electrostatic potential [V]
ψ	wavefunction
<i>Q</i>	quality factor of a resonance
<i>q</i>	electric charge [C]
<i>R</i>	characteristic feature size/radius of nanostructures, normally used in the context of this thesis to refer to the radius of the tip apex [m]
r	spatial vector with components (<i>x, y, z</i>) or (<i>r, θ, φ</i>) depending on coordinate system

r	radial coordinate [m]
r_{axial}	axial optical resolution, i.e. the depth of focus [m]
r_{lateral}	lateral optical resolution, i.e. the minimum resolvable distance between two features [m]
ρ	volume charge density [C m^{-3}]
ρ_{ext}	external volume charge density [C m^{-3}]
ρ_{int}	internal volume charge density [C m^{-3}]
ρ_{tot}	total volume charge density [C m^{-3}]
s	azimuthal angle [$^{\circ}$]
σ	conductivity [S m^{-1}]
σ	surface charge density [C m^{-2}]
σ_{abs}	absorption cross section [m^2]
σ_{ext}	extinction cross section, $\sigma_{\text{abs}} + \sigma_{\text{scat}}$ [m^2]
σ_{scat}	scattering cross section [m^2]
T	temperature [K]
t	time [s]
τ	relaxation time [s]
θ	angle [$^{\circ}$]
u	axial optical coordinate [m]
u	displacement of the free electron gas from equilibrium under an applied field [m]
V	voltage or potential difference [V]
v	lateral optical coordinate [m]
v	velocity [m s^{-1}]
$v_{\text{diffusion}}$	diffusion velocity of electrons [m s^{-1}]
v_{drift}	drift velocity of electrons [m s^{-1}]
\mathbf{x}	spatial vector with components (x, y, z) or (r, θ, ϕ) depending on coordinate system
x	a general spatial coordinate [m]
z	axial spatial coordinate [m]

Acronyms

Notation	Description
2DEG	2D electron gas
a-SNOM	apertureless scanning near-field optical microscopy
AFM	atomic force microscopy
BDP	bonding hybridised dipolar plasmon
BEM	boundary element method
BF	bright-field
BQP	bonding hybridised quadrupolar plasmon
BTh	benzenethiol
CCD	charge-couple device
CTP	charge transfer plasmon
DF	dark-field
DFT	density functional theory
DI	de-ionised
DSO	digital storage oscilloscope
EELS	electron energy loss spectroscopy
EM	electromagnetic
EMI	electromagnetic interference
FDTD	finite-difference time-domain
FIB	focussed ion beam
FWHM	full-width half-maximum
IMI	insulator-metal-insulator
IR	infrared
LSP	localised surface plasmon
LSPP	localised surface plasmon polariton
MIM	metal-insulator-metal
MNP	metallic nanoparticle
NA	numerical aperture
NIR	near-infrared
NP	nanoparticle
NPoM	nanoparticle-on-mirror
ODE	ordinary differential equation
PSD	position sensitive detector

Notation	Description
PSF	point spread function
QCM	quantum corrected model
s-SNOM	scattering scanning near-field optical microscopy
SAM	surface-assembled monolayer
SBDP	screened bonding dipolar plasmon
SCM	scanning capacitance microscopy
SDF	supercontinuum dark-field
SEM	scanning electron microscopy
SERS	surface-enhanced Raman scattering
SHE	standard hydrogen electrode
SMU	source-meter unit
SNOM	scanning near-field optical microscopy
SP	surface plasmon
SPM	scanning probe microscopy
SPP	surface plasmon polariton
SPR	surface plasmon resonance
STM	scanning tunnelling microscopy
TE	transverse electric
TENOM	tip-enhanced near-field optical microscopy
TERS	tip-enhanced Raman scattering
TIR	total internal reflection
TM	transverse magnetic
UV	ultraviolet

Appendix A

Supplementary Theory

A.1 Derivation of the Normal Modes of a Spherical Metallic Nanoparticle

The Laplace equation, describes the behaviour of an electrostatic potential, φ . In a spherically symmetric system the Laplace equation is expanded into, This can be solved by separating the variables such that $\varphi(r, \theta, \phi) = R(r)Y(\theta, \phi)$ giving two separate equations, where λ is an arbitrary constant required for both equations to sum to zero. Functions of the form of $Y(\theta, \phi)$ are considered spherical harmonics describing the angular component of a spherical system. Separating again to $Y(\theta, \phi) = \Theta(\theta)\Phi(\phi)$ leads to another two equations from Eq. ??, where m is another constant. Eq. ?? has a solution $\Phi(\phi) = e^{\pm im\phi}$. Eq. ?? has solutions given by associated Legendre polynomials $\Theta(\theta) = P_l^m(\cos \theta)$ of degree l and order m , restricting $-l \leq m \leq l$. Eq. ?? then has a solution $R = A_l r^l + B_l r^{-(l+1)}$. Combining these into the electrostatic potential leads to a general solution, The spherical harmonics set the charge distributions of the normal modes of oscillation in a MNP.

A.2 Quantum Charge Transport

One of main discussions of this work is the effect of quantum charge transport on plasmon coupling. Both quantum tunnelling and ballistic transport are qualitatively described in the main text for simplicity. The following section shows the relevant mathematical derivations of the conduction properties of metals resulting in the phenomena of quantum tunnelling and ballistic transport.

A.2.1 Quantum Electron Tunnelling

A.2.2 Ballistic Conduction

A 1D constriction between two charge reservoirs of length L and width W can be described as either diffusive if $l, l_\phi \ll L, W$, ballistic if $l, l_\phi \gg L, W$, or quasi-ballistic if inbetween, where l and l_ϕ are the mean free path and phase coherence length, respectively. Conductance in the diffusive regime is as classically expected, $G = W\sigma_{2D}/L$. In the ballistic regime, however, it inherits quantum properties as is thus given by the Landauer formula, where $f(E, E_F)$ is the Fermi-Dirac function and the wavevector of an electron can be related to its energy via $dE = \hbar v dk$. Converting Eq. ?? to an energy basis and adding the rightwards current yields, In the small bias limit¹ the Fermi-Dirac function is expanded as a Taylor series into, Substituting this into Eq. ?? yields the integral, At low temperatures $\delta f / \delta E \rightarrow \delta(E - E_F)$ and the integral evaluates to, from which the conductance $G = I/V$ is derived to be, With the barrier still in place this corresponds to a tunnelling conductance with $T(E_F) < 1$. The point at which the barrier disappears ($E_{\text{barrier}} = E_F$) gives rise to $T(E) = 1$ and opens up a single quantised conductance channel. Adding additional n sub-bands into the constriction continues to increase the conductance by its quantum, $2e^2/h$, and thus the conductance of a 1D *conductive* junction can be expressed as,

¹Large biases are ignored

Appendix B

Supplementary Experimental Details

B.1 Supplementary Optical Details

Features, design justifications and optics theory not essential to the main text are detailed here. The following paragraphs clarify the advantages of the reimaging technique, the limitations in choice of objective lens, beamsplitters and optical bench layout. Lastly, further useful information and optics characterisation, such as the range of laser powers, are presented.

B.1.1 Optical Design

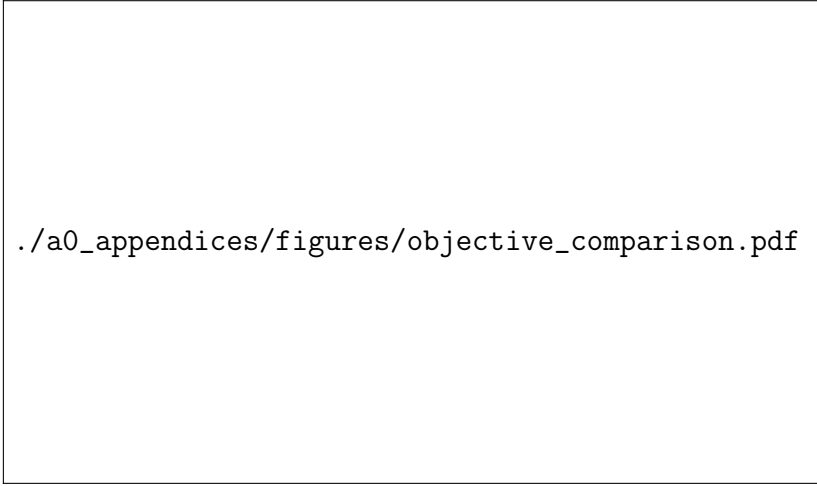
The concept of reimaging, and its effect on beam alignment, is shown in Figure ?? . The ray diagrams show that the beam position in the focus can be adjusted by changing the angle of a mirror placed in the Fourier plane (in the case of the microscope the mirror directly after the DF stop). The shape of the beam, dictated by its angular distribution in Fourier space, is controlled by tilting a mirror in a focal plane (the mirror in the focus of the reimaging arm). The two mirrors provide independent control over the two main beam properties.

The choice of objective was determined by the overall range over which a reference spectrum from a Ag mirror is valid. Two long working distance objectives suitable for single

(a)	angular deviation	(b)	k -space modification	lateral translation

./a0_appendices/./3_test_rig_design/figures/reimaging_concept.pdf

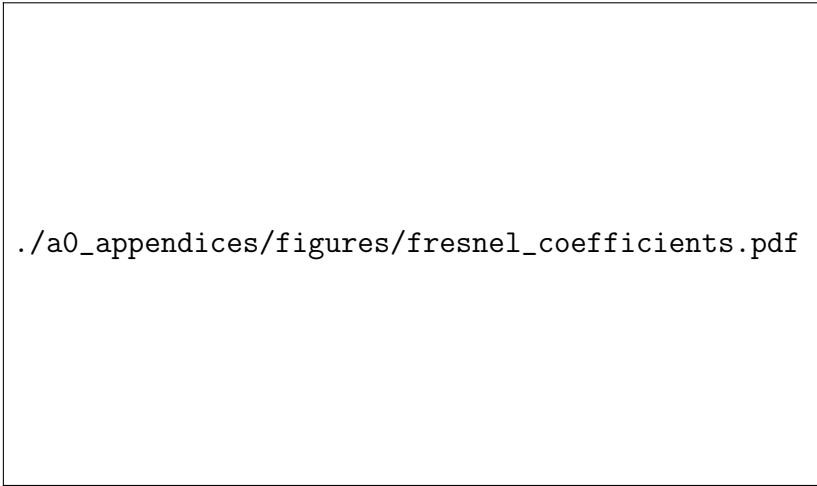
Concept of reimaging for beam alignment. Adjusting the angle of the beam in a focal plane does not change the position of the focus in the image (front focal) plane but changes the position in the Fourier (back focal) plane. Adjusting the angle of the beam in a Fourier plane translates the position of the beam in the image plane without changing its angular components.



./a0_appendices/figures/objective_comparison.pdf

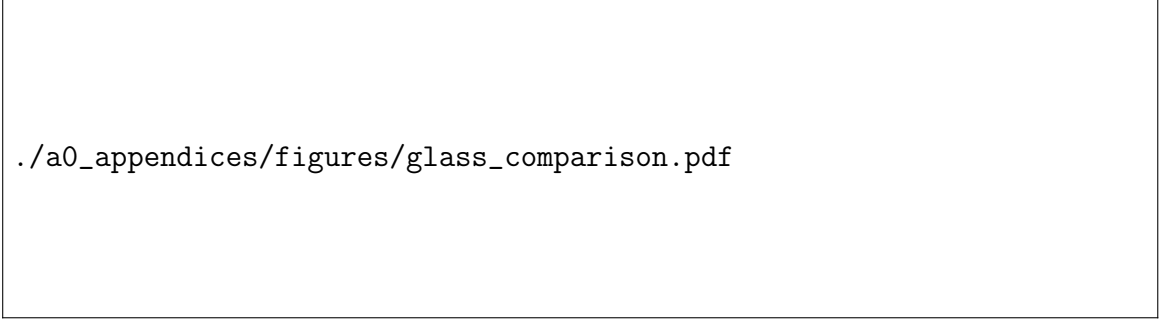
Spectral comparison between VIS and IR objectives. The VIS objective is an Olympus 100× 0.9 NA MPlan BD dark-field objective whereas the IR objective is an Olympus 100× 0.8 NA MPlan bright-field objective.

nanostructure spectroscopy were characterised for use in the microscope: a VIS and a IR objective. The raw spectra measured using each of the objectives is shown in Figure ?? . The sharp cut-on at 480 nm is due to the supercontinuum laser. The VIS objective clearly outperforms the IR objective below 625 nm, though both objective counts are large enough to maintain a good reference signal. Overall, references using the VIS objective only extend marginally more below 500 nm. However, the sharp 700 nm cut-off in the VIS objective means that it is not suitable for spectra in the NIR. The reference signal of the VIS objective is only valid up until 900 nm whereas the IR objective extends to 1100 nm. The gain in spectral range means that the IR objective is chosen despite its lack of dark-field illumination for imaging.



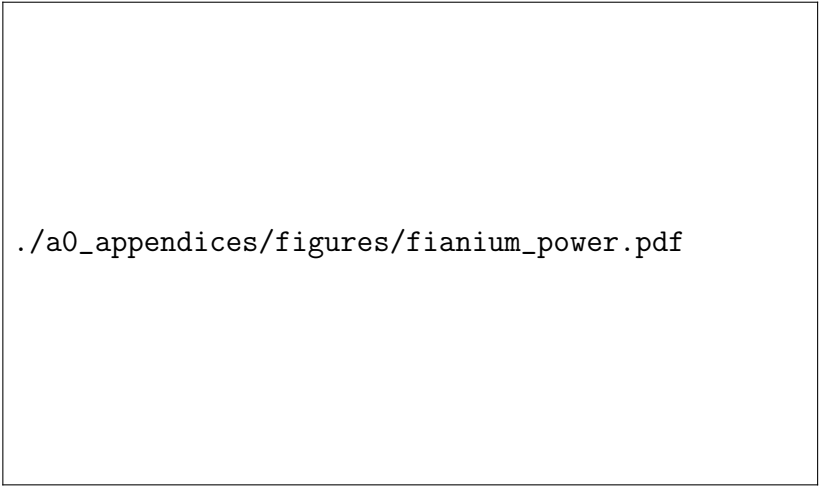
./a0_appendices/figures/fresnel_coefficients.pdf

Reflectance as a function of angle of incidence for glass-air interface. Reflective is calculated from the fresnel coefficients. The refractive index of glass is assumed to be $n = 1.5$. The inset shows a zoomed segment in the low reflectance regime.



`./a0_appendices/figures/glass_comparison.pdf`

Comparison of NBK7 and UVFS glass refractive index and reflectance. Reflectance is calculated at 45° where most beamsplitters operate.



`./a0_appendices/figures/fianium_power.pdf`

Fianium power incident on the back aperture of the objective as a function of driving current. The beam diameter is restricted to the size of the back aperture to accurately measure the power throughput without measuring extra power not transmitted to the sample plane. Error bars represent the precision (standard error) of 1000 repeat measurements at each power, hence they are small, however the large distribution of points shows that the power meter is only accurate to 1 mW.

Consideration was given when designing the optical layout to account for intensity differences in each linear polarisation. Reflection and transmission of an incident EM wave at an interface between two refractive media is characterised by the Fresnel equations, with reflectance given by, where the wave impinges on the interface at an angle θ_i and refracts into a transmitted angle θ_t due to the refractive index change from n_1 to n_2 . The angles are related using $n_2 \sin \theta_t = n_1 \sin \theta_i$. As shown in Figure ??, there is a large difference in reflectance between linear polarisations at higher angles of incidence. The microscope is designed such that the *s*-polarisation corresponds to light polarised along the tip axis, maximising its transmission to the spectrometers.

B.1.2 Optical Characterisation

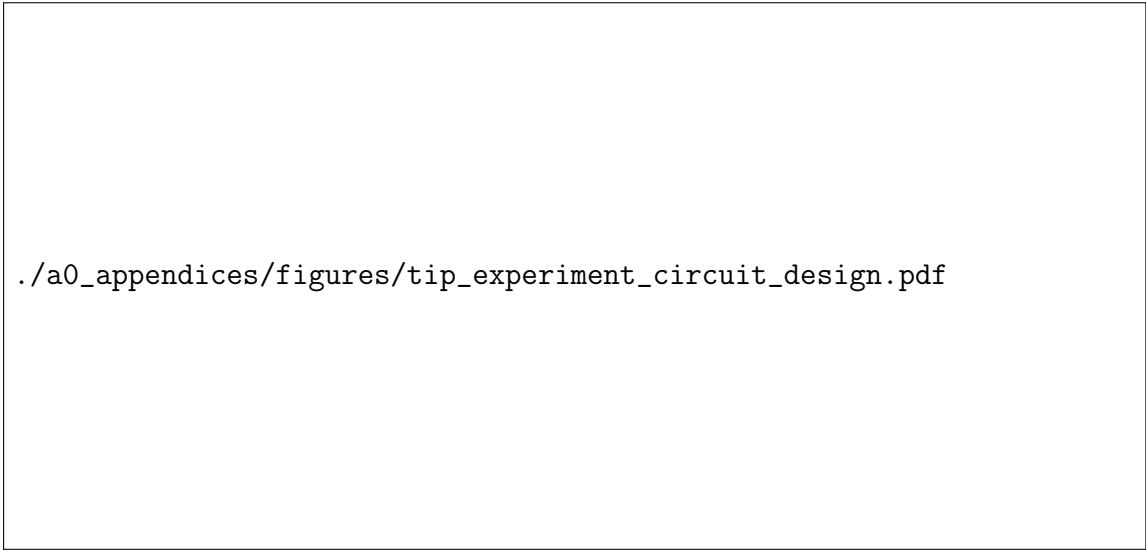
The measured broadband power incident on the back aperture of the objective (removing the contribution from over-filling of the back aperture using an iris) is shown in Figure ???. The power is measured using a thermopile bolometer (Coherent Powermax) with simultaneous measurements of the spectral counts of the *s*-polarised signal component summed between 400–1200 nm. The supercontinuum laser is driven with a d.a.c. of 1100 in most experiments. Under these conditions, less than 1 mW is used to illuminate samples, enough that reflection from a reference substrate just under saturates the spectrometer counts. Assuming a spot size on $\mathcal{O}(1\text{ }\mu\text{m})$ means a focal intensity of 10^8 mW cm^{-2} . Sub-mW powers are sufficient to maintain good signals without risking damage to nanoscale samples.

B.2 Supplementary Electronics

The circuitry of the microscope electronics is shown in Figure B.1.

B.3 Software Lock-In Derivation

To lock into only the signal component at the reference frequency ω_r a reference wave needs to be computed. The first step in the lock-in process is to mathematically construct a single frequency waveform at the correct harmonic using the supplied reference signal. The reference



`./a0_appendices/figures/tip_experiment_circuit_design.pdf`

Figure B.1: Schematic of the electrical measurement circuit. The central routing box allows switching between a.c. and d.c. circuits and low-and high-bandwidth d.c. measurements. The a.c. circuit is used to align two AFM probes together while the d.c. circuit is used to measure spatially dependent signals from the gap between two AFM probes.

signal is typically of the form $A \sin(\omega_{rs}t + \phi_r)$, but the algorithm will also work with any periodic function since it triggers off a rising position edge. When $\sin(\theta) = 0$ and the gradient is positive ($\cos(\theta) = 1$) $\theta = 2n\pi$. Hence the rising edge trigger points t_i occur at, A complex reference wave of the form $e^{ih(\omega_{rs}t + \phi_r)}$, where h is the harmonic of the reference frequency ω_{rs} required to lock into the frequency ω_r , is constructed from the $t_i = mn + c$ fit using, The frequency component of the signal at $\omega_r = h\omega_{rs}$ can be extracted using Fourier analysis, Discretising this not a programmable form results in, where $\text{Re}[Z_s(\omega_r)]$ and $\text{Im}[Z_s(\omega_r)]$ are the x and y of the signal component at ω_r , respectively. Polar coordinates of amplitude and phase are retrieved using the coordinate transforms,

B.4 Capacitive Alignment Model Derivation

Beginning with the general equation of motion for two cantilevers, denoted by $i = (1, 2)$, with initial positions z_{0i} , spring constants k_{0i}^z , masses m_i , damping coefficients β_i^z , and resonant frequencies $\omega_{0i} = \sqrt{k_{0i}/m_i}$, separated by a distance $d(t) = z_1(t) - z_2(t)$ and coupled via the z -components of the of the long range attractive electrostatic driving force F_{EL}^z and short range ($\mathcal{O}(\text{nm})$) Van da Waals and repulsive tip-tip interaction forces F_{TT}^z . The equilibrium separation between tips is denoted by $d_0 = z_{01} - z_{02}$. The equation of motion in the z -axis of the two parallel cantilevers of spring constant $k_i^z = k_{0i}^z + k_{TT}^z$ and damping coefficient $\beta_i^z = \beta_{0i}^z + \beta_{TT}^z$ is given by, where the sign of the force depends on the tip - positive for one tip and negative for the other. Tip-tip interactions can be ignored and $F_{TT}^z = 0$ by assuming alignment takes place at long range and therefore $\beta_{TT}^z = k_{TT}^z = 0$. Further assume that one cantilever remains stationary. The apex separation is then restricted to $d = z_1$ with an equilibrium separation $d_0 = z_{01}$. Under these conditions the motion reduces to that of a single tip, The substitution $z_r = z_1 - z_{01} = d - d_0$ can simplify the equation to using a single relative variable, This equation now describes the whole system rather than each individual tip with the main reference point between tips being the equilibrium separation d_0 .

The remaining force exerted between tips is purely electrostatic and depends on voltage V and capacitance C . In general an electrostatic force acting in one direction can be calculated using, where $\omega_p = 2\omega_s$ is the cantilever pump frequency.

Substituting Eq. ?? into Eq. ?? gives the simplified equation of motion for the dual-tip system, Driving at a pump frequency close to the cantilever resonance ($\omega_p \approx \omega_{01}$) therefore leads to strong resonant oscillations between tips.

Expressing Eq. ?? in terms of z_r and d_0 yields, and enables further simplification via approximation. Assuming that $z_r \ll d_0$ the right hand side of Eq. ?? can be taken to first order using a Taylor series,¹ where, This effective spring constant k_{e1}^z does not cause parametric

¹ $F(z_r) = F(0) + \left. \frac{dF(z_r)}{dz_r} \right|_0 z_r = \left(\frac{-\varepsilon_0 A_{ov} V_0^2}{4} \right) [1 + \cos(\omega_p t)] \left(\frac{1}{d_0^2} - \frac{2z_r}{d_0^3} \right)$

mixing as it oscillates at ω_p and so its effect can be averaged out over time resulting in $\langle k_{e1}^z \rangle = k_{01}^z - \varepsilon_0 A_{ov} V_0^2 / 2d_0^3$. Defining the constant q as, Equation Eq. ?? is of the form of the driven damped Mathieu equation, where

When extending this to determine current flow, the general current through the tip junction is given by, Substituting for $C(t)$ and $V(t)$ and taking the first few terms in the Taylor series results in the first-order current flow, where $C_0 = \varepsilon_0 A^{ov} / d_0$ and z_{off} is an additional offset due to $F_{EL}^z \propto V^2$.